SYNTHESIS, CHARACTERISATION AND MODELLING OF TWO-DIMENSIONAL HEXAGONAL BORON NITRIDE NANOSHEETS FOR GAS SENSING

BY

KEKANA MAGOPA TSHEPHO MCDONALD

A RESEARCH DISSERTATION SUBMITTED FOR THE DEGREE OF MASTER OF SCIENCE IN THE DEPARTMENT OF PHYSICS, SCHOOL OF PHYSICAL AND MINERAL SCIENCES, FACULTY OF SCIENCE AND AGRICULTURE, UNIVERSITY OF LIMPOPO, SOUTH AFRICA.

SUPERVISOR   : PROF TE MOSUANG

CO-SUPERVISORS   : PROF LM SIKHWIVHILU (MINTEK)

                    : DR MA MAHLADISA

2022

Declaration

I declare that "**SYNTHESIS, CHARACTERISATION AND MODELLING OF TWO-DIMENSIONAL HEXAGONAL BORON NITRIDE NANOSHEETS FOR GAS SENSING"** hereby submitted to the University of Limpopo, for the degree of Mater of Science (Physics), is my own work and has not been submitted before for any other degree at any other institution; that all the sources that I have used or quoted have been indicated and acknowledged by means of complete references.

23 May 2022

……………………...   …………………………

Kekana MTM (Mr)   Date

Acknowledgements

I would like to express my sincere gratitude and thank:

❑ My supervisors: Prof T.E Mosuang, Prof L.M Sikhwivhilu and Dr M.A Mahladisa for their exclusive guidance and support in making this study a success.

❑ Colleagues and friend both at the University of Limpopo (UL), Mintek and Counsel for Science and Industrial research (CSIR) for their contributions and sufficient inputs throughout the study.

❑ I also acknowledge UL, Mintek, CSIR and Centre for High Performance Computing (CHPC) for financial support and research facilities.

❑ I am delightful for the constant and continuous support and care from my family and extended families throughout my research journey.

Lastly, I want to thank me for:

❑ Putting all the effort in the fulfilment of my studies.

❑ Keeping continuous consistency perseverance through various tribulations for the duration of this work.

❑ For never gave-upping throughout the toughness and the difficulties of my MSc period.

❑ The enjoyment and the fun I had throughout my studies.

Publications and conference presentations

1. Publication

1. Kekana M.T., Mosuang T.E., Sikhwivhilu L., Mahladisa M.A., Saasa V.S., Mwakikunga B.W. "Synthesis and evaluation of the gas sensing properties of 2D h-BNNSs as a semiconductor-based gas sensor on H_2S and CO gases at various temperatures." The 6th International Conference on Nanotechnology for Instrumentation and Measurement (NanoFim 2021), held at Opole University of Technology Campus in Opole, Poland, 25 - 26 November 2021 (*Published*).

2. Conference presentations

1. Kekana M.T., Mosuang T.E., Sikhwivhilu L., Mahladisa M.A. "Points defects in cubic boron nitride (c-BN)." The 64th annual conference of the South African Institute of Physics (SAIP2019), held at the Protea Hotel, Polokwane, South Africa, 08 – 12 July 2019.

2. Kekana M.T., Mosuang T.E., Sikhwivhilu L., Mahladisa M.A. "Structural stability of the two-dimensional white graphene." 10th Faculty of Science and Agriculture Research Day, held at Protea Hotel, Polokwane, South Africa, 18 - 20 September 2019.

3. Kekana M.T., Mosuang T.E., Sikhwivhilu L., Mahladisa M.A. "Structural stability of the two-dimensional white graphene (Poster)." 13th Centre for High Performance Computing (CHPC) National Conference, held at Beach hood Hotel, Kempton part, Johannesburg, South Africa, 1-5 DECEMBER 2019.

4. Kekana M.T., Mosuang T.E., Sikhwivhilu L., Mahladisa M.A. "Location of boron and nitrogen vacancies in the two-dimensional hexagonal boron nitride." 14th Centre for High Performance Computing (CHPC) National Conference, held virtual, South Africa, 30 November - 2 December 2020.

5. Kekana M.T., Mosuang T.E., Sikhwivhilu L., Mahladisa M.A. "Wet chemical reaction synthesis of two-dimensional hexagonal boron nitride nanosheets (2D h-BNNSs) through chemical vapour deposition (CVD) technique catalyst free approach." 11th Faculty of Science and Agriculture Research Day, held at Bolivia Lodge, Polokwane, South Africa, 06 - 08 October 2021.

6. Kekana M.T., Mosuang T.E., Sikhwivhilu L., Mahladisa M.A., Saasa V.S., Mwakikunga B.W. "Synthesis and evaluation of the gas sensing properties of 2D h-BNNSs as a semiconductor-based gas sensor on H_2S and CO gases at various temperatures." The 6th International Conference on Nanotechnology for Instrumentation and Measurement (NanoFim 2021), held at Opole University of Technology Campus in Opole, Poland, 25 - 26 November 2021.

7. Kekana M.T., Mosuang T.E., Sikhwivhilu L., Mahladisa M.A. "Structural, stability and vacancy properties of both defect free and defected 2D h-BNNSs." The 66th annual conference of the South African Institute of Physics (SAIP2022), held virtual, South Africa, 04 – 08 July 2022.

Dedications

This work is dedicated to:

My Mother

Matlakala Velry Kekana

My Brothers and Sisters

Nkgetheng Collen Kekana

Mokgaetsi Beauty Kekana

Vincent Thapelo Kekana

Promise Koketso Kekana

Grand Brothers and sisters

Lebogang Kekana

Kgaugelo Kekana

Karabo Kekana

Phuthego Kekana

And to me

Magopa Tshepho Mcdonald Kekana

Abstract

The gas sensing performance of two-dimensional (2D) hexagonal boron nitride nanosheets (h-BNNSs) has being studied by means of computational and experimental methods. The structural, stability and vacancies properties of both defect free and defected 2D h-BNNSs were studied using the classical molecular dynamics (MD) approach. The calculations were performed in the NVT Evans and NPT hoover ensembles using the Tersoff potentials with the Verlet leapfrog algorithm to obtain reliable structural properties and energies for defect free, boron (B) and nitrogen (N) vacancies. B and N defect energies were calculated relative to the bulk defect free total energies, and the results suggest that N vacancy is the most stable vacancy as compared to the B vacancy. The radial distribution functions and structure factors were used to predict the most probable structural form. Mean square displacements suggests the mobility of B and N atoms in the system is increasing with an increase in the surface area of the nanosheets. Results obtained are compared with the bulk defect free h-BNNSs. Experimentally, 2D h-BNNSs were synthesised using the wet chemical reaction method through chemical vapour deposition (CVD) catalyst free approach. The X-Ray Diffraction (XRD), Transmission Electron Microscopy (TEM), Fourier Transform Infrared Spectroscopy (FTIR), Raman Spectroscopy (RM), UV-visible Spectroscopy (UV-VIS), dynamic light scattering (DLS), Energy Dispersion Spectroscopy (EDS) and Brunauer-Emmett-Teller (BET) were adopted to attain the structural properties of the nanosheets. Each spectroscopic technique affirmed unique features about the surface morphology of h-BNNSs. The crystallinity of the nanosheets with the stacking of the B and N

honeycomb lattice was validated by the XRD, while the TEM disclosed the specimen orientations and chemical compositions of phases with the number of layers of a planar honeycomb BN sheet, the EDS express the atoms present in the samples and BET validated the surface area of the materials. The FTIR, RM, DLS and the UV-vis expressed the formation of the in-plane, out-of-plane h-BN vibrations and, the nature of the surface with the thickness, particles stability together with the optical properties of the nanosheets. From TEM, FTIR, RS and BET the material fabricated at 800°C showed different morphologies, large number of disordering together with high surface area, which enhances the sensing properties of the nanosheets. However, with an increase in temperature the sensitivity of the nanosheets was found to decrease. Additionally, the UV-vis results, confirmed a lower energy band gap of 4.79, 4.55 and 4.70 eV for materials fabricated at 800, 900 and 1000 °C, that improved the semiconducting properties of the materials, which in return enhanced the sensing properties of the nanosheets. The gas sensing properties of the 2D h-BNNSs were also investigated on hydrogen sulphide (H_2S) and carbon monoxide (CO). The fabricated sensor based on 800 – 900 °C h-BNNSs showed good sensitivity towards ppm of H_2S at 250 °C. The excellent gas sensing properties could be attributed to high surface area, small crystallite size, defect/disordering of h-BNNSs. Overall, the h-BNNSs were found to be more sensitive to H_2S over CO.

Keywords: Molecular Dynamics, Defect free energies, Defects energies, Radial Distribution Functions, Structure Factors, Mean Square Displacement, 2D h-BNNSs, Chemical Vapour Deposition, Nanosheets, Gas Sensing, H_2S, CO and Defects/Dislocations.

Table of Contents

List of figures

List of Tables

Chapter 1

1.1 General Introduction

Swift industrialisation is responsible for the production of environmental pollutant gases, which increase day by day. The transformation of energy systems from fossil fuels to renewable energies, the reduction in primary resource consumption and increased utilisation of secondary resources are therefore central influence to environmental pollutant gases [1]. These results in compromised quality of breathable air as the emissions of various toxic gases continues. The industrialisation processes such as: mines and energy transformation very often release toxic gases that cannot easily be detected by natural human senses such as nose [2].

Carbon monoxide (CO) is one of the major pollutant gases, which results from incomplete oxidation/combustion of fuels [3-5]. Methane (CH_4), nitrogen dioxide (NO_2), carbon dioxide (CO_2) and hydrogen sulphide (H_2S) are other toxic gases, which can be seriously harmful to all living beings [6, 7]. As part of the measures to address this issue, high-performance gas sensors are required to monitor and measure toxic and flammable gas concentration levels in subsurface environment (environments with high pollutants gases) for the safety of all living beings.

To monitor the quality of atmospheric air, research and development towards highly efficient sensors have drastically attracted great interest from the research community in recent years [8-10]. Development of novel materials for sensing applications is currently an area of active research. In further advancing this research to two-dimensional (2D) level, materials such as graphene and

molybdenum disulphide (MoS_2) are physical candidates for gas sensing applications. This is because they ultimately have high surface-to-volume-ratio and wide range tuneable Fermi level [11-18]. Graphene became popular for various technological applications including sensors [19, 20], and its sensing applications was inspired by its perfect flat structure which allows most of its atoms on the surface to be exposed to the environment. It is believed that graphene has the capability of detecting various gas molecules to the atomic scale precision [21, 22]. Nevertheless, its intrinsic semi-metallicity restricts its path towards any practical application due to large leakage current [23, 24].

Analogous to graphene, two-dimensional hexagonal boron nitride nanosheets (2D h-BNNSs), also known as white graphene is another potential flat material gas sensor. 2D h-BNNSs has a wide energy gap of about 5.5 eV [25], which ensures greater acceptable physical applications due to higher thermal and chemical stability [26-29]. The material is derived from boron nitride (BN) which is the lightest chemical compound of group III-V with equal numbers of boron and nitrogen atoms [30-33]. Following the possible isolation of the single sheet of graphite (graphene), and the discovery of its singular properties, research interests has also shifted focus to similar two-dimensional structures.

The single sheet of h-BN is an appealing alternative due to its better chemical and thermal stability than graphene [34, 35], which has been successfully synthesised experimentally [36, 37]. Hexagonal boron nitride (which is also referred to as h-BN), is the most stable and attractive crystalline at room temperature due to its interesting potential applications such as lubricants, protective coatings and deep-ultraviolet light emitter. Moreover, it is applied as a dielectric layer in electronics and acts as a

carrier catalyst [30-33]. Within each layer of h-BN, the charge distribution is biased towards N atom to form a strong ionic and covalent bond, due to the electronegativity difference between B and N atoms, while weak van der Waals interactions exist between adjacent layers [34, 38, 39].

Gas sensors can be grouped based on operational mechanism and material used for fabrication. Operational mechanism and the choice of material is based on the chemical changes being monitored by the sensor, which could be optical absorption, modulation of the field, electrical current, etc. Based on technology the global gas sensor market can be classified as, semiconductor, electrochemical, solid state, photo-sonication detector (PSD), infrared, catalytic and others [40]. However, based on the end-user's perspective the global gas sensor market can be broadly classified as medical, environmental, building attenuation, domestic, automotive, petrochemical, industrial, etc.

For all this, industrial segment account for the largest usage of gas sensors. So one of the major activities in industrial and commercial sectors is the monitoring and control of the surrounding environments. In such a way, the successful implementation of sensors in monitoring and control of the environments frequently leads to innovations in the fields of comfort, security, health, environment, and energy savings. The explicit actual time for monitoring and control is required in enhancing productivity, maintaining health and safety, and limiting environmental pollution. So, the gas sensors have been proven to be the major challenge that inhibits significant advances (because of their life expectancy and the environmental temperature changes) in industrial and environmental monitoring, which is situated at the interface between the system and the environment being monitored [41].

In addition, semiconductor-based devices are ideal for next generation of sensors due to long-term stability, high surface-to-volume-ratio, better gas selectivity, and self-heating capacity. Semiconductor nanomaterials are ideal candidates for fabrication of sensor devices with improved sensitivity, low power consumption and lower limit of detection. Mahammad et $al.$ [42] reported on boron nitride nanosheets (BNNSs) as semiconductor-based gas sensors, synthesised through CO_2-pulse laser deposition (CO_2-PLD) technique, for CH_4 detection. Their work shows that BNNSs based gas sensors can be potentially fast and most importantly, they can operate in harsh environments where properties of other materials fall short [42].

In the current work, the computational and experimental studies of 2D h-BNNSs and their gas sensing performance towards H_2S and CO gases are reported. The computational studies were carried out using classical molecular dynamics (MD) simulations, while the experimental work was done using chemical vapour deposition (CVD) technique at three different synthetic temperatures. The combination of the theoretical and experimental methods, followed in this work, enhanced the understanding and the effects of the synthetic temperatures towards the properties and gas sensing ability of 2D h-BNNSs for H_2S and CO gases detection at various operating temperatures.

1.2 Problem statement

Theoretically, boron nitride nanotubes (BNNTs) have been predicted through density functional theory (DFT) to be able to detect various toxic gases such as CH_4, NO_2, CO_2, CO, H_2, and N_2 [6, 7]. Due to small surface area, BNNTs were found to be less sensitive to various gas molecules as compared to 2D h-BNNSs/white graphene [43]. High performance gas sensors (e.g., white graphene) which could provide

4

stable atomic layer, high electron mobility, better surface area and can function in harsh environments (environments with high temperatures and reactive materials), are required for monitoring of environmental gases. In addition, the chemical alternation of boron (B) and nitrogen (N) atoms within the layers of boron nitride nanosheets (BNNSs) causes the ionic nature of the crystal, which makes the material to be highly sensitive to various gases

1.3 Motivation

The two-dimensional nature of h-BNNSs allows the total exposure of all its atoms to the adsorbing gas molecules, which increases the sensitivity of sensors. h-BNNSs as a semiconductor-based gas sensor, was reported to be potentially faster, and most important, to operate in harsh environments where properties of other materials fall short [42].

Furthermore, the adsorption of gas molecules changes the electronic properties of a gas sensor (white graphene), which is an important requirement for materials to be good sensors. A good and robust sensor-device will be useful to monitor and measure the level of toxic gases in the atmosphere, and therefore improve human health, growth of crops and lowering of the sea water levels in the areas, where sea water levels begin to threaten livelihood [44].

1.4 Aim and objectives

1.4.1 Aim

The aim of the study was to synthesise, model and investigate the properties of 2D h-BNNSs as a semiconductor-based gas sensor for H_2S and CO gases detection.

1.4.2 Objectives

The objectives of the study were to:

    i.   synthesise 2D h-BNNSs.

   ii.   characterise the structural and optical properties of 2D h-BNNSs for different stoichiometric compositions.

  iii.   model the structural properties of the material and investigate the electrical, optical and thermodynamical properties of 2D h-BNNSs.

  iv.   test 2D h-BNNSs for gas sensing.

   v.   compare the computational and experimental results of 2D h-BNNSs.

Chapter 2

Literature review

2.1 Introduction

The development of gas sensors with optimising sensitivity have been gaining prominence interest in nanoscience and materials technology [45]. The use of semiconductor fabrication line is a preferred manufacturing process because of the ability to reduce costs. Originally, the metal oxides semiconducting sensors such as zinc oxide (ZnO), titanium dioxide (TiO_2), zirconium oxide (ZrO), etc. have been widely used for the detection of various gases. This was well before some attention was focused on the nanostructures of the same materials in search for the advanced gas detecting devices [46, 47]. Nanoscience and nanotechnology have lately developed the great ability in fabricating highly sensitive sensors with low costs, portraying large surface-to-volume-ratio. Various factors need to be addressed when fabricating 2D semiconductor gas sensors. Notably, characteristics that should be portrayed by a good sensor are particularly gas selectivity, sensitivity, accuracy, repeatability and reproducibility stability in different environments. A short response and recovery time with low operating temperatures complements a successful design [47-57]. 2D materials such as graphene and $MoSO_4$ have been fabricated and tested, and their successful implementation have brought much interest to 2D h-

BNNSs for better gas detection [58]. In this chapter, the distinct structural information of BN, more emphasis on nanosheets form, different synthetic methodologies, the importance of various gas detection and their impact to the environments and all livelihoods are being communicated.

2.2 Structural information on boron nitride

Boron nitride (BN) atomic orbitals are either sp^2 or sp^3 hybridised under normal conditions. This produces several crystalline forms [59], which are isostructural to carbon and generally exists within the following crystalline forms; graphite-like hexagonal boron nitride (h-BN), diamond-like cubic boron nitride (c-BN), rhombohedral boron nitride (r-BN), and wurtzite boron nitride (w-BN). It forms hexagonal (h) and rhombohedral (r) lattices via sp^2 hybridised bonding and forms cubic (c) or wurtzite (w) lattices via the sp^3 hybridised bonding configuration. Among all of these, h-BN and c-BN are the most stable and widely available. Apart from sp^2 hybridised crystalline h-BN and r-BN, two others less ordered sp^2 configured allotropes, amorphous (a)-BN, turbostratic (t)-BN, can form during the synthesis of h-BN, and r-BN. a-BN appears due to structural disorder introduced at the atomic level. Therefore, a-BN is a completely disordered h-BN and is very unstable in air, reacting with water (moisture) in the environment to form boric acid, boric oxides, and hydroxides [60]. t-BN on the other hand, forms due to a fault in the c-axis orientation of the h-BN layers (less or no ordering between the basal planes in subsequent layers) [61]. Most of the time, the interlayer spacing in t-BN is larger than those of h-BN and r-BN, and thus only in plane ordering of atoms is possible in t-BN. This type

of BN has also been reported to be unstable after long storage in air, forming ammonium borate compounds ($NH_4B_5O_8 \bullet 4H_2O$) [62].

2.3 Structure of hexagonal boron nitride nanosheets

Two-dimensional (2D) hexagonal boron nitride nanosheets (h-BNNSs) are layered materials composed of boron (B) and nitrogen (N) atoms. The configuration is analogous to that of graphene and graphite carbon nitride. Due to the remarkable structural similarity with graphene (bond length and interlayer distance); single layer hexagonal boron nitride is also called 'white graphene' [63]. In Physics terms, is just cutting one layer sheet from the known hexagonal boron nitride to obtain white graphene. White graphene is a sp^2-hybridised 2D semiconductor, which is isostructural to graphene with sub-lattices being occupied by equal numbers of boron and nitrogen atoms alternatingly arranged in a honeycomb configuration. The areal crystal structure of h-BNNSs has crystallographic parameters of $a = b = 0.250$ nm, $c = 0.666$ nm, in plane B-N bond length of 0.144 nm and bond angles of $\alpha = \beta = 90°, \gamma = 120°$ and lastly the interlayer spacing of 0.333 nm enable excellent comparison with graphene. There is a significant difference in the electronegativity between the B (2.04) and N (3.04) atoms [63].

Therefore, the B-N bond is covalent and slightly ionic in nature, which is highly polarised because of the high asymmetry of the sub-lattices, resulting in a large band gap of ~5 – 6 eV [64]. Consequently, there is a layer-by-layer interaction between the neighbouring layers of B and N atoms in addition to the van der Waals forces. Like

the carbon allotropes of graphene, carbon nanotube, and fullerene, h-BN can form BNNSs [9], BNNTs [65], and octahedral BN fullerenes [66]. In addition, various h-BN nanoscale morphologies, such as nanoribbons [67, 68], nanoplates [69, 70], nanowires [71], nanofibers [72], nanoropes [73], nanocups [74], nanofunnels [75], nanomikes [75], microbelts [43], and BN foams [76], have also been reported.

The 2D h-BN can be either zigzag or armchair edge terminated (Figure 2.1). From first principles and density functional theory (DFT) calculations, the armchair edge termination for h-BN nanoribbon has been found to be more energetically favourable than the zigzag edge termination [77, 78]. On the other hand, the nitrogen terminated zigzag edge is more favourable than the boron terminated one grown on Cu substrate, thus producing equilateral triangles during the growth [77, 78].

Moreover, on h-BN and isostructural graphite there is a stacking order difference as presented in Figure 2.1. The optimal AA stacking mode of h-BN has a partially positively charged boron atom residing on top of a partially positively charged boron atom, and partially negatively charged nitrogen atom residing on top of a partially negatively charged nitrogen atom in the adjacent layers. The optimal AA′ stacking mode of h-BN has a partially negatively charged nitrogen atom in one-layer residing on top of a partially positively charged boron atom in the adjacent layers. Hence, this configuration minimises the electrostatic energy of the material.

The optimal AB stacking of h-BN has a boron atom in a given layer residing atop the centre of a hexagon of the adjacent layer, and the metastable AB′ stacking mode of h-BN has eclipsed boron atom positions, whereas the nitrogen atoms appear on top of hexagon centres of adjacent layers. The optimal AC stacking of h-BN has a nitrogen atom in a given layer residing atop the centre of a hexagon of the adjacent layers, and the unstable AC′ stacking mode of h-BN has eclipsed nitrogen atom

positions whereas the boron atoms appear on top of hexagon centres of adjacent layers.
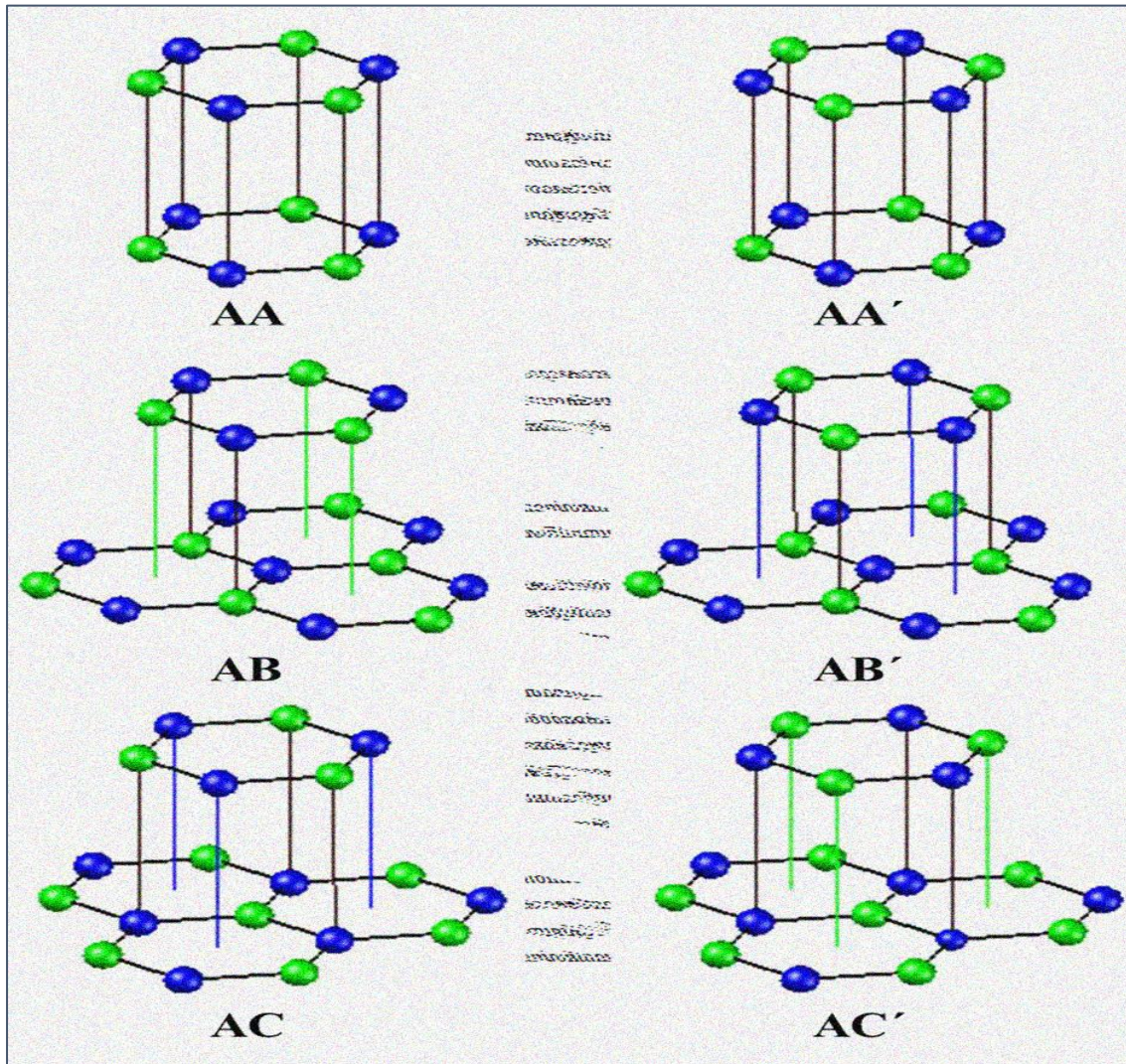
Figure 2. 1: The visualisation of the six possible types of bi-layer h-BN stacking modes [79]. *Khan et al.* [79] are acknowledged for these visualisations.

Lower (upper) layer hexagons are indicated by larger (smaller) circles representing the atoms and dashed (full) lines representing sp^2 covalent bonds. Blue (green) circles represent nitrogen (boron) atoms. From a naive electrostatic point of view, the AB, AB′ and AC, AC′ stacking modes of h-BN should be energetically equivalent.

However, due to the vanishing electrostatic interactions between partially charged atomic centres on adjacent layers and enhanced by Pauli repulsions between eclipsed nitrogen centres, among these various orientations of h-BN, Bernal stacked AB/AC, similar to graphite, have been reported to be energetically favourable structures, in addition to the AA' stacking for h-BN [80, 81].

Structurally, a single layer of h-BN is very similar to a graphene sheet having a hexagonal backbone where a boron–nitride pair replaces each couple of bonded carbon atoms, making the two materials isoelectronic. Nevertheless, due to the electronegativity differences between the boron and the nitrogen atoms, the π electrons tend to localise around the nitrogen atomic centres [82-85], thus forming an insulating material. Furthermore, the polarity of the B-N bond results in the build-up of effective charges on the atomic centres, thus allowing for interlayer electrostatic interactions between partially charged atoms to join higher order electrostatic multipole interactions, dispersion interactions, and Pauli repulsion in dictating the nature of the interlayer binding.

This, in turn, stabilises the AA' stacking mode (see Figure 2.1) where a boron atom bearing a partial positive charge in one layer resides between the oppositely charged nitrogen atoms on the adjacent layers. Based on the above considerations, one may generally deduce that electrostatic interactions between partially charged atomic centres may play a crucial role in the interlayer binding of polar-layered materials [82]. Specifically, the electrostatic attractions between the oppositely charged atomic centres in adjacent h-BN layers are expected to result in a considerably shorter interlayer distance than that measured for graphite. Nevertheless, the interlayer distances in graphite (0.333–0.335 nm) [86-88] and h-BN (0.330–0.333 nm) [88-92]

12

are essentially the same, suggesting that electrostatic interactions between partially charged atomic centres, which exist in h-BN and are absent in graphite, or have little effect on the interlayer binding. A recent study shows that van der Waals forces, rather than electrostatic interactions, are responsible for anchoring the h-BN layers at the appropriate interlayer distance [93].

Further support for this argument is found when comparing the optimal AA′ stacking mode with the AB′ stacking mode where the partially positively charged boron sites are eclipsed and the nitrogen atoms reside atop hexagon centres in adjacent layers (see Figure 2.1). From a naive electrostatic point of view, one would expect the AA′ mode; where opposite charges reside atop each other, to be considerably lower in energy than the AB′ mode. However, according to advanced ab initio calculations, the latter (AB) is found to be only 0.875 – 2.0 meV/atom higher in energy [93, 94].

Furthermore, when considering the AC′ stacking mode (see Figure 2.1), which in terms of electrostatic interactions between partially charged atomic centres is equivalent to the AB′ mode, its total energy is higher by as much as 6.5 – 12.0 meV/atom than both the AA′ and the AB′ modes [93, 95]. This may be related to enhanced Pauli repulsions between the more delocalised overlapping electron clouds of the nitrogen atoms [95, 96]. The partially ionic structure of BN in h-BN reduces covalence and electrical conductivity and unlike graphite, favours the AA′ stacking. Typically, this is the most energetically favourable stacking observed in h-BN, where the electron-deficient B atoms are directly above or below the electron-rich N atoms in the adjacent layer.

2.4 Defects in BNNS

Consistent with defects solid state theory, various defects such as vacancies, edges, grain boundaries, interstitial and substitutional atoms can exist in the 2D h-BN. Such can be introduced during the synthesis processes or because of subsequent environmental effects, can exist in the 2D h-BN, and may have investable impact on the materials behaviour and performance. This is possible because the majority of atoms are in the surface in 2D materials, and perturbation of the surface atomic arrangements due to defects can change the overall properties of the 2D crystal [79]. For example, the presence of Stone-Wales (pentagon-heptagon pairs, 5/7) type line defects in BNNSs can significantly lower the band gap [97].

In 2D materials where mono- to few-layer cases are mostly considered, the term 'grain boundary', which is a three-dimensional entity, is often replaced with 'domain boundary'. The line defects in a bulk crystal thus correspond to the domain boundary in 2D materials. A polycrystalline 2D material is thus made up of various domains connected along the domain boundaries. The main topological defects in the 2D material can be divided into three types: disclination, dislocation, and domain boundary. In sp^2 hybridised hexagonal systems, simple types of defects are SW defects [98, 99], generated by reconstruction of materials lattice (switching between pentagons, hexagons, and heptagons) with rotations of bonds by 90° [100].

The SW defects can be formed by rapidly cooling from high temperature or under electron beam irradiation [101, 102]. The Stone-Wales type defects, which are very common for graphene, were predicted to be energetically less favourable than the

square-octagonal pair (4/8) line defects, due to the unfavourable homo-elemental bonding formations (B-B or N-N bonds) in the former case [103, 104]. In a recent study by *Liu et al.* [10], however, through the density functional theory (DFT) calculations, both the 4/8 and 5/7 defects were predicted to be possible, depending on the tilt angles of the domain boundaries [105].

The polar domain boundaries, involving the 4/8 and 5/7 type defects, neutralise the net charge, being positive at B-rich edges and negative at the N-rich edges [105]. The predicted 4/8 or 5/7 type defects have been experimentally confirmed by scanning tunnelling microscopy (STM) [97] and high-resolution transmission electron microscopy (HR-TEM) analysis [106]. The exact natures of the bonding elements in the domain boundaries were unresolved. Nevertheless, the possible atomic configurations in the 4/8 and 5/7 type domain boundaries have been theoretically predicted for future experimental reference [97].

Among these various configurations, 4/8 type polar domain boundaries, including the less favourable B-B or N-N bonds, have been reported experimentally [107], while the other configurations are yet to be confirmed. Another kind of defects known to occur in 2D h-BN is the vacancy defect/ point defects, which is caused by the removal of B or N atoms from the nanosheets or the migration of the atoms, from the nanosheets to the interstitial site of the material. High temperature annealing and electron beam irradiation are common processes in device fabrication and characterisation, which are prone to induce points defects, types of which are B or N vacancies.

The early theoretical studies on vacancies in h-BN conducted in 2007, where the break-up of B-N bonding was reported, formation of the homo-nuclear bond of N atoms, and reconstruction of the N-N bond were predicted [108]. Migration of B

vacancy was shown to occur in the temperature ranging from 840 to 1400 K, while the migration of N vacancy was energetically unfavourable until the melting point of h-BN was reached [109]. Predominantly, boron mono-vacancy defect formation has been observed in high-resolution electron microscopy (HR-TEM) imaging of BNNS [110]. Syntheses induced atomic vacancy formation in the nanosheets has not been reported.

2.5 Hexagonal boron nitride nanosheets (h-BNNSs)

2.5.1 Mechanical properties

There have been a few measurements on few-layer BN produced by chemical vapour deposition (CVD). *Song et al.* [37] was the first to report that the elastic modulus of CVD grown bilayer BN nanosheets as 0.334 ± 0.024 TPa (that is, E^{2D}=112 ± 8 Nm^{-1}), and their fracture strength as 26.3 GPa (that is, 8.8 Nm^{-1}) [37]. These values are much smaller than those predicted by theoretical calculations. From the aspect of theoretical calculations, although the mechanical properties of few-layer BN have never been theoretically investigated, the Young's modulus of 1 layer BN was predicted to be 0.716 – 0.977 TPa (that is, E^{2D}= 239 – 326 Nm^{-1} with an effective thickness of 0.334 nm), while its breaking strength fell in the wide range of 68 – 215 GPa (that is, 23 – 72 Nm^{-1}) [37, 111-119].

The lowered mechanical properties of the 2 layered CVD BN reported by *Ding et al.* [120, 121] were attributed to the presence of defects and grain boundaries. *Kim et al.* [122] measured the Young's modulus of ~15 nm thick (that is, ~45L) BN nanosheets produced by CVD to be 1.16 ± 0.1 TPa [101]. *Li et al.* [123] investigated the bending modulus of BNNSs which was disclosed to be ~50 nm-thick (that is, ~150L) [123]. The scarcity of regular study of the intrinsic mechanical properties of atomically thin BN of different thicknesses greatly delays the study and use of these nanomaterials.

On the other hand, the different interlayer interactions in few-layer BN and graphene [124-126] could play important roles in their mechanical properties. *Aleksey Falin et al.* [127] reported the mechanical properties of high-quality 1 – 9L BN nanosheets experimentally using AFM. Mono-layer BN had a Young's modulus of 0.865 ± 0.073 TPa, and a fracture strength of 70.5 ± 5.5 GPa. Few-layer BN is suggested to be as strong as 1L BN. This is different in the case of graphene whose modulus and strength is known to decrease dramatically with increasing thickness.

Theoretical and experimental investigations indicated that the difference in mechanical properties of BN and graphene is caused by the distinct interlayer interactions in these two nanomaterials under large in-plane strain and out-of-plane compression. The DFT calculations where van der Waals interactions are included revealed that 2L graphene had energetically favoured sliding under an in-plane strain and large compression close to the indentation centre, while 2L BN could have large positive sliding energies under the same conditions to prevent it from sliding [127]. According to the simplified models using the sandwich beam structures, graphene layers tended to slide during indentation, but BN layers were mostly glued, especially the area under the tip. Thus, the studies suggested that BN nanosheets are one of the strongest insulating materials, and most importantly, the strong interlayer interaction in BN nanosheets, along with their thermal stability, make them ideal for mechanical reinforcement applications [127].

2.5.2 Thermal conductivity

The thermal conductivity of h-BN is up to 400 W (m^{-1} K^{-1}) at room temperature, which is higher than many of the metals and ceramic type materials. h-BN has a typical anisotropy: having a high thermal conductivity in the direction perpendicular to the c-axis of 300 W (m^{-1} K^{-1}), low thermal expansion coefficient of $0 – 2.6 \times 10^{-1}$ K^{-1}, and a

relatively high tensile strength of 41 MPa. When parallel to the c-axis direction, h-BN has a lower thermal conductivity of 20 – 30 W (m^{-1} K^{-1}) and high compressive strength [128-132]. Thermal conductivity experimental value for 11 layers (11L) h-BN was reported to be 360 W (m^{-1} K^{-1}) (390 W (m^{-1} K^{-1}) for bulk h-BN) and 250 W (m^{-1} K^{-1}) in 5 layers h-BN due to the higher polymeric residue contamination [133]. The high in-plane thermal conductivity and insulating nature of BNNS have been used to prepare thermally conductive nano-oils containing BNNS nano-fillers [134, 135].

2.5.3 Optical Properties

The optical properties of BNNSs were reported through UV-vis spectroscopy [136]. A 2D h-BN is known to have no absorption in the visible range in both the experimental and theoretical calculations. However, it absorbs in the ultraviolet region and has a good photoluminescence property [136]. It is theoretically known that the electronic state of 2D semiconducting materials can be reflected to their optical properties, which are widely used to calculate the band gap energies of semiconductors.

The band gap energy of h-BN is known to be in the range of 3.6 – 7.1 eV from the experiments of h-BN with different structures reported in the available literature data [137]. *Gao et al.* [138] reported the measurements of UV-vis optical absorption spectrum of h-BN by investigating as-prepared h-BN nanosheets, where the absorption peaks were found to be at 251, 307 and 365 nm, which corresponds to band gap energies of 4.94, 4.04, and 3.40 eV. As a wide band gap material [139, 140], h-BN is transparent in infrared and visible light, while in ultraviolet light it has a strong optical absorption at 251 nm with a strong excitation absorption shoulder [138].

2.5.4 Stability in air

Few-layered h-BN have been found to be thermally stable in air up to 1500 °C and chemically inert [141, 327]. BNNSs of about 5 nm thick were reported to resist oxidation up to 1100 °C on Ni substrate and up to 500 °C on a Cu substrate in 300-mTorr oxygen atmosphere for 30 minutes [142]. Considering its honeycomb structure that is impermeable to small molecules, chemical inertness, high-temperature stability in air, and insulating nature, BNNSs were found to be very stable at room temperature in air. However, oxygen reduction reaction at room temperature on top of nitrogen rich defects of the mono-layer h-BN have been theoretically predicted [143]. The large number of defects formed during the growth process thus makes it worthwhile to study the long-term stability of BNNSs in a room temperature air environment.

2.5.5 Chemical properties

A 2D h-BN possesses the inert chemical properties to both strong acidic and basic solutions [144]. The chemical inertness of h-BN material, allows it to commonly be used as a coating material for transition metal surface to protect them against corrosion [145, 146], where the thickness, aesthetics, and stability of the underlying substrate are important in harsh environment. Now, a question naturally arises, what happens if the thickness of this coating material (h-BN) is reduced to a single atomic layer? Will its chemical inertness be retained on the transition metal surface? The issue has already been addressed in the context of Ni (111) support on h-BN nanosheet [147]. Effect of transition metal on the properties of h-BN sheet is now well documented in the literature [147, 148].

In fact, hexagonal BN has successfully been synthesised on several FCC transition metal substrates such as Ni (111), Pd (111), Pt (111) [149–152], Ru (001), Rh (111)

[153] via epitaxial route. Among them, the combination of h-BN/Ni (111) is a special one because of their desirable crystalline compatibility, which is an essential prerequisite in forming a defect free and atomically sharp epitaxial interface. Being a magnetic material, the Ni-substrate introduces spin polarisation as well as gap states in the wide gap of h-BN electronic structure. These states are primarily responsible for the functionalisation of inert h-BN nanostructures [147].

2.5.6 Sliding characteristics

The 2L layered BN sliding tendencies discussed here are based on the sandwich beam geometries estimations [127]. The estimations did not consider the nonlinear deformation in the structures under indentation [127]. The two surface layers of the 2L BN can be defined as faces, and the interlayer interactions including van der Waals interactions can be viewed as a core. Such designation meets the basic requirement for a sandwich structure where the faces are much stiffer than the core [127]. In addition, the core in BN nanosheets satisfies the concept of an 'antiplane' core, which has no contribution to the bending stiffness of the structure but can sustain a finite shear stress. The beams with a length of 1,300 nm and width of the unit cell of h-BN have both ends clamped and are under central loads. The shear stiffness of BN was linearly approximated based on the vdW-DFT-deduced sliding energy from the AA to AA$^{\prime}$ stacking in BN [130]. The shear stiffness values of BN, when no strain or compression applied, was found to be 6.61 GPa [154], where the shear stiffness of h-BN values is known to range between 2.5 – 9.0 GPa [154-157]. However, under a large strain and compression close to the indentation centre, the shear stiffness value of BN increased enormously to 534 GPa [127].

2.5.7 Other properties

Projecting BNNSs in such a way that the layered surface area morphologies is vertically aligned and the core appear on the horizontal, the material demonstrate super-hydrophobia. *Weitz et al.* [158] argued this property using droplets hitting the vertical surface perpendicular until a contact angle of 150°. The ultrahigh surface area and aspect ratio of porous h-BN nano-belts have been utilised in hydrogen storage application [43]. Furthermore, BNNS has been reported as an effective water cleaning agent (taking advantage of its large surface area) to adsorb oil from an oil water solvent mixture [159].

In summary BNNS portrays the following properties: low density, high strength, large band gap energy, low dielectric constant, high thermal conductivity, resistance to high temperature oxidation, capability to behave as a high ultraviolet emitter, and high resistance to wet chemical attacks in both acidic and basic environments, more utilisation of this material is expected in the near future, and it might be the next generation material for electronic device fabrication and applications in harsh environments [79].

2.6 Synthesis of BNNS

In 1842, the synthesis of BNNS was first initiated with the reaction between boric oxide and potassium cyanide [160]. The most popular commercial methods to synthesise h-BN powders, is by heating boric acid/boric oxide and ammonium/melamine/urea mixture at 900 °C, followed by annealing at 1500 °C in N_2 atmosphere to increase the crystallinity of the powders [160, 161]. Immediately after the discovery of graphite in 2004, then the synthesis of 2D h-BN was brought into the centre of research interest [162]. Globally speaking, there are two methods used to fabricate BNNS, which is top-down, where bulk h-BN is exfoliated and/or thinned,

and bottom-up, where B and N atoms form few-layered h-BN. The suitable synthesis methods should be selected according to the preferred application. Following is the summary of the BNNS synthesis routes that have been generally adopted (Figure 2.2)
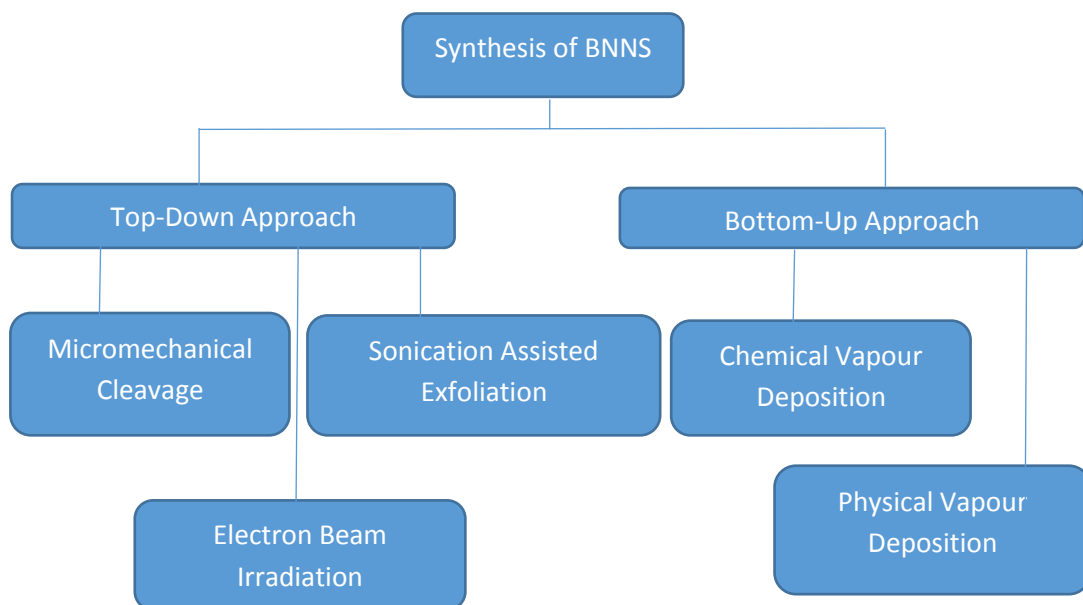
Figure 2. 2: Commonly used methods for the synthesis of BNNS.

2.6.1 Top-Down Approach

This method is to exert certain forces (shearing force for example) to overcome the van der Waals forces that hold BN layers together. This method is useful for large-scale production of BNNSs, but it generally produces BNNSs with a large distribution of layer numbers, various lateral sizes, and contamination.

2.6.1.1 Micromechanical Cleavage

Scotch tape has been used to peel off layered materials (graphite, BN, MoS_2, $NbSe_2$, and $Bi_2Sr_2CaCu_2O_x$) down to mono- and few-layers [163]. The effective procedure to extracts the 2D crystallites was implemented, where a fresh surface of a layered crystal was rubbed against another surface, which left variety of flakes attached to it (the rubbing process is similar to drawing by a chalk on a chalkboard). This technique can lead to BNNS with large lateral size and relatively free of contamination (aside from the tape adhesive which can be removed by a thermal anneal). BNNS obtained in this way can be easily stacked on top of another 2D material.

For example, flexible field effect transistors (FETs) prepared by stacking exfoliated BNNS and graphene, have shown exceptional room temperature carrier mobility [164, 165, 166] and flexibility [166]. Instead of the direct peeling applied in the scotch-tape method, shearing forces were employed in the ball milling process to exfoliate BNNS from bulk h-BN powders [167, 168]. Direct contact of the h-BN powders with the grinding balls can be avoided by carrying out the process in a solvent medium, which improves the efficiency of the process and the quality of the nanosheets [169]. Ball milling without using a solvent generates a large numbers of defects and impurities in the nanosheets [170-172].

2.6.1.2 Sonication-Assisted Exfoliation

Sonication in common organic solvents was reported to effectively overcome the van der Waals forces between the layers in highly oriented layered materials. An extensive study of sonication-assisted exfoliation was conducted by the *Coleman et al.* [173] where they exfoliated h-BN, MoS_2, WS_2, $MoSe_2$, $MoTe_2$, $TaSe_2$, $NbSe_2$,

NiTe$_2$, and Bi$_2$Te$_3$ in a wide range of solvents, and the best 20 solvents for h-BN, MoS$_2$, and WS$_2$ exfoliation were identified [173].

The amount of nanosheet exfoliation and retention in the solvents was found to be dependent on the solvents' surface tension value, and better exfoliation was seen for 40 mJ/m^2. Several reports were published afterward on exfoliating BNNS by intercalating ions and compounds inside the layers [174-177]. Molten hydroxides of NaOH and KOH were used to exfoliate h-BN powders down to mono- and few-layers of BNNS by reaction, curling, cutting, and peeling mechanisms [178].

Interestingly, even water was found to be suitable for obtaining mono- and few-layer BNNS by sonication-assisted hydrolysis of boron nitride bulk powders [179]. Besides conventional solvents, BNNS were exfoliated in 1, 2 dichloroethane solution of poly (m-phenyl-enevinylene)-co-(2, 5-dictoxy-p-phenylenevinylene) [180] (1.2 mg polymer in 10 ml solution) by ultra-sonication. Although BNNSs are very inert towards acid and basic attacks, functionalisation of the BNNSs has been attempted to fully utilise its properties in polymer composites. *Liu et al.* [181] used block copolymers [(P(S-b-MMA)), where PS is polystyrene, PMMA is methylmethacrylate and b represents the double block polymer], to interact with the exfoliated BNNS [181]. The different solubility of polystyrene and PMMA in the block copolymer broadened the dispersion range of the nanosheets even where the Hansen solubility parameters were mismatched. For example, BNNSs can be dispersed in acetone and toluene using the block copolymers, although acetone and toluene are considered unsuitable for BNNSs dispersion. In another work, BNNS were ball milled at high energy to incorporate mechanical defects. These defects were utilised to effectively exfoliate and functionalise the nanosheets by gold nanoparticles [182]. Amine functionalised

exfoliated stable BNNS dispersion in organic solvents and water was achieved using octadecylamine (ODA) for the functionalised molecules [183].

Functionalisation is achieved due to the strong Lewis acid-base interaction between electron deficient boron and electron rich amine molecules. In a recent work by *Sainsbury et al.* [184], oxygen radical functionalisation of BNNS was also reported [184]. Firstly, the exfoliated BNNS in N-methyl-2-pyrrolidone (NMP) were tertbutoxy functionalised using di-tert-butylperoxide reagent in a high-pressure autoclave at 120 °C for 12 hours. In the second stage, tertbutoxy functionalised BNNS was reacted with piranha solution (H_2SO_4: H_2O_2, 3:1) to make hydroxyl functionalised BNNS. Nanocomposites prepared by the addition of 0.1% hydroxyl functionalised BNNS to polyvinyl alcohol (PVA) showed very high elastic modulus, strength, elongation, and toughness values compared to bare PVA and non-functionalised BNNS incorporated in PVA. All the properties were enhanced due to effective load transfer in functionalised nanosheets by cross-linking of hydroxide ions with PVA and nanosheets [79].

2.6.1.3 Electron Beam Irradiation

According to *Jin et al.* [185], the h-BN specimens with reduced number of layers are prepared and thinned to a single layer *in situ* using electron beam irradiation at 120 kV inside the TEM. The single layered h-BN are prepared within a desired region in a well-controlled manner [186]. During the electron beam thinning process, many lattice defects such as vacancies are subsequently introduced, mainly due to the knock-on effect of the incident electron beam [185]. In addition, it has been reported through the studies [185] that, by means of the exit-wave (EW) reconstruction of through-focus image series, individual boron and nitrogen atoms have been

experimentally distinguished. Defects in boron nitride mono-layer created by irradiation damage, such as the dominated boron mono-vacancies and the large vacancies with nitrogen atom terminated zigzag edge, have also been atomically resolved [185].

2.6.2 Bottom-Up Approaches

Bottom-up approach is a route in which atoms are assembled in order, on a specific substrate through physical or chemical methods, and offers significant advantage for synthesising large area 2D h-BN compared to top-down methods. Among bottom-up methods, CVD is the most thoroughly explored and promising for large-scale production, which is a prerequisite for applications of 2D h-BN. Besides CVD, other novel methods have been developed for synthesising 2D h-BN during the past several years.

2.6.2.1 Chemical Vapour Deposition

Chemical vapour deposition (CVD) is a synthesis technique used to grow a thin solid film from gas source precursors. The deposition occurs when the precursor in the form of atoms or molecules, or a combination of the two is adsorbed and then coalesces on a substrate. Nucleation and growth methodologies for high-quality mono- and few-layer h-BN films, as well as many other 2D material counterparts, have been of significant interest within the past decade. h-BN mono-layer was first reported to be synthesised by CVD technique through the deposition of borazine $(B_3N_3H_6)$, on a transition metal substrate such as Pt(111) and Ru(001) in 1990 [187]. Moreover, BNNS have also been reported to be synthesised by CVD techniques starting from different precursors such as boron trifluoride and ammonia $(BF_3\text{-}NH_3)$, boron trichloride and ammonia $(BCl_3\text{-}NH_3)$, borazine $(B_3N_3H_6)$, trichloroborazine

($B_3N_3Cl_3$) or hexachloroborazine ($B_3N_3Cl_6$) [188-196]. Furthermore, borazine and its compounds are easier to use compared to BF_3-NH_3 and BCl_3-NH_3 since these precursors involve two or more gases.

Borazine ($B_3N_3H_6$) is a compound similar to benzene except the atoms are boron and nitrogen in equal ratio and therefore the two parent atoms of the final products are present in only one precursor. Thus, it is possible to avoid having to use more complicated systems using two or more gaseous precursors. It is possible to synthesise mono-layer h-BN by dehydrogenation of borazine using a transition metal substrate such as Pt(111), Ru(001), Ni(111), Cu(111), Pd(111), Pd(110), Fe(110), Mo(110), Cr(110) and Rh(111) at high temperatures [197-208].

The substrate used determine the products morphology, since the interfacial bonding between h-BN and the substrate are different [187]. For example, using Rh (111) a particular structure called BN nano-mesh is formed [188], consisting of a single corrugated layer. In low-pressure CVD, it is possible to use gases produced from BH_3-NH_3 on Cu to obtain h-BN mono-layer by nucleation of BN triangle shape islands on the substrate. In fact, at 70 – 90 °C a complete layer is formed by the little islands as they grow and merge with each other. Low precursor pressure is essential to achieve high quality 2D BN [209]. In 2010, a few layered BN films (about 2 – 5 layers) were synthesised on Cu by thermal catalytic CVD [37]. A split tube furnace was used to place the substrate at 600 °C for 20 minutes under Ar-H_2 flux. Successively BH_3-NH_3 was elevated at 120 – 130 °C and carried in the furnace by the Ar-H_2 flux. Large and flat BNNSs were obtained since BN and Cu have similar lattice structures. Theoretical calculations and experimental results have

demonstrated that 2D h-BN layers forming on 3d-transition and 5d-transition metals are weakly bound to the metallic substrates [210].

However, on 4d-transition metals, the h-BN substrate binding energy increases with the unoccupied states in the d-shell of the substrate. For instance, epitaxial h-BN mono-layer can be formed on Ni (111) [189]. Nevertheless, it is rather not easy to controllably grow h-BN and to transfer it onto other substrates, due to the complex nature of the ultrahigh vacuum (UHV) systems. Recently, both atmospheric pressure CVD (APCVD) and low-pressure CVD (LPCVD) have also been used to grow 2D h-BN on metallic substrate for the fabrication of h-BN layer by CVD during the past years [37, 211-213].

2.6.2.2 Physical Vapour Deposition

Physical vapour deposition (PVD) is a common process for growth, which can avoid the complex interrelation in growth parameters involved in the CVD process. Viewing it from this point, *Sutter et al.* [214] deposited mono- and few-layer h-BN in an ultrahigh vacuum N_2/Ar atmosphere by radio frequency (RF) magnetrons sputtering of a B target. The use of Ru (001) substrate offers an orientation of B and N species to assemble into an ordered h-BN layered film. A similar approach has been taken to synthesise h-BN film on the Au (111) substrate with 60° angle rotation between two inter-connected triangular h-BN domains [215].

The particular morphologies observed, including butterfly, diamond, and sic-apex star, implies a significant different interaction of h-BN films with the underlying substrate during the growth process. Other sputtering-based strategies such as high-energy electron irradiation [216, 217], and ion beam sputtering [218] have been exploited to prepare h-BN with controlled number of layers. There is no doubt that

these PVD techniques provide different approach towards the high-quality and wafer-scale fabrication of 2D layered h-BN, although the crystallinity of the nanosheets obtained need to be optimised, as well as the types of substrates that can be effectively employed.

2.6.3 Other Processes

Apart from the conventional bottom-up or top-down approaches, BNNSs can be synthesised by substitutional reaction of graphene [219-221]. To synthesise the nanosheets, boron trioxide powders were covered with molybdenum oxide (to act as a promoter), and graphene sheets, and all those materials were put into a graphite furnace at 1650 °C under flowing N_2 gas [222]. In the process, BN and BCN nanosheets were synthesised. Oxidising the as-obtained product at 600 °C lowered the carbon content in the sample, and high purity BNNS could be obtained. Further modification of the process by using diverse carbon sources (including any vegetation, fleabane flowers, pine needles, wiper papers, etc.) resulted in gram scale fabrication of BNNSs [223]. Epoxy composite using this gram scale BNNSs filler demonstrated a 14-fold increase in the thermal conductivity.

In addition, several researchers have tried synthesis of BNNSs by chemical reactions in solution. The first paper reported that the synthesis of BNNSs by chemical routes involves the reaction of boric acid and urea in water at 65 °C, which forms a complex in the stirred solution. After evaporating the water, the formed solid powder was heated at 900 °C to obtain few-layer BNNSs [224]. A mixture of boron trioxide and guanidine chloride in methanol was used to produce porous BNNSs at 1100 °C, which was utilised for the absorption of oil, organic solvents, and dyes in water [64]. BNNS, 4 nm in thickness on average was synthesised by mixing B_2O_3,

zinc powders, and $N_2H_4 \cdot 2HCl$ in a sealed autoclave at 500 °C [225]. In another process, $NaBF_4$, NaN_3, NH_4Cl, and S were mixed under 450 MPa pressure to form pellets. This was then kept in the autoclave at 300 °C for 1 hour to synthesise h-BN of a few nanometres thickness [215]. Nevertheless, all the attempts to prepare BNNSs by wet chemical routes encounter difficulty in terms of controlling the nanosheets thickness and purity.

2.6.4 Limitation of the Synthesis Routes and Challenges for Application

Although several synthesis routes have been identified to synthesise mono- and few-layer BNNSs, methods for production of large-scale and high-quality single crystalline nanosheets for practical use are still not available. With the top-down approaches, the nanosheets size and cleanliness are limited by the pristine powder size and purity. In the micromechanical cleavage technique, nano- to micro-meter size nanosheets can be peeled off from the pristine highly oriented pyrolytic boron nitride samples. This process has extremely low output, however, and both mono- and few-layer nanosheets are formed at the same time. This method cannot be scaled up for industrial production. In the sonication-assisted exfoliation, defective and small-sized nanosheets are often found. Functionalisation of the nanosheets prior to exfoliation can increase the efficiency of exfoliation and dispersion, although it generally induces defects in the nanosheets.

In addition, using the ball-milling process to exfoliate nanosheets creates defects and possible foreign-element contamination in the nanosheets. Small-size nanosheets are obtained, which also depend on the pristine h-BN powders. Electron beam irradiation and PVD methods have been utilised to synthesise BNNSs, although these synthesis routes are very expensive and only laboratory scale production is

possible with them. Leftover impurities in the nanosheets are the main concern with these wet chemical routes. The as-synthesised nanosheets often require very high-temperature annealing (1000 – 1500 °C) to improve the crystallinity and sometimes require oxidation to remove the carbon contamination from the nanosheets surface [60, 226].

Among all the synthesis routes, the CVD method has been established as a popular route to synthesise large BNNSs. Several years back, 30-inch-long graphene was synthesised by a CVD method through a roll-to-roll transfer technique, which demonstrated strong evidence of the reliability of this technique for large-scale production [227]. Although BNNSs has not been synthesised on such a large scale yet, by utilising the suitable gas flow of the precursor and carrier gases, as well as the right temperature, catalyst and CVD design, large-scale production of BNNSs is possible. The major bottleneck to overcome with this technique, however, is to reduce the grain boundaries (so to form large single grains) and control the mono- or few-layer characteristics (homogeneity) all over the synthesised product in the CVD system. Moreover, suitable techniques need to be developed to avoid surface contamination, which is formed during the synthesis and/or during the transfer process.

2.7 Gas detection importance and impacts

The detection of various toxic gases such as carbon monoxide (CO), nitrous oxides (NOx), methane (CH_4) and hydrogen sulphide (H_2S) etc. that might be harmful to human and agriculture which often begins to threaten livelihood at large, is important for monitoring of the environmental atmospheres. Through the scientific studies, it has been disclosed that global warming is a growing threat of the environmental

collapse in the future [228], which is influenced by some of the above-mentioned gases.

2.7.1 Importance of detecting carbon monoxide (CO)

Carbon monoxide (CO) is one of the major toxic gases that contribute to global warming. The CO gas is colourless and undetectable by humans; it is a dominant cause of poisoning in the North America (United State), which is responsible for more than 50% of fatal poisoning disclosed by many industrial countries [229-231]. South African is amongst the nations that possesses the energy and carbon intensity economy, with almost 91% of the electricity generated in the nation is from coal, which result in the emission of toxic gases such as CO [232] that have created high environmental and health problem in affected areas with large industrial presence. The gas is known to bind irreversible to the iron centre of haemoglobin, the oxygen transport molecules in blood, and that leads to the difficulty in oxygen absorption, which at elevated levels of vulnerability can result in death [233]. The CO gas is the result of poorly combusted organic materials, such as fuels. CO concentrations are specifically rising in area of industry, where the energy production result from the combustion of fossil fuels and lastly in areas where there are elevated levels of traffic. Exposure to high levels of the gas is injurious to human health. In addition, the gas is obtained in domestic areas due to the faulty gas-powered boilers, which leads to the CO poisoning deaths annually; again, it has also been reported to cause dizziness and confusion in high concentrations [234].

2.7.2 Importance of detecting nitrous oxides (NOx)

Nitrous oxides (NOx) gases result from the combustion of fossil fuels in internal combustion of engines, which is due to the combustion reaction of N_2 and O_2 [235].

There are a variety known groups of NOx gases such as nitric oxide (NO), nitrogen dioxide (NO_2), nitrous oxide (N_2O), dinitrogen trioxide (N_2O_3), dinitrogen tetroxide (N_2O_4) and dinitrogen pentoxide (N_2O_5) [235]. Nitric oxide is a known photochemical smog that is irritating to the eyes and damages plant lives in affected area, emanating from the combination of hydrocarbons and oxygen to create a compact smoke over heavily industrial areas. On the other hand, NO_2 appears to be risky due to its effects on the lungs, where people living with diseases such as asthma are particularly at high risk upon the inhalation of the gas, leading to the inflamed lungs that may result in difficulties in breathing [235]. Animals with long-term exposure to NO_2 were found to have damaged lungs [235]. Based on the impacts that NOx gases bring to the environment, it appears to be important to monitor the concentrations of any NOx gas in the air, thus to monitor the toxic gases, as a result this will provide an opportunity to air quality regulator and environmental agencies to predict how likely a smog is to form [235]. This will particularly reduce the pollution of the atmosphere and therefore improve human health, growth of crops and decrease rising of the toxic gases in areas where such gases begin to threaten livelihood.

2.7.3 Importance of detecting methane (CH_4)

Methane (CH_4) gas is one of the carbon compounds gases known to exist in the atmosphere. This gas result from the decomposition of the dead plants and animals. During decomposition, the carbon is released to the air as CH_4 or stored in the soil [236]. The burning of CH_4 results in the production CO_2 gas as another known carbon compound, which as well fall within the monoxide toxic family gases [236]. CH_4 is known to reduce the amount of oxygen breathed from the air, which can result in a number of human health difficulties such as vision problem, memory loss,

vomiting, nausea and headache. These complexities in turn lead to the changes in heart rate, balance problems and unconsciousness in particular [237]. As a results of the impacts that CH_4 brings to the environments and to all living being at large, it is quite important to monitor the levels of CH_4 in the atmosphere, as to reduce the risks of above-mentioned related illnesses.

2.7.4 Importance of detecting hydrogen sulphide (H_2S)

Hydrogen sulphide (H_2S) is a colourless, highly flammable and explosive toxic gas, which is produced naturally by decaying organic matters and by certain industrial processes [238]. Exposure to the high concentration of H_2S can cause inhibition of the cytochrome oxidase enzyme system, resulting in lack of oxygen use in the cells. The ultimate consequences are rapid unconsciousness, which may lead to death [238].

2.7.5 Sensing properties of 2D h-BNNSs

There are various nanomaterials fabricated for sensing the above-reviewed gases such as metal oxides nanomaterials: ZnO, TiO_2, WO_3 and In_2O_3 [239, 240] and other carbon-based nanomaterials etc. [42] that have been tested. However, due to ineffectiveness of some as they often suffer from low sensitivity, slow response time, poor gas selectivity and slow recovery time, they tend not to be effective as good gas sensors. BN has been verified to be a good sensor device both theoretically and experimentally. In particular, BNNTs have been theoretically studied for various gas detection, but due to their small surface area, they tend to be less sensitive to certain gas molecules [241]. A point to note, as stipulated in the rationale of this study, 2D h-BNNSs were experimentally verified [241] to be good gas detectors. Lastly, these nanosheets demonstrate the property of operating where most materials fall short.

2.8 Standard performance and working principles of different sensors

A gas sensor is a device which detects the presence or excess concentration of harmful gases in the atmosphere. Based on the detected amount of concentration of the harmful gas, the sensor produces a signal which may be a light spark, change in potential difference or electric current, or change in colour on the device or sensor material. Such a signal occurs when the harmful gas molecules are in contact or adsorbed on the device material sample triggering a disturbance in the original local environment. There are various types of gas sensors, of which are but not limited: optical gas sensors, electrochemical gas sensors and semiconductor-based gas sensors etc. Optical gas sensors are one of the most widely used sensors, both in homes and industrial segments, which determines the detection of a gas component by utilising absorption, fluorescence, scattering, reflection of light, and changes in refractive index and optical path length. Such signal occurs when the harmful gas molecules are adsorbed on the sensor device material. However, optical gas detectors face several key challenges, which include sensitivity, specificity, interferant discrimination, response and recovery time, background drift, and aging [337]. Similarly, electrochemical sensors are as well, widely used sensors, for the detection of toxic gases. Electrochemical sensors are operated based on the diffusion of gas of interest into the sensor, which results in the production of an electrical signal that is proportional to the gas concentration. Electrochemical sensors are widely used in confined spaces such as monitoring indoor air quality and gas leaks, and with portable instruments consisting of multiple sensors [338]. While on the other hand novel semiconductor-based gas sensors are ideal for next generation of sensors for long term stability, high surface to volume ratio, better gas selectivity and self-heating capacity, and can also operate in various environments

where properties of other materials fall short. So, the challenge is to fabricate semiconductor-based sensor device with improved sensitivity, reduced power consumption and relatively lower limit of detection as well as relatively lower operating temperature [40]. As part of the objectives, the production of semiconductor-based gas sensor, should not only focus on the performance of the sensor, rather also on the cost effective manufacturing process to acceptable and sustainable standards.

Chapter 3

Methodologies and Characterisation Techniques

3.1 Introduction

In this chapter, both the computational and experimental methodologies that are adopted in this study are discussed. The computational study make use of classical molecular dynamics (MD) simulations to investigate the structural, optical and electrical properties of white graphene [241]. This simulation methods are good in explaining and predicting numerous properties of the materials in solid and liquid phases.

Tersoff potentials were employed to explain the interactions between the B and N atoms of 2D h-BNNSs/white graphene using the DL_POLY computer code [242]. Calculations were performed in the NVT Evans and NPT hoover ensembles for comparison. The Verlet leapfrog (VL) algorithm [3], which uses accelerations, velocities, positions and time to calculate new positions, was used to integrate the equations of motion.

This makes molecular dynamics to be systematic because if we know the accelerations, velocities, positions and time at previous steps we can predict the properties of the atoms and molecules at a later time [243]. In the experimental part of the work, in order to provide an accessible methodology to grow 2D h-BNNSs/white graphene, chemical vapour deposition (CVD) family techniques were extensively explored for their ability to control the lateral size, number of layers, as well as the crystalline structures precisely [37]

3.2 Computational method

3.2.1 Classical molecular dynamics

Compared to the first-principle quantum mechanics, classical MD [244] simulation is an empirical method which is easy to implement in large systems (millions to billions of atoms). The classical MD method was first proposed by Alder and Wainwright [245], and up to now it is the most powerful and popular tool for investigating the equilibrium, transport and mechanical properties, together with the structural deformation of classical many-body systems. It is used to predict the structural, dynamics and kinetic properties at certain conditions such as pressure and temperature [241].

It is a fully deterministic method, based on the numerical solution of Newton's equations of motion, to calculate the positions and velocities of atoms. The basic concept of the method is to simulate the time evolution of a system. It describes a system's atomic-scale dynamics, in which atoms and molecules move while interacting with many of the other atoms and molecules in the vicinity. The method relies on a mathematical description of total energy of the system as a function of all atomic coordinates. Atoms in the system are treated as point-like masses that interact with each other according to a given potential energy $E(r_1, r_2,. . .,r_N)$, where r_j is the position vector of the jth atom and $j = 1, 2 ... ... N$.

The evolution is computed at every time-step, and the instantaneous location and velocity of each atom are then determined by solving the Hamilton's classical equation of motion from Newton's second law. Such that:

$$F_i = m_i \times \frac{d^2 r_i}{dt^2} = -\nabla_i E(r_1, r_2, ..., r_N) \qquad \text{3.1}$$

where m_i and r_i are the mass and spatial coordinates of the ith atom, respectively, E is the empirical potential energy for the system, and ∇ denotes the spatial gradient. Due to the small scale involved, explicit integration algorithms, such as the Verlet method [246] and other high-order methods, are commonly used to ensure a high order of accuracy.

3.2.2 Tersoff potentials

The reliability of a MD simulation depends on the use of an appropriate potential model. *Allinger et al.* [247-250] and his colleagues developed a molecular mechanics (MM2) force field and an improved version known as the MM3 force field. These methods are designed for a broad class of problems in organic and inorganic

systems. *Abell et al.* [251] proposed the quantum-mechanical concept of bond order formalism for carbon nanotubes (CNT's) characteristics. Using Morse-type potential, Abell showed that the degree of bonding universality could be well maintained in molecular modelling for similar elements.

Tersoff [252, 253] introduced the concept for the modelling of group four elements such as carbon, silicon, and germanium, and reasonably accurate results were reported. *Nordlund et al.* [254] modified the Tersoff potentials such that the interlayer interaction is also considered. The Tersoff potential is a three-body potential functional, which explicitly includes an angular contribution of the force. Within the Tersoff potential, the total potential energy E_{tot} of the system composed of N atoms is written in the form:

$$E = \sum_i E_i = \frac{1}{2} \sum_{i \neq j} V_{ij}$$

3.2

with

$$V_{ij} = f_c(r_{ij})[V_R(r_{ij}) + b_{ij}V_A(r_{ij})]$$

3.3

such that the total energy is given as:

$$E_{tot} = \frac{1}{2} \sum_i^N \sum_{i \neq j}^N f_c(r_{ij})[V_R(r_{ij}) + b_{ij}V_A(r_{ij})]$$

3.4

with the pairwise repulsive and attractive contributions respectively given by:

$$V_R(r_{ij}) = Ae^{(-\lambda_1 r_{ij})}$$

3.5

$$V_A(r_{ij}) = -Be^{(-\lambda_2 r_{ij})}$$

3.6

Here, A, B, λ_1 and λ_2 are adjustable parameters

The cut-off function $f_C(r)$ is defined as:

$$f_c(r) = \begin{cases} 1, & for\ r < R - D \\ \frac{1}{2} - \frac{1}{2} sin\left(\frac{\pi}{2}\frac{r-R}{D}\right), & for\ R - D \leq r \leq R + D \\ 0, & for\ r > R + D \end{cases} \qquad 3.7$$

and acts in such a way as to restrict the interaction range. The cut-off function smoothly cuts the contributions from pairs of atoms, which are separated by more than $R + D$. R and D are also adjustable parameters, which specify the position and the width of the cut-off region. They are typically chosen in such a way to include only the first coordination shell in the summation presented in equation 3.2. Another summation, which is also limited by $f_C(r)$, appears in the definition of the bond order b_{ij}, which is given as:

$$b_{ij} = \left(1 + \beta^n \zeta_{ij}^n\right)^{-\frac{1}{2n}} \qquad 3.8$$

where

$$\zeta_{ij} = \sum_{k \neq i,j}^{N} f_c((r_{ik})h(r_{ij} - r_{ik}) g(\cos\theta_{jik}) \qquad 3.9$$

The $h(r)$ function is defined as:

$$h(r) = e^{(\lambda_3^m r^m)} \qquad 3.10$$

Symbols β, n, λ_3 and m represent other parameters. Due to the non-linearity present in the definition of the bond order (Equation (3.8)), the Tersoff bond order b_{ij} is a many-body term, involving the relative nearest neighbor distances of the coordination number of atoms. The function $(\cos\theta)$ describes the angular dependence and is defined as:

40

$$g\left(\cos\theta\right) = \gamma\left(1 + \frac{c^2}{d^2} - \frac{c^2}{d^2 + (\cos\theta + \cos\theta_0)^2}\right) \qquad 3.11$$

The angular function $(\cos\theta)$ is determined by the parameters γ, c, d and θ_0. Therefore, fourteen parameters in total need to be specified for a single element system. There are many different parameterisations of the Tersoff potential available in the literature, mostly for elements of group IV [252, 253, 255-257]. However, some parameterisations for elements of groups III and V also exist [258-260,261, 244, 245]. These set of parameters are modified to describe the interactions between B and N of h-BN system in our studies. Furthermore, such parameters are used to study the thermal transport and mechanical properties of more complex materials such as hybrid graphene-boron nitride or graphitic carbon nitride [262, 263].

3.2.3 DL_POLY computational processes

As already explained above that, classical molecular dynamics (MD) is a computational method used to study the motion of atoms and molecules in a system. In setting and running a molecular dynamics simulation, the first task is to decide which energy model to use to describe the interactions within the system. Then the initial configuration has to be chosen in such a way that it favours the potential model used.

Classical molecular dynamics simulations have been performed in this work using the DL_POLY [258] computer cope to study the various physical properties of 2D h-BNNSs/white graphene. For a DL_POLY calculation to take place, three files are required in setting the parameter of the material, which are the CONTROL, CONFIG and FIELD files. The CONTROL file is where the algorithms directives on how the calculations should run and what to expect as outputs are set; such as timestep,

period, equilibration, the cut-off parameters, the radial distribution functions (RDF) prints together with the state of the system (ensemble).

The CONFIG file contains the information about the crystal structure, which includes lattice parameters and the atomic positions, velocities and forces of the material, and lastly in the FIELD file a set of chosen atomic potential parameters used on the system defined in the CONFIG file are defined. The Verlet leapfrog (VL) algorithm has been adopted throughout the calculations to integrate equations of motion, by so doing the properties of 2D h-BNNSs/white graphene are studied. Tersoff potentials have been used to accurately reproduce the interactions between the Boron (B) and Nitrogen (N) atoms within a BN system [253].

The calculations are based on the canonical ensemble (NVT Evans) and isothermal-isobaric ensemble (NPT hoover). From the output files, the radial distribution functions (RDF) and structure factors (SF) were plotted to understand the structural configurations whilst the mean square displacements (MSD) were plotted to determine the diffusion constants. The motive to perform simulations in canonical and isothermal-isobaric ensembles but not in micro-canonical ensemble is that, simulations are easily done in micro-canonical ensemble and produce the correct results, however it describes an isolated system, that only performs the constant energy experiments which does not bring us into a real-life situations [264]. Simulations performed at constant temperature and constant pressure come closer to real life situations, and both the NVT and NPT ensembles describe them. Additionally, simulations in the NVT ensemble are performed by keeping the number of particles, volume and temperature constant, which are distinguished by mainly two

approaches: coupling the system to a heat bath and rescaling the velocities accordingly or make use of the extended phase approach.

Simulations in the NPT ensemble are performed such that the volume of the system is adjusted in a way that the average internal pressure is the same as the applied external pressure *Slotman et al.* [265]. Three supercells of about 144 atoms (72 B and 72 N atoms), 324 atoms (162 B and 162 N atoms) and 576 atoms (288 B and 288 N atoms) were modelled for the examination of 2D h-BNNSs/white graphene intended properties. A vacuum between the layers was created by creating an interlayer spacing of 7.900 Å in all the three systems. The MD simulations were allowed to run with a 0.001 ps timestep, for a period of 5000 steps and an equilibration after every 500 steps. On the existing knowledge, no conclusive study has been made so far, on the effects of temperature on the stability and structural properties of pristine and defective mono-layer h-BN with an increase in the surface area.

3.3 Experimental Method

3.3.1 Reagents used for the synthesis of 2D h-BNNSs

The reagents used in this study were purchased from Sigma Aldrich. The reagents are: Boric acid (H_3BO_3 99.5%) and urea bioxtra ($CO(NH_2)_2$ 99-100.5%) with (PH 7.5 - 9.5) as B and N precursors, nitric acid (HNO_3 10%) deionised water (H_2O), ethanol (C_2H_6O 99.9%) and nitrogen gas (N_2).

3.3.2 Synthesis of 2D h-BNNSs

In order to provide an accessible methodology to grow 2D h-BNNSs/white graphene, a catalyst free wet chemical reaction synthesis technique has been extensively explored for its ability to control the lateral size, number of layers, as well as the

crystalline structures precisely [35]. Additionally, the approach is preferred for its capability to avoid the transfer of the as-deposited 2D h-BN to the target substrate for consecutive characterisation or device fabrication [37, 266], which can result into the sample damage or film contamination. The BNNSs were synthesised over a reaction of boric acid (H_3BO_3) and urea ($CO(NH_2)_2$) as B and N precursors [267] at 800, 900 and 1000 °C under N_2 atmosphere [268] to examine the effect of temperature on the synthesis of the nanosheets. The reactions included are:

$$2H_3BO_3 \rightarrow B_2O_3 + 3H_2O \qquad\qquad 3.12$$

$$CO(NH_2)_2 \rightarrow NH_3 + NHCO \qquad\qquad 3.13$$

$$B_2O_3 + 2NH_3 \rightarrow 2BN + 3H_2O \qquad\qquad 3.14$$

The number of layers can be accustomed by the reaction concentration [269]. During the synthesis of h-BNNSs, a mole ratio of 1:2 of H_3BO_3 (4g) and $CO(NH_2)_2$ (8g) were dissolved into deionised H_2O of 20 ml in a 250 ml beaker to give a solution with high homogeneity [270]. The solution was then allowed to stir for 3 hours at 60 °C at a speed of 300 rpm (revolution per minutes) until the solid samples have completely dissolved in deionised H_2O.

After the full complete 3 hours reaction, the sample was then dehydrated in an oven drier for 24 hours at 110 °C to get a solid sample. The obtained sample was then crashed into a desired powdered form. Three (3) samples of 3 g (grams) each were then measured and transferred into the quarts substrates boards then into the quarts tubes to the muffle furnace for heating under N_2 atmosphere as shown in Figure 3.1 below. Figure 3.2 represents the dynamic visualisation of the experimental set-up for the synthesis of the nanosheets. Before heating can start, the N_2 gas was allowed to

run for 10 – 15 minutes to clear any unwanted gases (such as oxygen) inside the quarts tubes to reduce the risks of impurities on the nanosheets. The samples were then heated at 800 °C for 3 hours with a stepwise heating rate, at a flow rate of 0.5 l/min of N_2 gas. The obtained h-BN was then washed with hot deionised H_2O once, followed by diluted 10% HNO_3 for several times in order to remove the impurities. Subsequently, 3 mg of h-BNNSs was exfoliated by sonication and blender in a 300 ml beaker of deionised H_2O to yield several h-BN nanosheets. Finally, the product was washed with absolute C_2H_6O to remove H_2O, and dried it at 60 °C for 12 hours. The same procedure was then repeated for samples fabricated at 900 and 1000 °C.

800 °C step-wise heating rate						
0	600	600	700	700	800	800
			Temperature (°C)			

900 °C step-wise heating rate						
0	700	700	800	800	900	900
			Temperature (°C)			

Fume hood

Muffle furnace

Quarts

Gas flow

Gas flow

Samples

N₂ gas
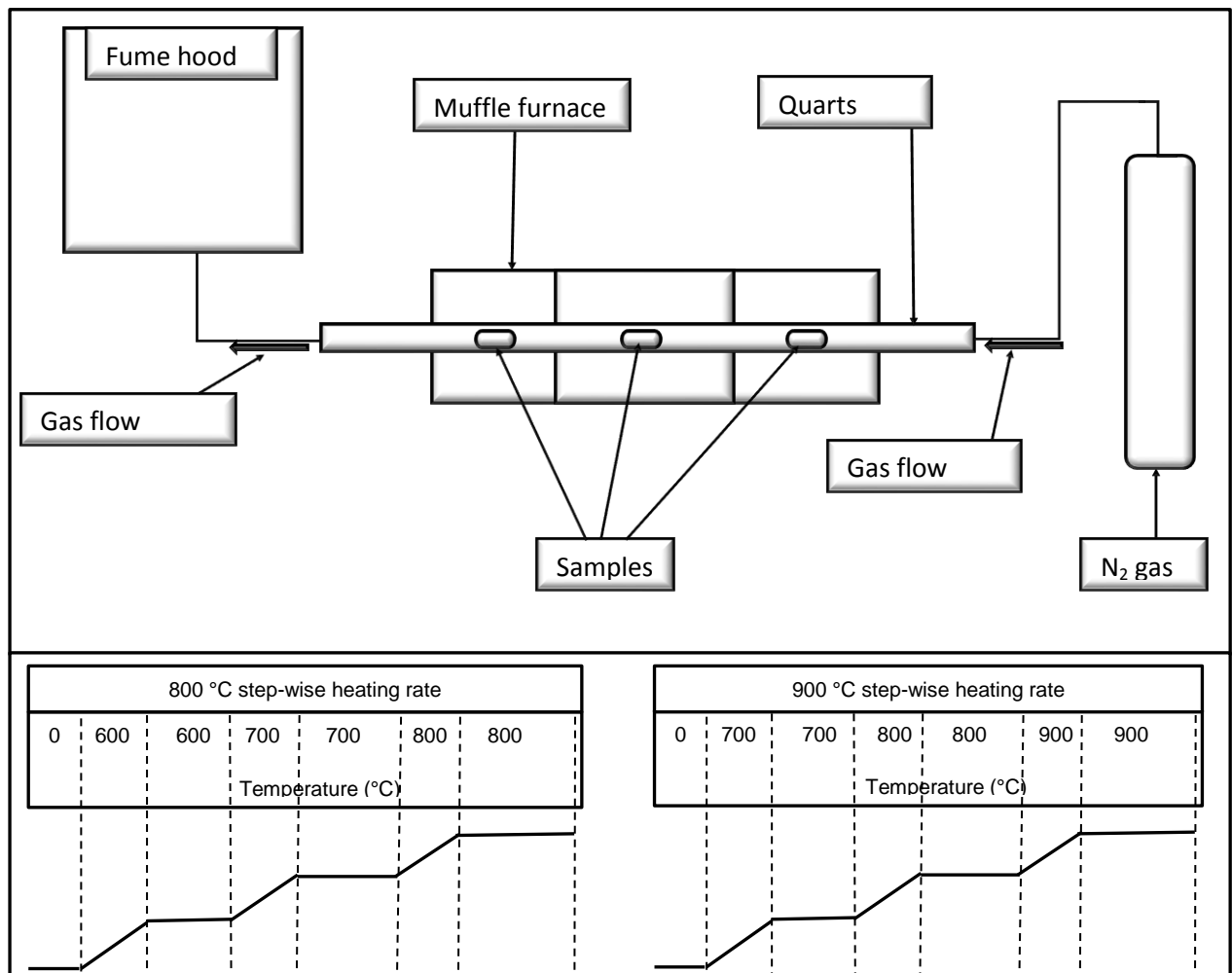
Figure 3. 1: CVD experimental representation together with the dynamic step-wise heating rates for the synthesis of the h-BNNSs at 800, 900 and 1000 °C temperatures.
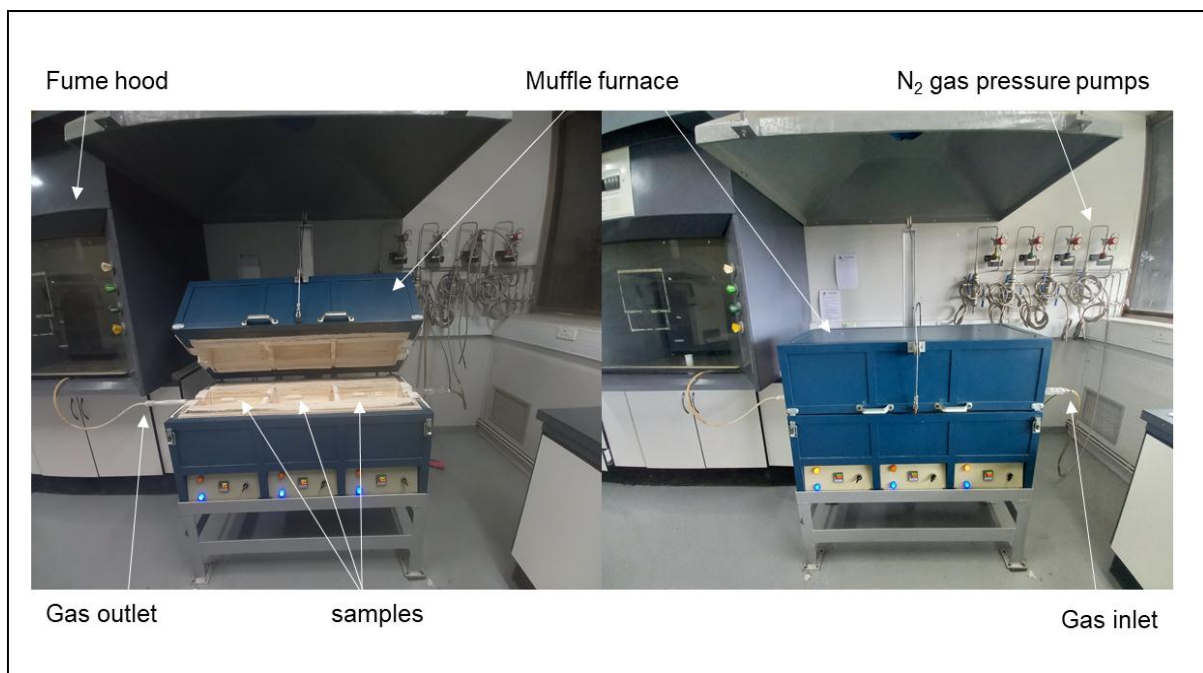
Figure 3. 2: The dynamic visualisation of the CVD experimental set-up for the synthesis of the h-BNNSs respectively.

3.6 Characterisation Techniques

3.6.1 X-Ray Diffractometer

The X-ray powder diffraction is an instrument used for the structural analysis of the samples as depicted in Figure 3.3. X-ray diffraction pattern of h-BNNSs for all the three synthesised samples at 800, 900 and 1000 °C were analysed using the Bruker D8 advanced Diffractometer (λ = 0.05 – 0.2 nm) which uses the cobalt radiation source equipped with Lynx-eye XE detector operated between 5 and 80 2θ angles. The obtained diffraction patterns were collected with an X-ray gun operating at 40 kV and 20 mA. The samples were run in powder form inside an amorphous silicon holder, where after, the nanomaterials identifications was surveyed through the comparison with those h-BNNSs in literature [270-272]. In the X-ray diffraction instrument, an incident X-ray beam is focused into a crystalline specimen, which diffract it according to the Bragg's law shown in the equation:

$$n\lambda = 2dsin\theta$$
3.15

where *n* is the order of diffraction, *λ* is the X-ray wavelength, *d* is the spacing between two consecutive crystal phase planes and *θ* is the diffraction angle at which the specimen is orientated. Furthermore, the crystalline size of the nanosheets was determined using the Debye-Scherrer's equation [273] as follows:

$$D = \frac{k\lambda}{\beta cos\theta}$$
3.16

where D is the crystalline size, K is the constant (K = 0.9), λ is the wavelength of the incident X-ray, $β$ is the full width at half maximum (FWHM) in radians and θ is the Bragg's angle in radians.

Figure 3. 3: The visualisation of the X-ray diffractometer instrument used to analyse the structural properties of the nanosheets.

3.6.2 Fourier Transform Infrared Spectroscopy

Fourier Transform Infrared Spectroscopy (FTIR) is an instrument used to analyse the chemical bonds and functional groups present in a given sample. In FTIR analyses, Infrared light from the light source passes through a Michelson interferometer along the optical path. The Michelson interferometer comprises a beam splitter, moving mirror, and fixed mirror. The light beam split into two by the beam splitter is reflected from the moving mirror and fixed mirror, before being recombined by the beam splitter. As the moving mirror makes reciprocating movements, the optical path difference to the fixed mirror changes, such that the phase difference changes with time [339]. The light beams are recombined in the Michelson interferometer to produce interference light as represented in Figure 3.4. The intensity of the interference light is recorded in an interferogram, with the optical path difference recorded along the horizontal axis with the interferogram frequency following equation 3.17.

$$f = \frac{2v_m}{c} U, \qquad\qquad 3.17$$

with mirror velocity of

$$v_m = \frac{\delta}{2t}, \qquad\qquad 3.18$$

where

$$\Delta v = \frac{1}{\delta}. \qquad\qquad 3.19$$

In this research, the Perkin Elmer FTIR TWO spectrometer was used, operating at a spectral wavenumber ranging from 400 to 4000 cm^{-1} with a resolution of 4 cm^{-1}. The presence of the in and out-of-plane bending vibrations of h-BNNSs for all the three

synthesised samples at 800, 900 and 1000 °C were determined and the measurements were performed over a broad spectrum instead of narrow frequencies. The vibrational identification was finalised by comparison with the h-BNNSs reported in the literature.

$$\Delta \upsilon = \frac{1}{\delta}$$
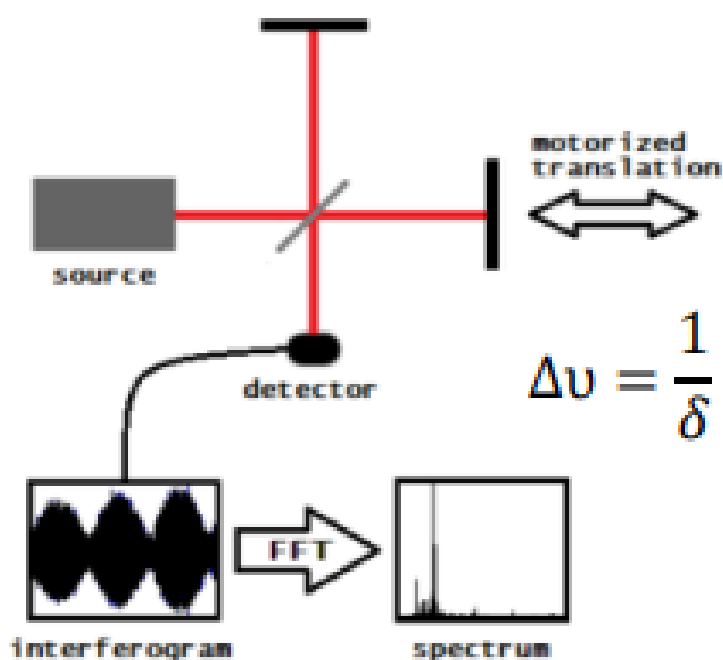
Figure 3. 4: A schematic representation of principles of FTIR spectroscopy [339].

3.6.3 UV-vis spectroscopy

UV-vis spectroscopy is an instrument used to analyse the optical properties of synthesised thin films. The technique used in the measurement of absorbance of light across ultraviolet and visible regions. When the incident light strikes the sample, it is usually reflected, transmitted, or absorbed as in Figure 3.5. The absorbance of light causes the transition of molecules from the ground state to the excited state. Making use of the UV-Vis spectrophotometer, the intensity and excited states of light the absorbed by the studied samples can be measured [340]. The instrument used in

this study was the Thermo Fisher Scientific UV-vis spectroscopy, operating at a wavelength of 365 nm, with a spectrum collected in a wavelength range of 230 – 850 nm for all the samples synthesised at 800, 900 and 1000 °C. The UV-vis spectrum was obtained when the electromagnetic radiation of a diverse wavelength was ideally irradiated on to the samples. The monochromatic radiation operating at +20VDC/ 4A was employed to ideally emanate through the sample and obtain the optical properties of a sample from the reflected light. The position of the maximum absorption band called λ-max, and the intensity of the bands are the two major parameters used to characterise the UV spectra of substances [274]. The sample was prepared by dissolving a small portion of h-BN into deionised water, and then sonicated for the sample to completely dissolve in to water, then after taken for characterisation. The energy band gaps of the materials are calculated using the Tauc relation method for determination of the band gap energies using the UV-vis data [275]. The Tauc method is based on the assumption that the energy-dependent absorption coefficient α can be expressed by the following equation 3.20:

$$(a.hv)^{1/\gamma} = B(hv - E_g)$$
3.20

Where h is the Plank constant, v is the photon's frequency, E_g is the band gap energy, and B is a constant. The γ factor depends on the nature of the electron transition and is equal to ½ or 2 for direct and indirect transition band gaps respectively [335, 336].
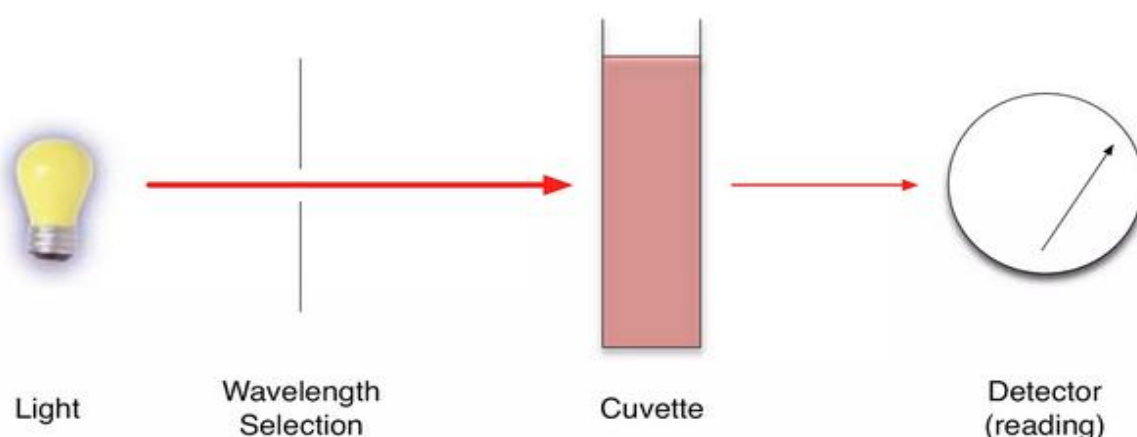
Figure 3. 5: A schematic representation of the working principle of UV-Vis spectroscopy.

3.6.4 Dynamic Light Scattering

Dynamic light scattering (DLS) is an instrument used to determine the particle size and electro-kinetic zeta potential of a sample. As with the other characterisations, the instrument ZETASIZER Nano-Series analyser was applied on the synthesised samples at 800, 900 and 1000 °C. In DLS, when a monochromatic beam of light encounters solution-containing macromolecules, light is scattered in all directions as a function of the size and shape of the macromolecules. Therefore, the detected intensity fluctuates because of the Brownian motion of macromolecules in the solution, and the scattered light is analysed. Thereafter, the diffusion coefficient (D_T) that is related to hydrodynamic size of macromolecules can be obtained [276-278]. In order to determine the particle sizes, the samples were prepared by dissolving small portions of h-BN nanosheets powders into deionised water. Thereafter, sonicated in order for the samples to completely dissolve in water. The entire solutions were later considered for particle size measurements.

3.6.5 High Resolution Transmission Electron Microscope

High Resolution Transmission Electron Microscope (HRTEM) is an instrumental analysis used for the determination of the particle size and morphology of nanomaterials. In this study, the JOEL 2100F, JEM-200 kV transmission electron microscope operating at 200 kV as depicted in Figure 3.4 was used for morphology analysis of the h-BNNSs fabricated at 800, 900 and 1000 °C. HR-TEM analysis also allows the determination of the lattice spacing and their direction, however, is not precise. Generally, in TEM, an electron beam enters the solid sample in a vacuum and is detected on the other side of the sample as the secondary transmitted electrons. The secondary electrons detected, produce images, which have information about the extent of penetration in a sample [279]. Furthermore, in the current study, h-BNNSs were dispersed in water and droplet of a liquid sample were placed on a copper grid coated with a fomvar-film and carbon; afterwards the grid was dried and taken into the TEM instrument for analysis.
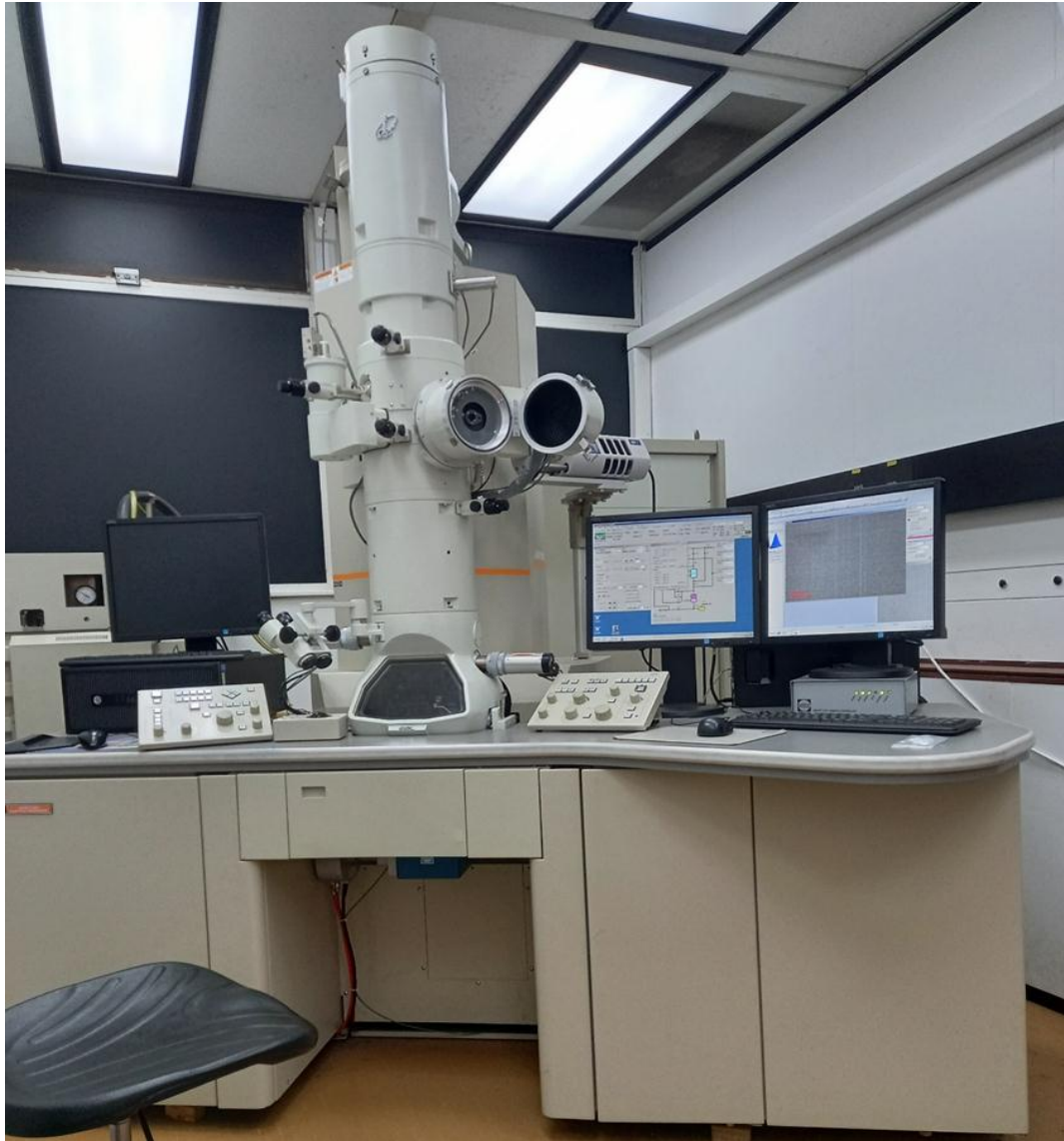
Figure 3. 6: The visualisation of the HR-TEM that was used to capture 2D h-BNNSs nano-films

3.6.6 Raman spectroscopy

The Raman spectroscopy (RS) is essential to analyse the crystal quality of 2D materials. When light interacts with molecules in a gas, liquid, or solid, many of the photons are dispersed or scattered at the same energy as the incident photons. This is described as elastic scattering, or Rayleigh scattering. A small number of these photons, approximately 1 photon in 10 million will scatter at a different frequency

than the incident photon [341]. This process is called inelastic scattering, or the Raman effect, named after Sir C.V. Raman [342], who discovered this and was awarded the 1930 Nobel Prize in Physics for his work. The Raman system allows the user to collect the vibrational signature of a given sample, giving insight into how it is put together, as well as how it interacts with other molecules around it as represented in Figure 3.7. A Horiba Scientific Raman Spectroscopy (HSRS) version of the machine was used with a visible light excitation wavelength of 532 nm, operating at a spectral wavenumber ranging from 80 to 3500 cm^{-1}. The Raman signal is known to be thickness dependent, and the shift of the Raman peaks can be used for the thickness determination of atomically thin nanosheets [280]. The presence of the E_{2g}, mode which are known to be Raman active, were used for the thickness identification and prediction of the number of layers for all the three synthesised samples and the measurements were performed over a broad spectrum instead of narrow frequencies.
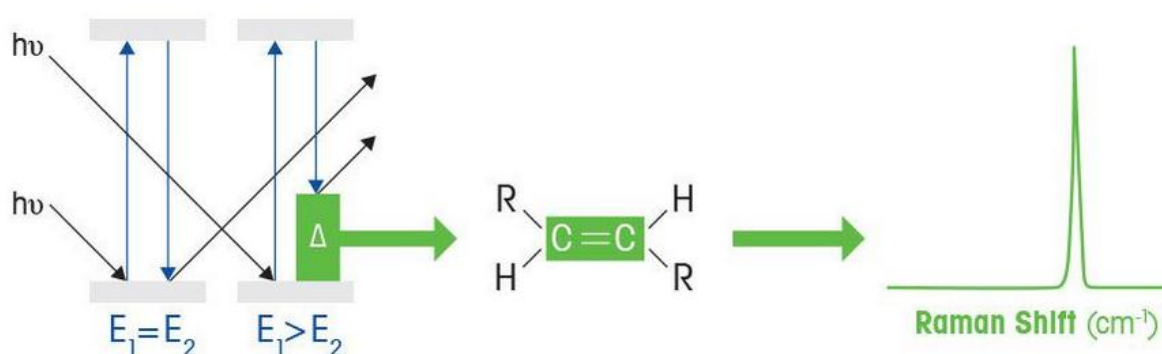
Figure 3. 7: A schematic representation of principles of Raman shift.

3.6.7 Brunauer Emmett Teller (BET)

The Brunauer Emmett Teller (BET) instrumental analysis is used to examine the surface area of nano-materials. The surface area of the fabricated nanosheets at

three different temperatures was characterised using Brunauer-Emmett-Teller (BET) Micrometrics TRISTAR 3000. The amount of gas adsorbed usually depend on the exposed surface area but also on the temperature, gas pressure and strength of interaction between the gas and the solid. During the surface area examination, nitrogen is usually used due to its availability in high purity and its strong interaction with most solids. After the complete analysis, the data collected is displayed in a form of BET isotherms, which plots the amount of gas adsorbed as function of the relative pressure [281].

Chapter 4

Molecular dynamics studies of h-BN nanosheets

4.1 Introduction

Classical molecular dynamics (MD) simulations play an important role in modelling of materials properties and processes for a better understanding of their applications. The approach is applicable and transferable across the fields of physics, chemistry, material science, nanotechnology and engineering [282]. In addition, the study of mechanical, optical, elastic and electrical properties of materials is important for different industrial applications. Certain studies have suggested that h-BN and its derivatives have better mechanical properties over the layered pristine graphene [283] and are used in the production of nano devises and nano electronics. Naturally,

h-BN is thermally stable and chemically inert in air up to 1500 °C. Different researchers using various approaches have successfully investigated the mechanical robustness of h-BN. *Srivastava et al.* [284] have effectively used the *ab anitio* density functional theory (DFT) to study the structural defects in h-BNC$_2$ sheets. The DFT approach is known to be more accurate than the classical molecular dynamics simulations at electronic level; however, it only accumulates a few hundreds of atoms due to non-trivial nature of calculations involved and memory effects. The study of the 2D materials along with the corrugation of their atomic surface needs more computational costs [282]. One of the advantages of MD is the ability to handle more atoms (up to millions) and the incorporation of the anharmonicity through the empirical potential, which is a crucial phase of atomic mobility in 2D materials [285]. On the existing knowledge, no conclusive study has been made so far, on the effects of temperature on the stability and structural properties of pristine and defective mono-layer h-BN with an increase in the surface area. Furthermore, the study on the effects of vacancy defects on mono-layer h-BN as the surface area expands were also considered. Particularly, this section report on the modelling of the structural and thermal properties with consideration of the native defects in mono-layer h-BN.

4.2 Results and Discussion

4.2.1 Structural properties of h-BNNSs

4.2.1.1 Radial Distribution Functions and Structure Factors

The radial distribution function (RDF) or pair correlation function is a powerful tool to analyse the structural information of a material. It is estimated by considering the average distance between all pairs of atoms in a given material. In general, if $g_{AB}(r)$

is the radial distribution function, then $g_{AB}(r)r$ is proportional to the probability of finding an atom of type *B* at a distance between *r* and *r* + Δr from an atom of type *A* [286] where *B* and *A* represents B and N atoms. For a two-dimensional system, the equation would be:

$$g_{AB}(r) = \frac{\Delta n_{AB}}{2\pi r \Delta r \rho_B}$$
4.1

where ρ_B is the average density of species *B* in the entire material and Δn_{AB} is the average number of particles of type *B* present in the angular region between *r* and *r* + Δr with an *A* atom at the centre (equation 4.1). The averaging is over all the *A* atoms present in the simulation volume. The radial distribution functions must be delta functions at 0 K, as there are unique values for the radii of the various neighbouring shells. However, due to thermal vibrations, these distances become blurred as the temperature of the system increases. The delta functions broaden into smooth peaks. The peak width increases with temperature. The width is in fact proportional to the root mean squared displacement of the atoms from their equilibrium position. The position of the nth peak in $g_{AB}(r)$ would correspond to the mean distance of the *B* atom from the *A* atom in n^{th} neighbour positions. Thus, the value of $g_{AB}(r)$ at any *r* decreases as the temperature increases due to thermal broadening [286, 40]. Structural properties of mono-layer h-BN have been precisely analysed using the radial distribution functions ($g_{AB}(r)$) and structure factors *(S(k))*. The observed sharp peaks, separations and heights in Figure 4.1, are all the characteristics of a lattice structure exhibited by a solid material. In the $g_{AB}(r)$ of nanosheets, the peak positions (abscissa values) correspond to the first neighbor, second neighbor, and other neighbor distances between the atoms of the hexagonal atomic system on the plane sheet.

Table 4.1 depicts the peak positions of first and second neighbour distances of h-BN144 at equilibrium temperature of 300 K. The peak positions of h-BNNSs144 atomic positions for the B-B, first and second nearest neighbour distances appear at 2.47 and 2.69 Å respectively. In the same manner, B-N first and second nearest neighbour distances appear at 1.41 and 2.81 Å respectively. Likewise the N-N, first and second nearest neighbour distances appear at 2.47 and 2.69 Å. For h-BN324 and h-BN576 supercells, the reader is referred to Appendix 2 Table 1. The B-N bond lengths of pristine mono-layer h-BN nanosheets were respectively found to be 1.41 Å, 1.44 Å and 1.44 Å for 144, 324 and 576 atoms supercells. Obtained results concur well with various studies on h-BN nanosheets as reported by *Thomas et al.* [286] and many bulk h-BN studies [287, 288]. A typical visualisation of the h-BN mono-layer (nanosheet) at 300 K is shown Figure 4.2. Here the hexagonal honeycomb with alternating B and N atoms [289-294] is evident in Figure 4.2(a). Further on Figure 4.2(b) present the same visual perpendicular to the nanosheet plane.
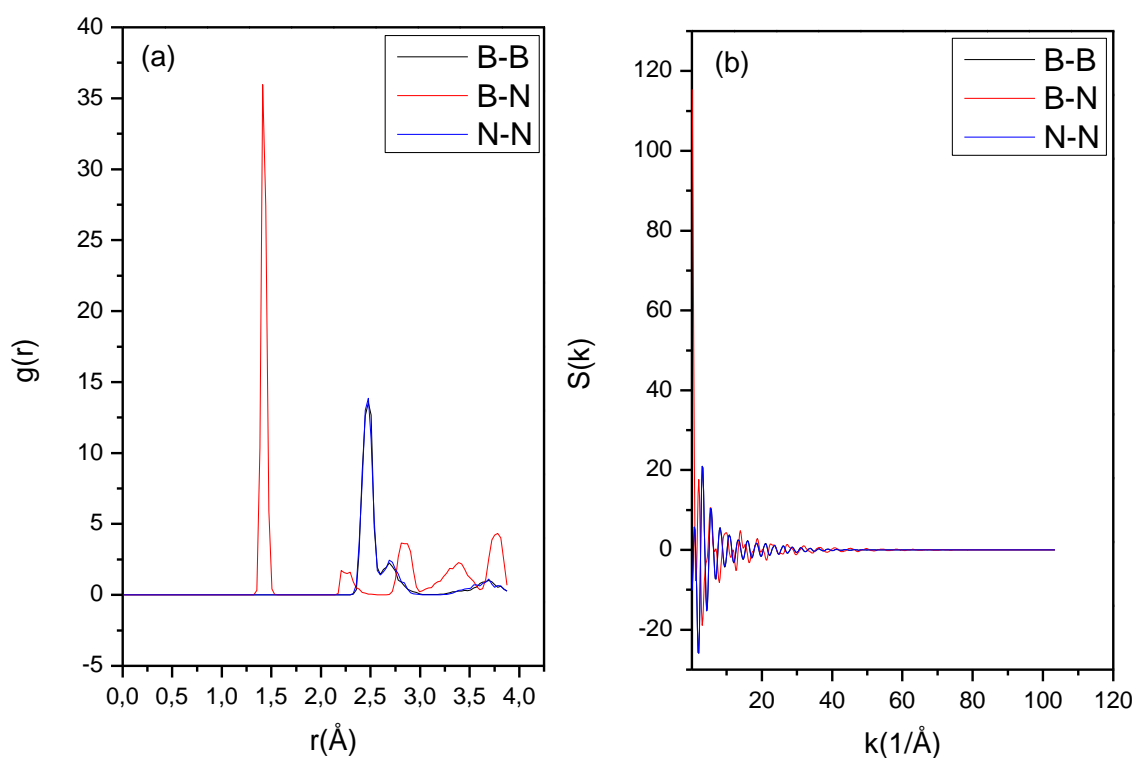
Figure 4. 1: Radial Distribution Functions together with their corresponding structure factors for (a) and (b) h-BNNSs144 supercell.

Table 4. 1: First and second nearest neighbouring distances (r_1 and r_2) and number of atoms (n_1 and n_2) for h-BNNSs144 supercell at 300 K.

Supercells	Atomic bonds	r_1(Å)	n_1	r_2(Å)	n_2
h-BNNSs144	B-B	2.47	0.82	2.69	0.24
	B-N	1.41	1.64	2.81	0.27
	N-N	2.47	0.82	2.69	0.22
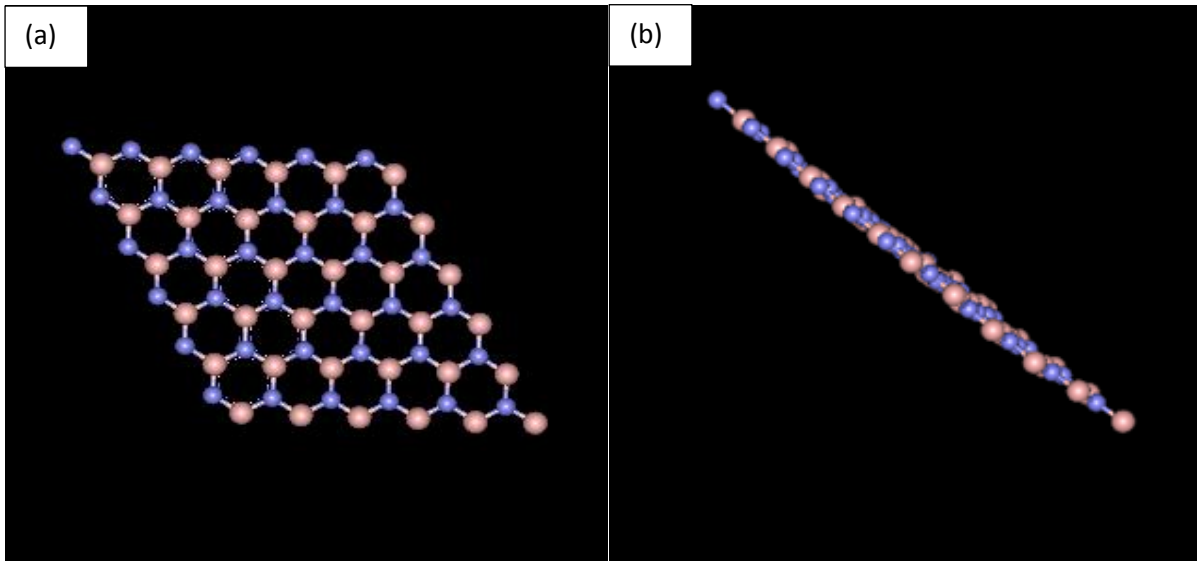
Figure 4. 2: The visualisation of the structure (a) and (b) represented by alternating B (brown balls) and N (blue balls) atoms together with its alignment perpendicular to the plane of defect free nanosheets for h-BN144 supercell at 300 K.

4.2.1.2 Determination of the lattice parameters

The equilibrium lattice parameters of h-BNNSs calculated for all the supercells are in good agreement with the previously obtained results on the material [295, 296, 297]. The Tersoff potential used in the present study reliably gives the lattice parameters of all the three supercells closer to the experimental values. The experimental lattice parameter of h-BN at room temperature is reported as a = 2.504 Å with an average

B-N bond length of 1.44 Å [295]. Molecular dynamics simulations using a modified Albe, Moller and Heining interatomic potential gives the equilibrium lattice parameter of a = 2.532 Å at 0 K [296, 297] with an average B-N bond length of 1.46 Å. In this work, at room temperature the lattice parameters of the supercells (144, 324 and 576 atoms) were respectively found to be a = 2.477 Å, 2.507 Å and 2.507 Å with an averaging B-N bond length of 1.41 Å, 1.44 Å and 1.44 Å.
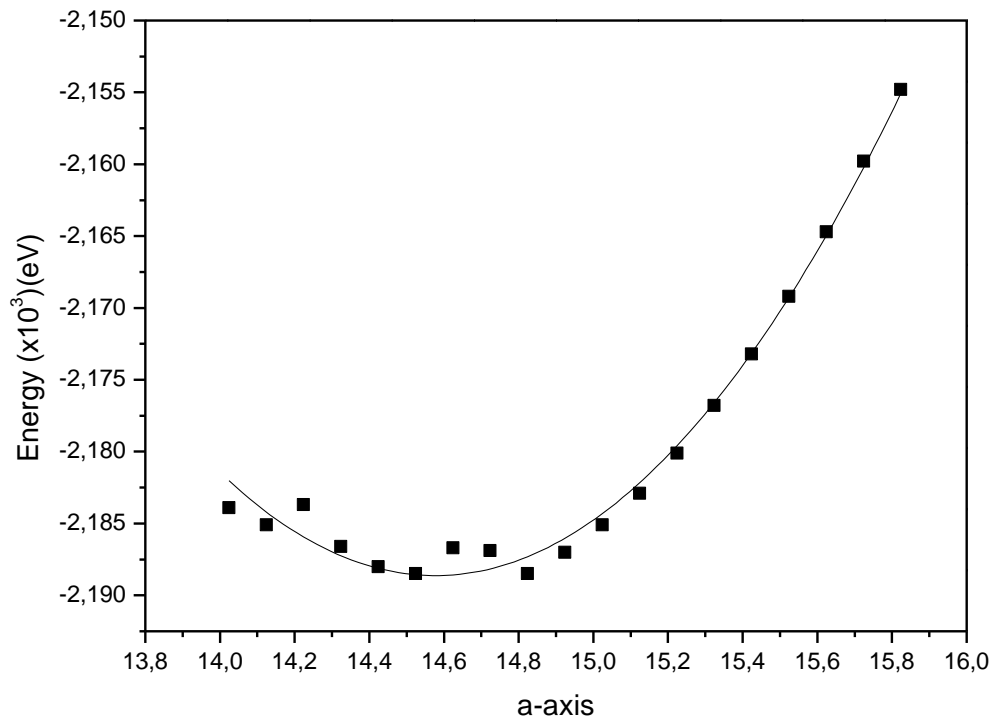
Figure 4. 3: Graphs of total energy vs a-axis of h-BNNSs144 supercell.

These results compare fairly well with experimental values as well as those of other studies reported in this section [295, 296, 297 and 393]. The lattice parameters of all the supercells were determined at minimum temperature, together with their

corresponding energy. Table 4.2 shows the lattice parameters that were found to be increasing with an increase in the surface area, and their corresponding energies decreased as the surface area increased. The relationship between energy and the lattice parameter, which is of inverse proportionality nature, is respected and complemented by the calculated results.

Table 4. 2: Supercell and unit cell lattice parameters at minimum together with the corresponding minimum energy for all the supercells.

Supercells	h-BNNSs144	h-BNNSs324	h-BNNSs576
Supercell lattice parameter (a_0) (Å)	14.563	22.568	29.897
Unit cell lattice parameter (a_0) (Å)	a = b = 2.477	a = b = 2.507	a = b = 2.507
Literature unit cell lattice parameter (a_0) (Å) [393]	a = b = 2.504		
Total Energy (E_T) (eV)	-2.1886×10^3	-4.9155×10^3	-8.7414×10^3

4.2.1.3 Diffusion constants on the h-BN nanosheets

To explain the mobility of B and N atoms in the h-BN nanosheet, the mean square displacement (MSD) graphs are plotted in Figure 4.3 for h-BN144 (see Appendix 1: Figure 1-3 for h-BN324 and h-BN576 supercells MSD) and are utilised to calculate the diffusion coefficients or constants of both B and N atoms. The diffusion coefficients are calculated as the surface area of the sheets increases. The mobility

of the atoms within the surface of the material was studied to extract the bending rigidity of h-BN nanosheets and, it was noticed that the formation of the ripples strongly rely on the atomic corrugations, which can be outlined through diffusion coefficient. In relation to the sp^2 C-C bonds in graphene, the B-N bonds in h-BN are not perfectly covalent in nature and that is because there is an ionic character in B-N bonds, due the electronegativity difference between the two atoms.
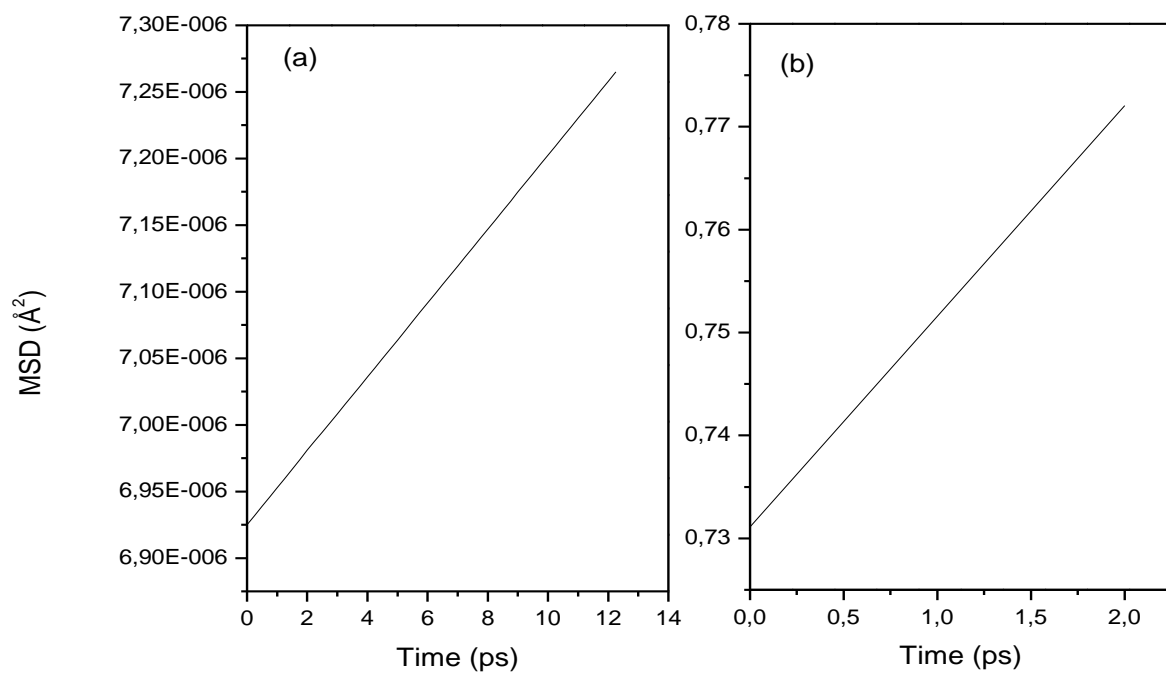
Figure 4. 4: Mean Square Displacement graphs of (a) B for h-BNNSs144, (b) N for h-BNNSs144 supercells.

Table 4. 3: Diffusion coefficients for both boron (B) and nitrogen (N) atoms for all the supercells.

Supercells	Diffusion coefficient of B ($Å^2$/ps)	Diffusion coefficient of N ($Å^2$/ps)
h-BNNSs144	2.86×10^{-8}	2.05×10^{-2}
h-BNNSs324	6.68×10^{-3}	4.31×10^{-3}
h-BNNSs576	2.02×10^{-1}	2.02×10^{-1}

The results depicted in Table 4.3 shows the diffusion coefficients of B and N atoms respectively for h-BNNSs144, h-BNNSs324 and h-BNNSs576 supercells at 300 K. The diffusion coefficient of B atom within the nanosheets increases with an increase in the surface area of the nanosheets, while that of N monotonically increases with an increase in the surface area of the nanosheets. That results in the larger charge density along the plane due to valence electrons in the B-N bonds. A careful analysis of the MSD of both B and N atoms in the h-BN nanosheet, shows the MSD fluctuations of B atom in relation to an increase in the surface area, while that for N atom decreases monotonically with an increase in the surface area of the nanosheets. These demonstrates that, the absence of the inter-layer interactions in mono-layer h-BN, which leads to an increase in the hardness of the nanosheets that is enhanced by the ionic nature of B-N bonds, has a negative impact in the hardness of mono-layer h-BN relative to the bulk h-BN. The stiffness of the nanosheets is reduced as the surface area of the nanosheets increases, which is in good agreement with what was reported by *Alem et al.* [297].

4.2.2 Thermal properties of h-BNNSs

In this sub-section, modelled effects of temperature on the mechanical properties of 2D h-BNNSs/white graphene are discussed. It is a known fact that temperature plays an important role on the mechanical properties of nanomaterials [298, 299]. The variation of temperature from 300 to 1000 K for NVT ensemble and from 300 to 1200 K for NPT hoover ensemble as the surface area increases was performed to investigate the thermo-stability of the nanosheets. In the process, the entropy and coefficient of linear thermal expansion were calculated. The calculations for all the supercells were performed in the NVT Evans and NPT hoover ensembles at standard pressure (0.0 atm). To achieve the objectives, the total energy of each supercell was plotted with respect to the changing temperature as displayed in Figure 4.5. To quantify the behaviour of h-BNNSs energy against temperature, Figure 4.6 presents the visuals effects of these nanosheets at 1000 K (see Appendix 3: Table 3-1 for full visualisation together with the alignments for NVT ensemble).

The structural stability of 2D h-BNNSs/white graphene can also be demonstrated from the strain and stress point of view. It is known that there are only two energy components that contribute to the total energy for material to break under tensile loading, which are thermal and strain energy [300]. It has already been shown that the thermal energy of the materials for all the supercells increases linearly with temperature which implies that, the strain energy required for a material to break is reduced, due to the inverse proportionality relationship between strain and thermal energy. As such, the stress will also reduce because of direct proportionality relationship between stress and strain. Therefore, the materials experience less strain and stress as the temperature gets intensified.

66
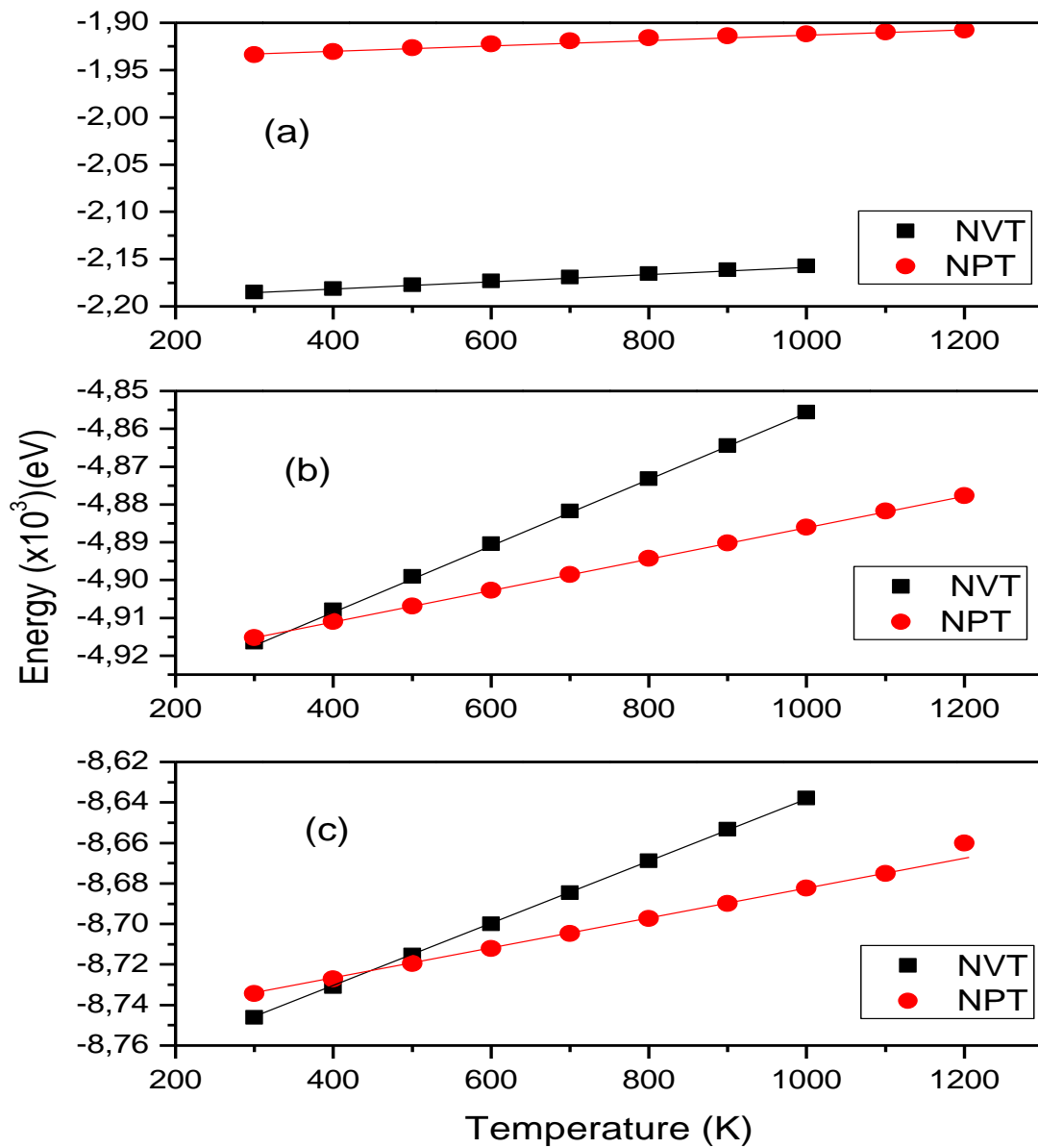
Figure 4. 5: Graphs of total energy vs temperature for NVT and NPT ensembles of (a) h-BNNSs144 (b) h-BNNSs324 and (c) h-BNNSs576 supercells.
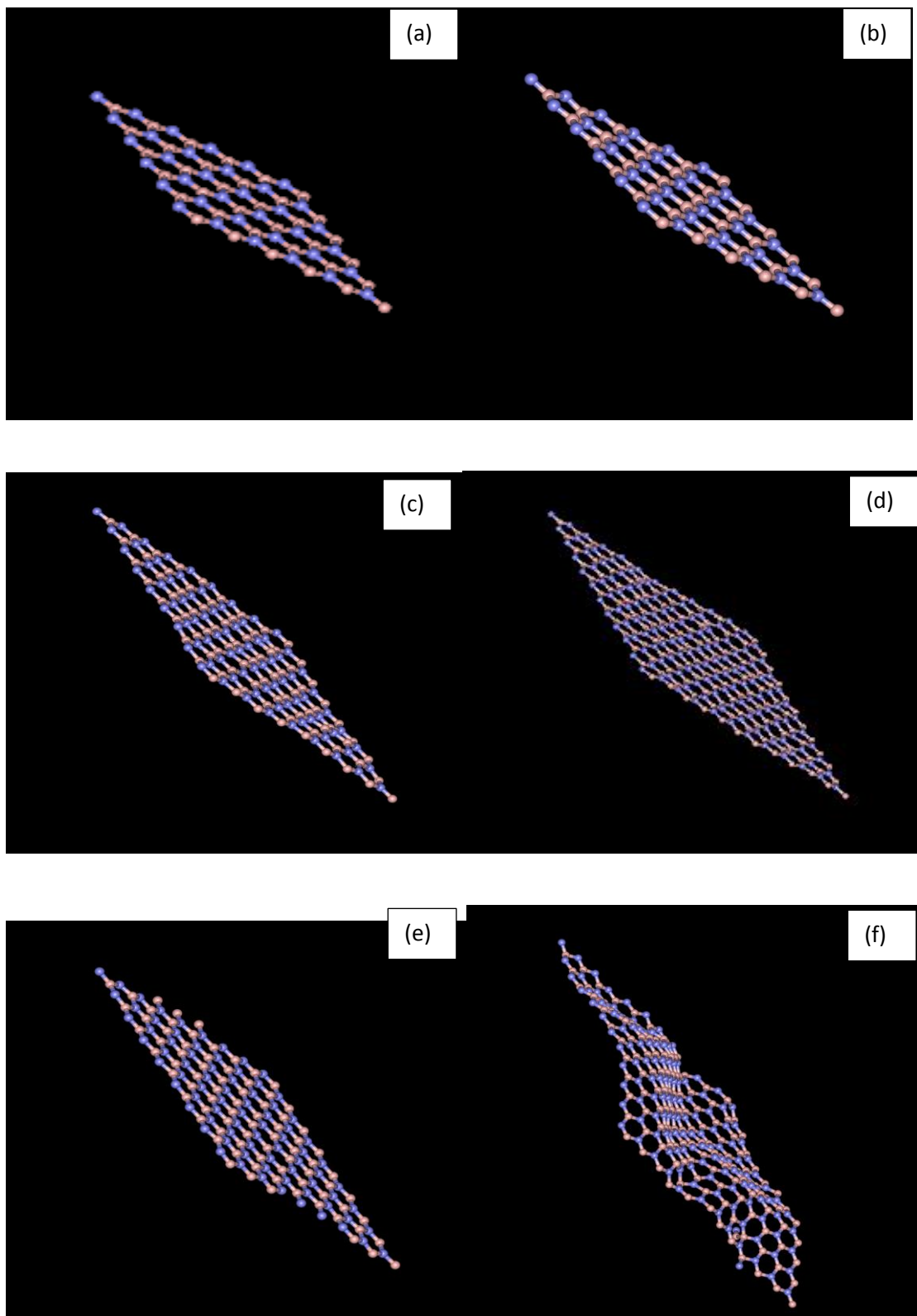
Figure 4. 6: The visualisation of defect free supercells structures represented by alternating B (brown balls) and N (blue balls) atoms for (a) h-BN144 NVT, (b) h-

BN144 NPT, (c) h-BN324 NVT, (d) h-BN324 NPT, (e) h-BN576 NVT and (f) h-BN576 NPT ensembles at 1000 K.
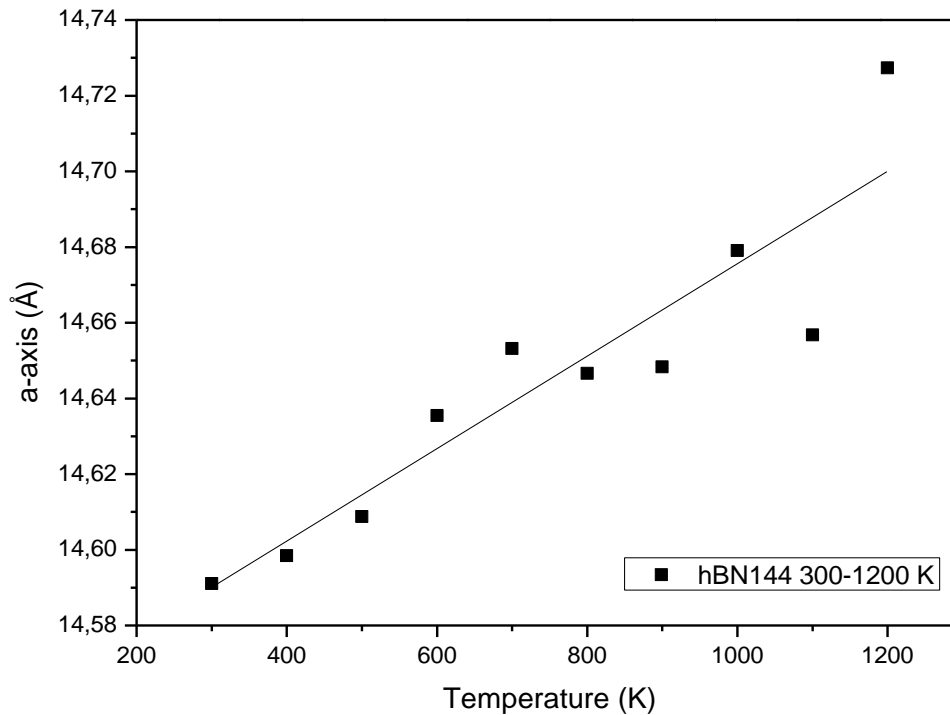
Figure 4. 7: Graph of a-axis vs temperature for hBN144 from 300 – 1200 K temperature range for determining the coefficient of thermal expansion under NPT hoover ensemble.

The entropy was then calculated for all the three supercells, as it is known in physics that, the unfound information about the state of a system can be related to the entropy of the system. In statistical mechanics, entropy is one of the most popular quantities, which displays the measure of the disorder of a system [301, 302], which is also known to be a measure of the number of possible arrangements atoms can have in a system. The entropy in the supercells considered increases with an

increase in the surface area of the materials, which actively demonstrates that, the number of possible arrangements of the atoms within the surface increases.

Table 4. 4: Calculated entropy and coefficient of linear thermal expansion with an increase in the surface area for all the supercells.

Supercells	Entropy (eV/K)	Thermal expansion (K⁻¹)
h-BNNSs144	3.8×10^{-2}	1.50×10^{-3}
h-BNNSs324	8.6×10^{-2}	-3.50×10^{-2} and 3.50×10^{-2}
h-BNNSs576	1.56×10^{-1}	1.02×10^{-1} and 1.45×10^{-2}

This also contributes to the stability of the material to be uniform as the surface area of the material increases. In nanotechnology, materials that have both positive and negative thermal expansion coefficient are of practical importance as they can be utilised to make composites with very little thermal expansion/contraction [303]. In general, if a is the equilibrium lattice parameter and T is the corresponding temperature, then the linear thermal expansion coefficient $(a_l (T))$ can be calculated using equation 4.2:

$$a_l(T) = \frac{1}{a(T)} \left(\frac{\partial a(T)}{\partial T} \right)_p \qquad 4.2$$

Thomas et al. [10], have disclosed that h-BN has a negative thermal expansion at low temperatures as a result of the presence of low frequency bending modes in its phonon spectrum. *Sevik et al.* [304], also reported negative thermal expansion of h-BN below 300 K using a quasi-harmonic approximation (QHA) which gradually

increases in the temperature range of 300 – 1500 K. In the present study, the linear thermal expansion of 2D h-BNNSs/white graphene for the supercells was examined through classical molecular dynamics. This was achieved by simulating the material at different temperatures ranging from 300 to 1200 K as depicted in Figure 4.7 for hBN144 (see Appendix 2: Figure 1-4 for hBN324 and hBN576 graphs). The results acquired using the NPT hoover ensemble shows that 2D h-BNNSs/white graphene possesses a positive a_l of $1.50 \times 10^{-3}\,K^{-1}$ for hBN144 within the specified temperature range. The hBN324 supercell possesses a negative a_l of $-3.50 \times 10^{-2}\,K^{-1}$ within a temperature range of 300 – 500 K and a positive a_l of $3.50 \times 10^{-2}\,K^{-1}$ within a temperature range of 600 – 1000 K. In the case of h-BN576, two positive thermal expansion coefficients were observed; a_l of $1.02 \times 10^{-1}\,K^{-1}$ in the temperature range of 300 – 500 K and a_l of $1.45 \times 10^{-2}\,K^{-1}$ in the temperature range of 800 – 1200 K (see Table 4.4 for full results). Our study shows both positive and negative linear thermal expansion coefficients, which are comparable to the earlier studies, reported by *Thomas et al.* [10] for negative and *Sevik et al.* [304] within a range of 300 – 1500 K for positive thermal expansions. As the temperature further increases, the vibrational frequency of the atoms around a single atom will also increase, causing the increase in the inter-atomic distance. Thus, a non-monotonic variation of the lattice constant with temperature is observed at 1200 K as shown in Figure 4.5: (c) h-BN576 supercell NPT hoover ensemble.

4.2.3 Native defects of h-BNNSs

The computational analysis of defects for the calculations of mechanical properties promotes the understanding of the materials behaviour at various physical situations [303]. The effect of the defects in a 2D mono-layer system may be far more evident

when compared with the bulk counterparts. This is because all atoms in a mono-layer nanosheet are in the surface on both sides of the plane. Therefore, the defects can change the properties of the material dramatically, due to the perturbation of the surface atomic arrangements [80]. Vacancies are the usual defects in a 2D h-BN layer that needs special attention. The focus here is on the mono-vacancy defects, which are created by the removal of either B or N atom in h-BNNSs. The vacancies are randomly created in the h-BN nanosheet, where the variation of total energy with temperature generally demonstrate the structural changes. Classical molecular dynamics is a good suitable computational simulations model used to search for possible distortions of the lattice [338]. In all the three supercells, the B and N atom vacancies were introduced with the varying temperature of 300 – 1200 K in the NVT Evans ensemble. The energy versus temperature of the entire setting is displayed in Figure 4.7. The interatomic potential model used in the present molecular dynamics simulations has no one-body term. Hence, the total energy that is being calculated represents the change in energy of a collection of atoms when they are brought together.
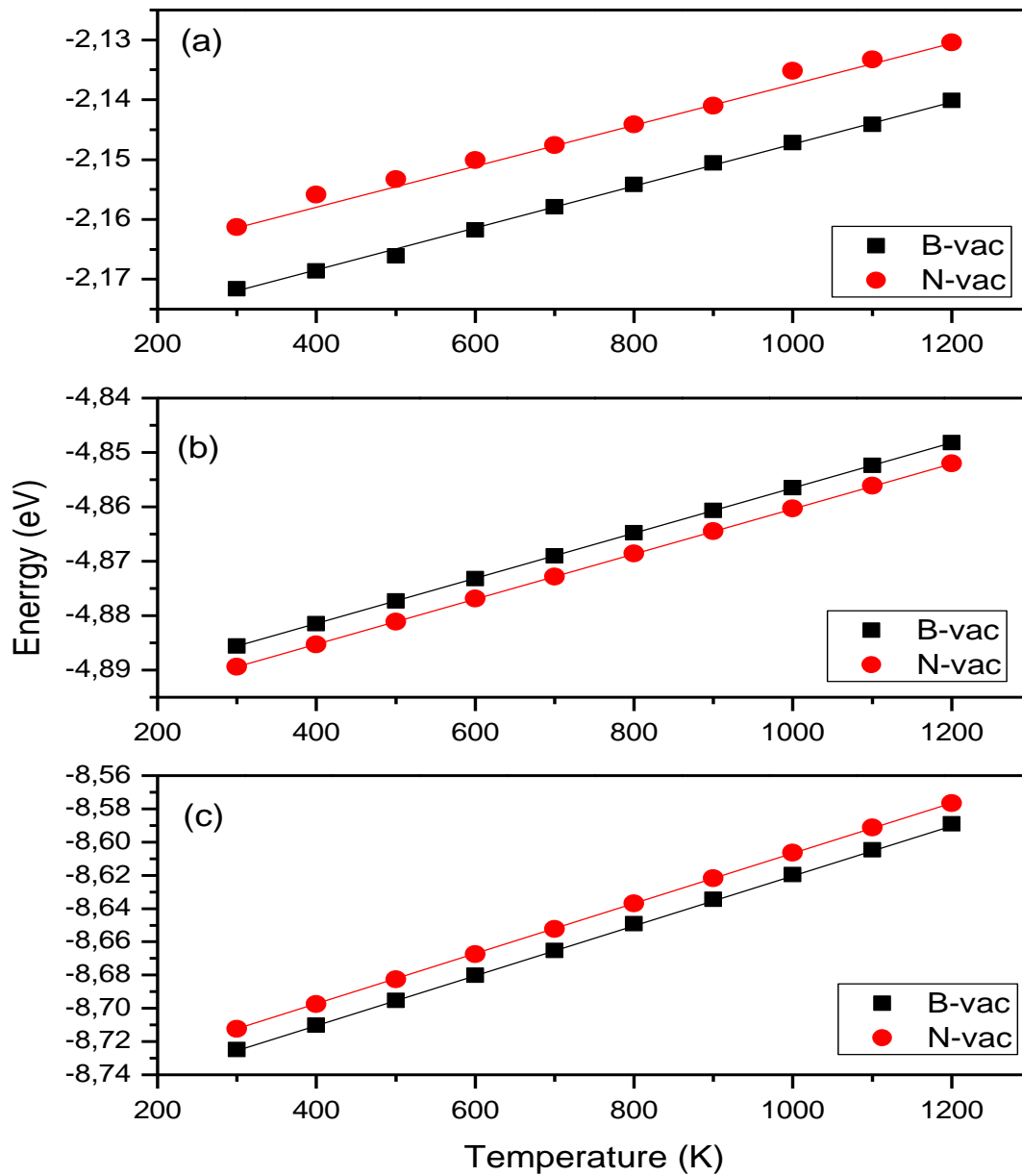
Figure 4. 8: Graphs of energy as a function of temperature of V_B and V_N for (a) h-BNNSs143 (b) h-BNNSs323 and (c) h-BNNSs575 NVT Evans ensemble.

Table 4. 5: Shows the total energy of a defected BN system, vacancy energy for the formation of a vacancy, volume and entropy of a system of V_B, V_N and defect free for h-BNNSs143 supercell.

Supercells		B-vacancy	N-vacancy	Defect free
h-BNNSs143	Total energy (eV)	-2.1716×10^3	-2.1613×10^3	-2.1886×10^3
	Vacancy energy (eV)	-17	-27.3	$-$
	Volume (Å^3)	1.4969×10^3	1.4969×10^3	1.4969×10^3
	Entropy (eV. K^{-1})	3.8×10^{-2}	3.0×10^{-2}	3.8×10^{-2}

In the present setup, the boron atom vacancy is represented by V_B and the nitrogen atom vacancy is represented by V_N. The V_B and V_N defects on h-BNNSs are constantly compared with the defect free h-BN nanosheet. The energy-temperature graphs of both V_B and V_N for all the supercells in Figure 4.7, clearly shows the linearity and the proportionality relationship between energy and temperature. From these linear plots of the defected nanosheets, we can calculate the vacancy energy as in equation 4.3:

$$E_{vac} = E_{defect\ free} - E_{defected} \qquad\qquad 4.3$$

where $E_{defect\text{-}free}$ and $E_{defected}$ represents the total energies of the defect free and defected nanosheets for all the supercells. Furthermore, if $E_{defect\text{-}free}$ is the total energy of a system with N atoms, then the cohesive energy per particle can be expressed according to equation 4.4:

$$E_{coh} \; = \; \frac{E_{defect\,free}}{N} \qquad\qquad 4.4$$

where the cohesive energy of defect free supercells was calculated to be E_{coh}= -15.2

eV/atom for all the three-defect free h-BNNSs supercells respectively. Furthermore,

the evaluation of vacancy energies of the defected nanosheets, is simply the

difference between the defect free and that of defected nanosheet. According to the

present study the V_B and V_N for h-BNNSs143, h-BNNSs323 and h-BNNSs575 per

defect are presented in Table 4.6. The tremendous difference on the values in

relation to those in literature [265] might be due to various methodological

procedures used in the modelling of the defects.

Table 4. 6: Calculated V_B and V_N defects energies for h-BNNSs143, h-BNNSs323
and h-BNNSs575 per defect.

	V_B (eV)	V_N (eV)
h-BNNSs143	-17.0	-27.3
h-BNNSs323	-14.0	-28.0
h-BNNSs575	-16.5	-29.0
Literature [265]	11.7	11.7

It was noticed that V_B and V_N have different E_{vac} in all the supercells, which clearly

describes their state of stability as shown in Table 4.5 for h-BN144 (see appendix 2:

Table 2-2 for the calculations of h-BN324 and h-BN576 supercells). Moreover, the

calculations show that the V_N has the lowest E_{vac} value as compared to V_B, which

describes V_N as more stable than V_B, suggesting it to occur easily compared to V_B type of defect.

4.2.4 Structural integrity analysis of defected h-BNNSs

In the earlier sections, we have outlined the structural behaviour of pristine mono-layer h-BN by temperature variation of the system from 300 to 1000 K to analyse its mechanical properties. Table 4.7 shows the peak positions of first and second neighbour distances of V_B and V_N at 300 K for h-BNNSs143. For V_B, the first and second nearest neighbour distances appear at 2.47 and 2.63 Å respectively. In the same manner, B-N first and second nearest neighbouring distances appear at 1.43 and 2.22 Å, while the N-N first and second nearest neighbouring distances appear at 2.45 and 2.68 Å. Looking at the nitrogen vacancy, V_N, B-B interactions has 2.47 and 2.70 Å, first and second nearest neighbour distances respectively. On the B-N interactions, the first and second nearest neighbour distances appear at 1.43 and 2.27 Å respectively, while the N-N arrangement has 2.47 and 2.68 Å first and second nearest neighbour distances. Such a display is projected in Figure 4.8 for the h-BNNSs143. These results were found to compare and concur well with the defect free counterpart.
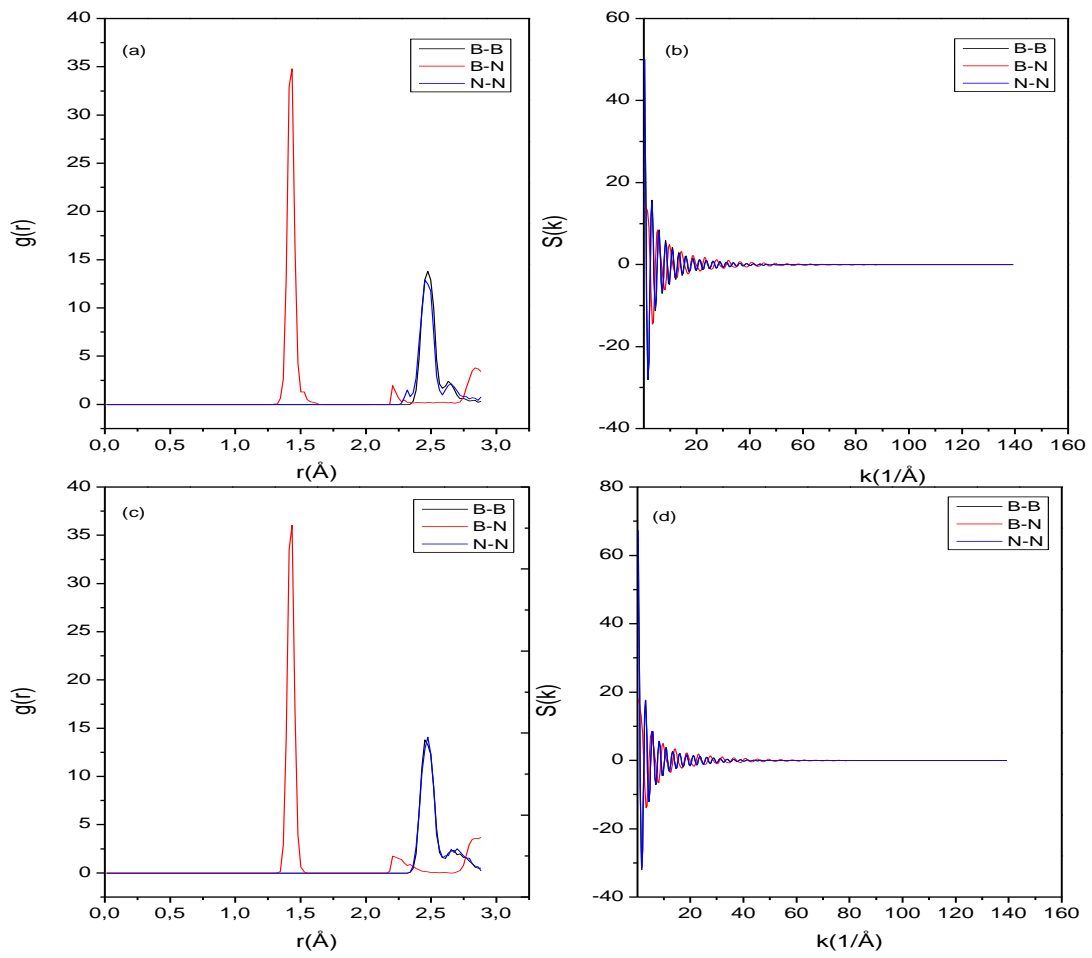
Figure 4. 9: Radial Distribution Functions together with their corresponding structure factors of (a) and (b) V_B for h-BNNSs143 supercell and (c) and (d) V_N for h-BNNSs143 supercells.

Table 4. 7: First and second nearest neighbouring distances (r_1 and r_2) and number of atoms (n_1 and n_2) of V_B and V_N for h-BNNSs143 supercell.

Defect description	Atomic bonds	r_1(Å)	n_1	r_2(Å)	n_2
	B-B	2.47	1.10	2.63	0.23
V_B	B-N	1.43	2.26	2.22	0.14
	N-N	2.45	1.61	2.68	0.16
	B-B	2.47	1.76	2.70	0.23
V_N	B-N	1.43	2.53	2.27	0.11
	N-N	2.47	1.76	2.68	0.14
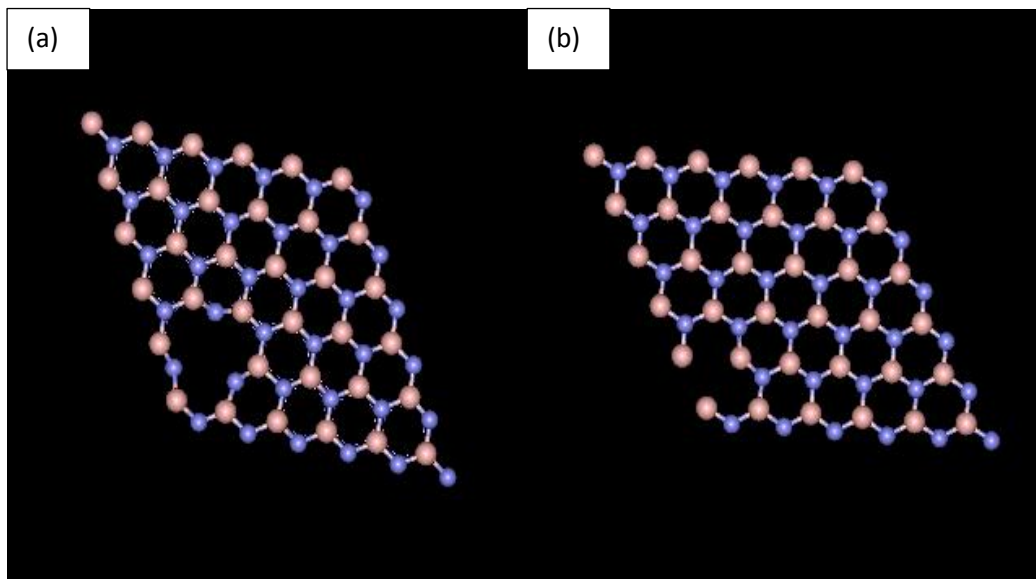
Figure 4. 10: The visualisation of V_B and V_N represented by alternating B (brown balls) and N (blue balls) atoms respectively. (a) V_B for 143 atoms, (b) V_N for 143 atoms supercells.

4.3 Conclusion

The structural behaviour of defect free and defected mono-layer 2D h-BNNSs atomic supercells have been studied with help of Tersoff potentials at different temperatures. The calculated $(g_{AB}(r))$ and $S(k)$ results demonstrated the consistency of Tersoff potentials in explaining the interaction between B and N atoms within the BN system, together with how B-B, B-N, and N-N bonds arrange and distribute themselves around a given atom. The calculated diffusion coefficients for both B and N atoms, which were found to be increasing with an increase in the surface area, demonstrated the motion of atoms on the surface of the materials. Whilst the entropy which was as well found to be increasing with surface area outlined the arrangements of atoms within the surface of the nanosheets with an increase in the surface area. The coefficients of thermal expansion through the h-BNNSs demonstrate complex behaviour as the supercell surface area increases. At larger surface areas, more coefficients of thermal expansion, which include both positive and negative values, are experienced. This idea is associated with the nanosheets bending and wrinkles as suggested by the experiments. V_N point defect was found to be more stable and to occur easily than the V_B point defect due to its less E_{vac}. Lastly, the results of defect free and defected nanosheets were found to compare and concur well with each other.

Chapter 5

Experimental studies on h-BN nanosheets

5.1 Introduction

The synthesis of BN was first initiated in 1842 by the reaction between boric acid and potassium cyanide as the B and N precursors [160], as h-BN cannot occur spontaneously. The structure and properties of h-BN depends on the synthesis method. Various techniques and synthetic conditions have been applied, to experimentally synthesise h-BN from a variety of B and N precursors [306, 307]. In this section, the analysis of the as-synthesised h-BN through CVD approach is reported at three various temperatures of 800, 900 and 1000 °C with the aim of identifying the effects of temperature on the synthesis of the nanosheets.

5.2 Results and Discussion

5.2.1 XRD analysis

The X-Ray Powder Diffraction (XRD) is typically known to be the most common method used to analyse the phase purity and structural properties of the layered materials [308]. Figure 5.1 displays the regular XRD pattern of h-BNNSs for h-BN800°C, h-BN900°C and h-BN1000°C. The pattern attest to the fact that h-BN powders crystallise into a pattern of nanosheets which describe 2D hexagonal honeycomb. The pattern is presented by the most intense known peaks at 2θ = 26.02°, 25.97°, 26.06° with an interlayer d-spacing (d_{002}) of 0.342 (h-BN800°C), 0.343 (h-BN900°C) and 0.342 (h-BN1000°C) nm (estimated according to Bragg's law) corresponding to (002) diffraction plane of the hexagonal phase of BN crystal. The classical MD simulation results displayed in Figure 4.2 and Table 4.3 in sub-

section 4.2.1 confirm the dimensions of the h-BN nanosheets measured through this XRD. The second peaks appear at 2θ = 45.03°, 44.68°, 44.63°, corresponding to (101) diffraction plane of the hexagonal BN crystal phase with no impurities detected. Such findings suggest a polycrystalline structure in nature.
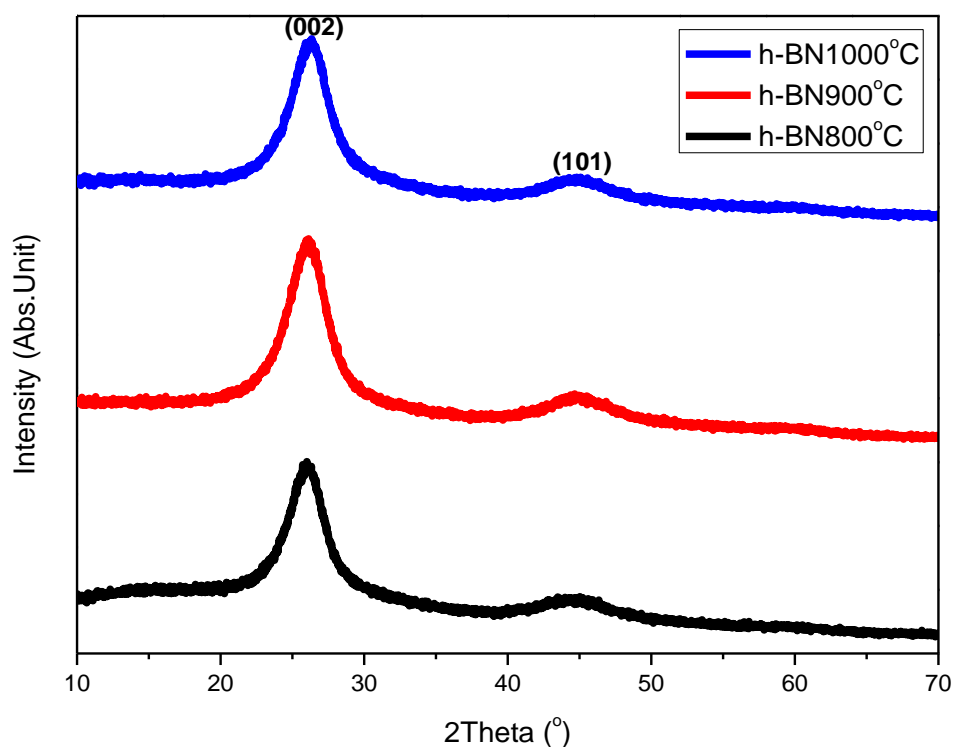
Figure 5. 1: X-ray diffraction pattern of 2D h-BNNSs at three different

The nanosheets were found to display the corresponding lattice parameters of $a = b$ = 2.515 Å and c = 6.700 Å belonging to the space group of P63mc (180) for all the samples of h-BN800°C, h-BN900°C and h-BN1000°C, and all these parameters were found to be in good agreement with theoretically reported values [270-273]. The amorphous phase of BN crystal is formed when heating boric acid and urea at 600 °C, however, further increase of the reaction temperature leads to the formation of h-BN [270]. Ammonium polyborate is formed as well, as a result of heating the

mixture in a temperature range of 250 – 300 °C, while another part of urea reacts with water to form ammonia.

Table 5. 1: XRD extracted lattice parameters and calculated d-spacing and crystalline sizes for h-BN800°C, h-BN900°C and h-BN1000°C respectively.

Sample names	Lattice parameters (Å)	d-spacing (Å)	Crystalline sizes (Å)
h-BN800°C	a = b =2.515 c = 6.700	3.420	46.00
h-BN900°C	a = b =2.515 c = 6.700	3.430	46.00
h-BN1000°C	a = b =2.515 c = 6.700	3.420	46.00

Lastly, ammonium polyborates react with ammonia to form a-BN [270] by heating in a temperature range of 500 – 600 °C in accordance to the equations:

$$4^.H_3BO_3 + CO^.(NH_2)_2 \rightarrow (NH_4)_2B_4O_7 + CO + 4H_2O \qquad 5.1$$

$$CO^.(NH_2)_2 + H_2O \rightarrow 2NH_3 + CO_2 \qquad 5.2$$

$$(NH_4)_2B_4O_7 + NH_3 \rightarrow 4\ a\text{-}BN + 7H_2O \qquad 5.3$$
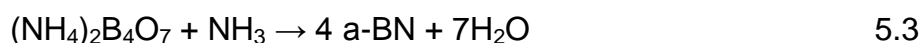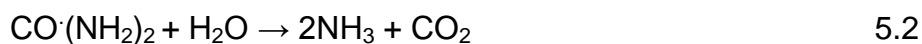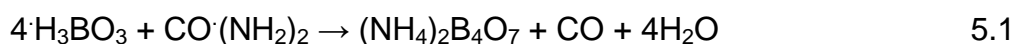
A similar methodological procedure is followed in the current study. However, in this study the mixtures were heated for 3 hours at three different temperatures (800, 900

and 1000 °C) under N_2 gas atmosphere. In that way, h-BN is fabricated under high vacuum system to avoid the chances of impurities in the nanosheets. It has been observed that at a temperature of 800 °C/ 3 hours under N_2 atmosphere, the material experiences some phase changes from amorphous phase. The graph at this temperature shows a BN crystal which is not fully crystallised as observed in the XRD pattern of h-BN800°C in Figure 5.1. As such, the temperature was further increased to 900 and 1000 °C for 3 hours to enhance the crystallinity of the nanosheets. The hexagonal phase of BN nanosheets were fully synthesised with high crystallinity at a minimum temperature of 900 °C and a maximum temperature of 1000 °C as displayed in the XRD pattern of h-BN900°C and h-BN1000°C in Figure 5.1. On comparison, the thickness of (002) peak phase has been mostly used for the investigation of single or fewer layered graphene [309]. Therefore, the crystal size of the h-BNNSs for all the three samples was determined by Debye-Scherrer equation:

$$D = \frac{K\lambda}{\beta cos\theta}$$
 5.1

where D is the crystallise size, K is the constant ($K = 0.9$), $λ$ is the wavelength of the X-ray, $β$ is the full width at half maximum (FWHM) in radians and $θ$ is the Bragg's angle in radians. The broadness of the diffraction peak suggests the nanoscale crystal size of h-BNNS for (h-BN800°C, h-BN900°C and h-BN1000°C) to be 4.6 nm (46 Å) which is consistent with the previously reported values [270]. The consistency in the crystalline size, it is what has been expected, since it is a known fact that, the larger or the increase in the crystalline size will affect the surface area of the materials, which will in-turn lower the gas sensing properties of the nanosheets.

5.2.2 FTIR analysis

The Fourier Transform Infrared Spectroscopy (FTIR), shown in Figure 5.2 was employed to survey the types of chemical bonds formed by the obtained h-BN800°C, h-BN900°C and h-BN1000°C samples. In the spectra, there are two strong peaks observed in relation to the chemical bonding of the h-BNNSs. The first peaks appear at 748, 764 and 764 cm^{-1} for h-BN800°C, h-BN900°C and h-BN1000°C samples respectively, attributed to the B-N out-of-plane bending vibrations. The second peaks which appear at 1360, 1366 and 1365 cm^{-1} for h-BN800°C, h-BN900°C and h-BN1000°C samples respectively, are associated with the in-plane B-N-B stretching vibrations of the sp^2 bonded BN which verifies the formation of planar h-BN. The appearance of the other peaks is observed at 3375, 3487 and 3481 cm^{-1} for h-BN800°C, h-BN900°C and h-BN1000°C samples which are assigned to the hydroxyl group (*-O-H*) vibrations emerging from the releasement of the H_2O from the h-BN formation. The other broad absorption peaks appearing at 3198, 3210 and 3179 cm^{-1} for all the three samples (h-BN800°C, h-BN900°C and h-BN1000°C) are due to the imbrication of *N-H* (nitrile) stretching vibrations and *-O-H* vibrations, and are as a result of the moisture absorbed on the surface of the sample, after the ultra-sonication process. Lastly, another peak appearing at 1665 cm^{-1} in the h-BN800°C sample was observed, which is also attributed to the stretching and bending vibrations of the *-O-H* group. All these findings are consistent with the previously reported data [270, 310].
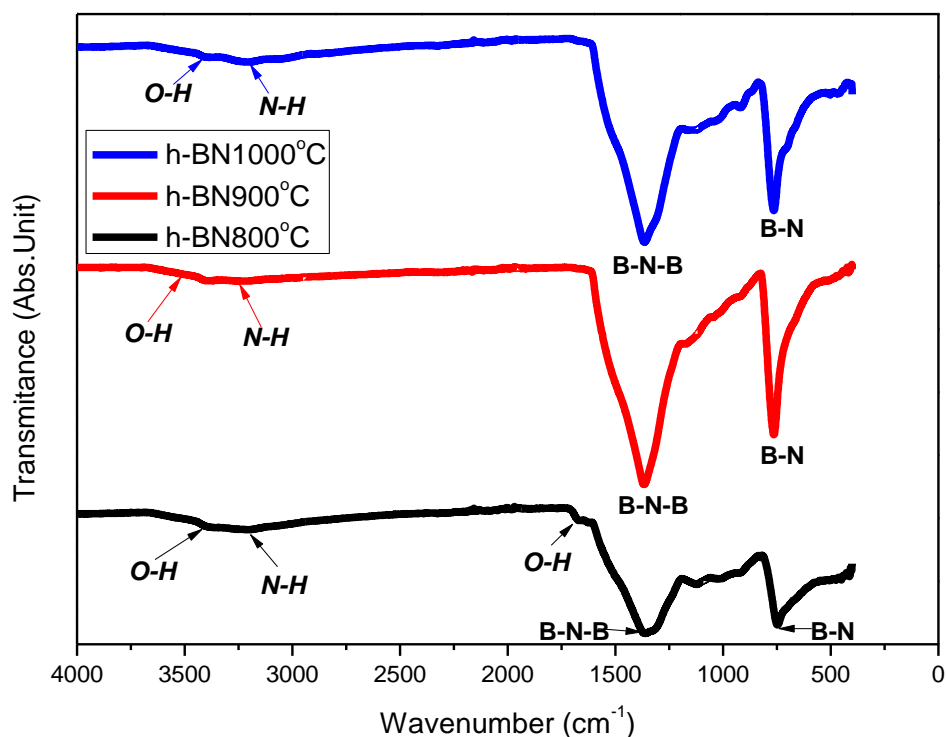
Figure 5. 2: FTIR spectroscopy of h-BNNSs at three different temperatures.

The appearance of the other small peaks of the h-BN800°C sample, at 1125 and 1021 cm^{-1} are attributed to the disordering of the amorphous phase that is still covering the entire surface of the material, as it is known that the amorphous phase of BN is the disordered h-BN. Additionally, the peaks (at lower wavenumbers) are further associated with the phase change of the material because the BN material did not completely transform from the amorphous into the hexagonal phase of BN at 800 °C and is complemented by the XRD findings. In the case of sample h-BN900°C there is only a single observed small peak appearing at 1174 cm^{-1}, which is indexed to the presence of various exterior bonds consisting of B and/or N or they might be due to the presence of the dislocations or defects [310], however with low concentration. These types of exterior bonds which involve B and/or N or dislocations or defects, are also observed with high concentrations in h-BN1000°C

samples, associated with the peaks appearing at 1163 and 919 cm^{-1}. The B and/or N exterior bonds or defects may suggest that the dislocations concentration or the presence of the defects increases with increasing temperature, which enhances the electronic properties of the nanosheets and ultimately results in the enhancement of the sensing properties of the nanosheets.

5.2.3 UV-vis spectroscopy analysis

The optical properties of h-BNNSs together with their corresponding energy band gaps were examined by means of Ultra Violet-visible (UV-vis) spectroscopy as shown in Figure 5.3. The spectroscopy was employed in all the samples as obtained in three specified temperatures. It is theoretically and experimentally known that 2D h-BN does not absorb in the visible range, however, has an absorption spectroscopy in the ultraviolet region and a great photoluminescence property with the absorption peaks ranging from 209 – 365 nm. The corresponding band gap energy ranging from 3.6 – 7.1 eV was disclosed from the experiments of h-BN with different structures [311]. The electronic state of a material can be reflected by its optical properties [311], which are regularly used to calculate the band gaps of semiconductors. The calculated direct band gap energies of 2D h-BN obtained at 800, 900 and 1000 °C, and were respectively found to be 4.79, 4.55 and 4.70 eV. The band gap energies correspond to the optical absorption shoulders of 239, 243 and 241 nm with the strong excitation peaks in the ultraviolet region, because h-BN is known to be transparent in the infrared and visible light regions. It is observed that from 900 to 1000 °C the band gap increased, this result might be due to the combination of high defects concentration together with the presence of −*OH* and *N-H* groups in the material as justified by the FTIR findings. The latest reported band gaps were

disclosed to be ~5.5 eV [312], which shows that in this study the band gap energy, has decreased with an average percentage difference of 16%.
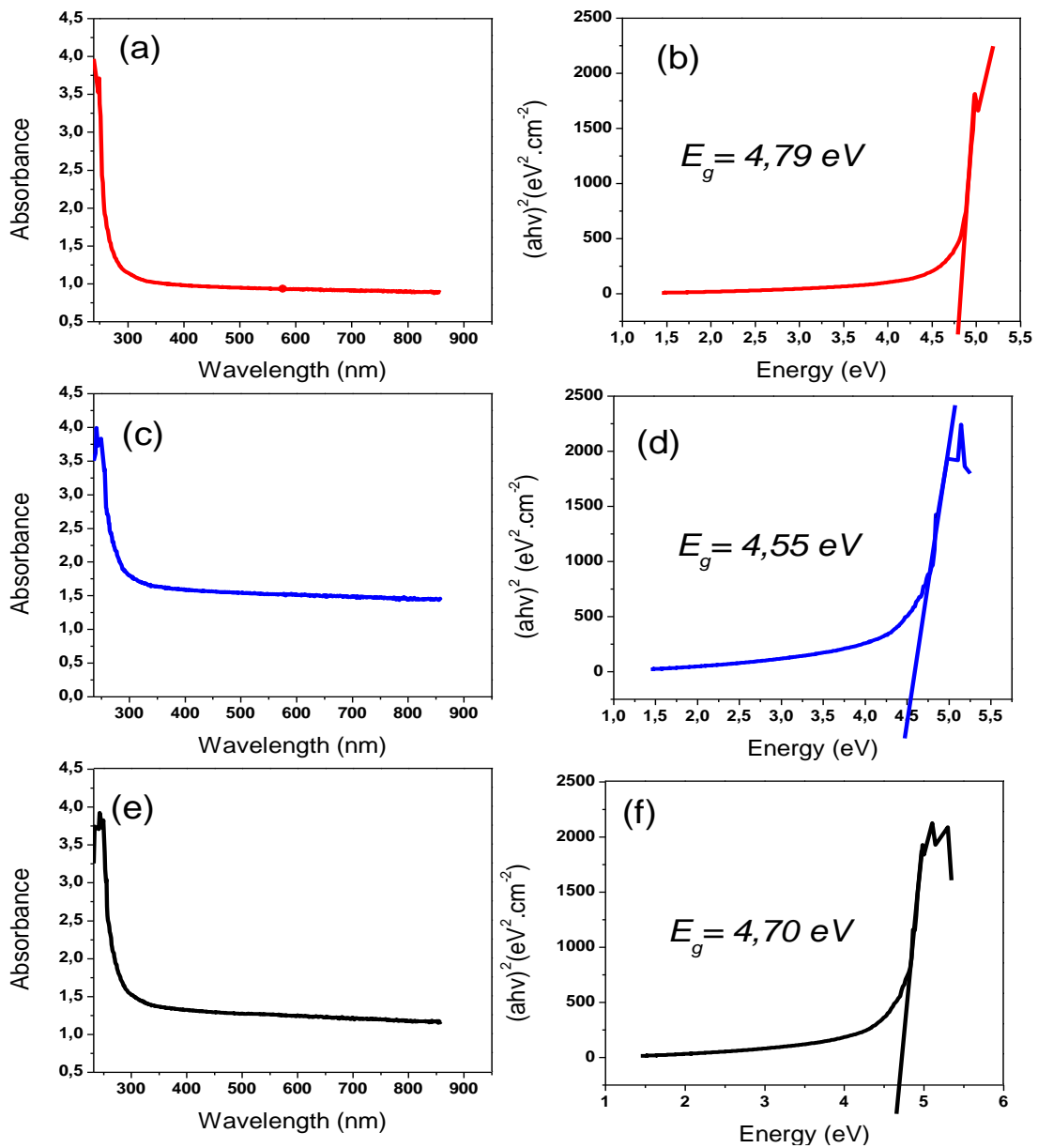
Figure 5. 3: UV-vis spectroscopy of h-BNNSs and optical band gap determination at three different temperatures of (a) and (b) 800 °C, (c) and (d) 900 °C and (e) and (f) 1000 °C.

The reduction in band gaps are due to the presence of the dislocations/defects or

the bonds containing B and/or N atoms (which some of them are related to the Stone Wales types of defects), that were found to be increasing with an increase in temperature. The rise in the dislocations were due the cooling of the system from a very high to room temperature at a high rate. Furthermore, the introduction of the defects in our studies was one of the important aspects that really needed to be taken into consideration, as they assist in the reduction of the optical band gaps [313-317], which in turn enhances the sensing properties of the nanosheets, as the major objective of the current study.

5.2.4 DLS analysis

Dynamic Light Scattering (DLS) was employed to examine the stability on surface charge of slipping planes of the nanosheets by determining the size distribution profile of the small particles, known to be affected by the presence of the polymer and the surfactant [318]. The charge is expressed by the specific value of the electro-kinetic zeta potential. Just like with other characterisation methods, the samples synthesised at three different temperatures of 800, 900 and 1000 °C were examined for noted records as illustrated in Table 5.1 and Figure 5.4.

As it is observed on the table of results, both the size distribution of a particle and zeta potential tend to factually increase with temperature. Hence, it is important to examine both the parameters that have to do with surface charge stability, as one parameter value is not a reliable indicator. The factual increase in the particle size helps to fully absorb the surfactants molecules on the particle surface, which in-turn repel each other, causing long-term dispersion, which enhances the surface stability. On the other hand, the factual increase in the electro-kinetic zeta potential was found to optimally maintain the stability of the attractive and the repulsive force of the

88

surfactants on the surface of the particles. This ability is governed by the average zeta potential falling within the range of optimum threshold limiting value of (±30 mV) for all the samples obtained at 800, 900 and 1000 °C as illustrated in Figure 5.4.

Table 5. 2: Illustrations of the size distribution of a particle and the electro-kinetic zeta potential for three different records together with their corresponding average values for samples of h-BNNSs obtained at three different temperatures of 800, 900 and 1000 °C respectively.

h-BNNSs	Size distribution (d.nm)				Zeta potential (mV)			
	Record 1	Record 2	Record 3	Average	Record 1	Record 2	Record 3	Average
800 °C	2.431e4	0.000	2.277e4	1.6e4	-32.4	-26.4	-27.4	-28.7
900 °C	4659	1.093e4	7783	7.8e3	-18.3	-9.71	-15.0	-14.3
1000 °C	5798	5485	6527	5.9e3	-26.1	-24.2	-24.8	-25.0

The colloidal dispersion of the particles is known to be theoretically governed by the Diastolic Left Ventricular Overloading (DLVO) theory, which works on the balance of the repulsive and attractive forces among the particles [319]. Therefore, both the size distribution of a particle and the electro-kinetic zeta potential, where found to be all consistent with the postulates of the theory, which in-turn enhances the stability on surface charge of the slipping planes of the nanosheets for all the samples. Furthermore, the obtained results were all verified to be in good agreement with the theoretically reported values [318].
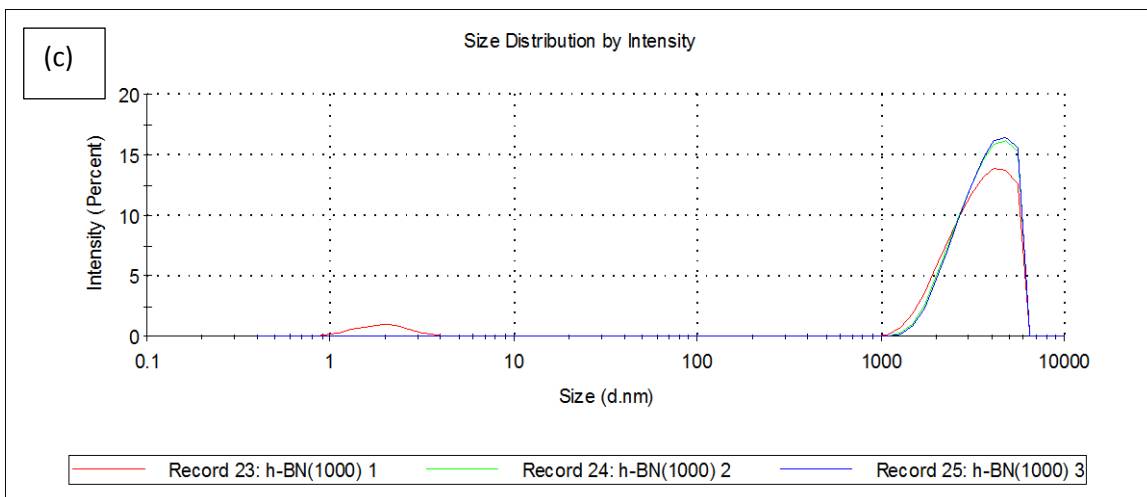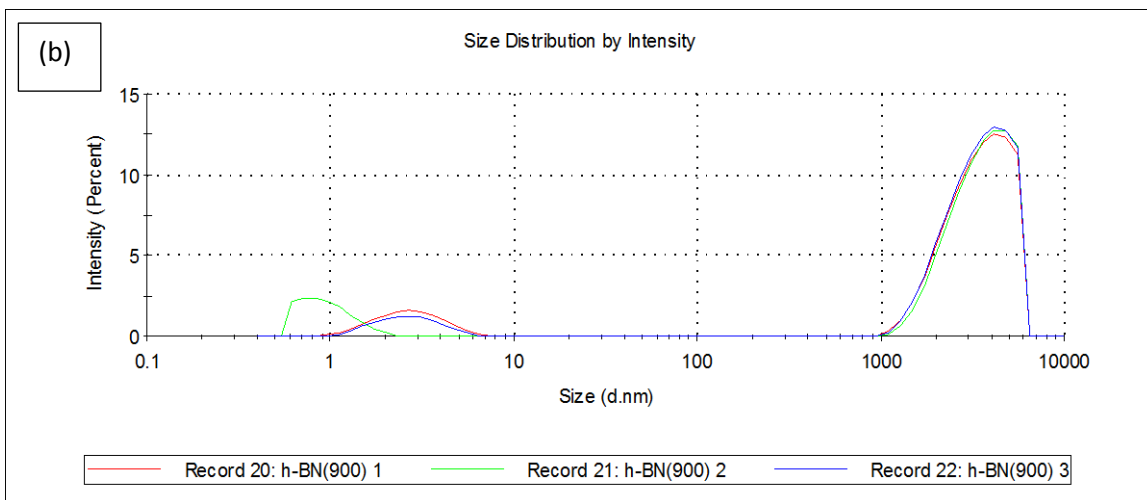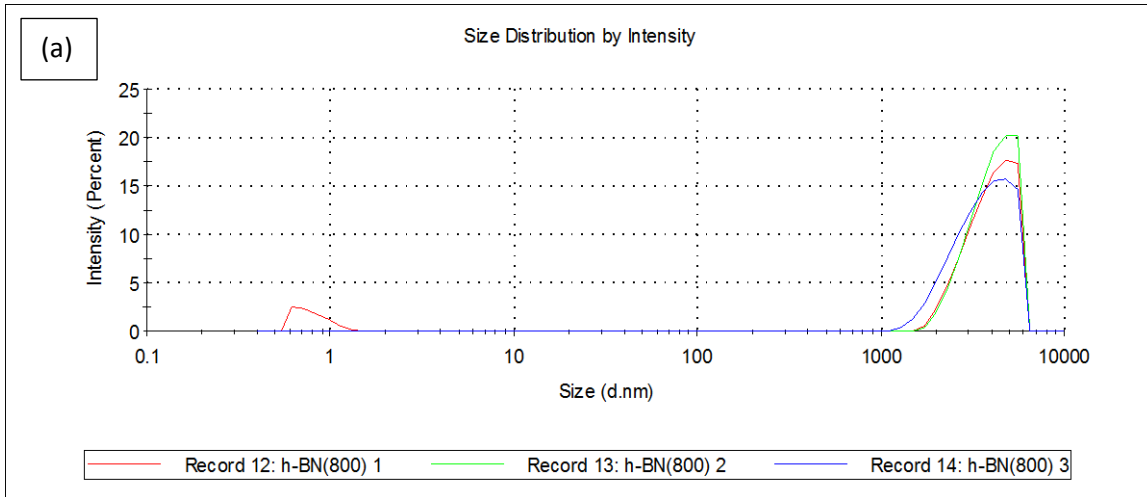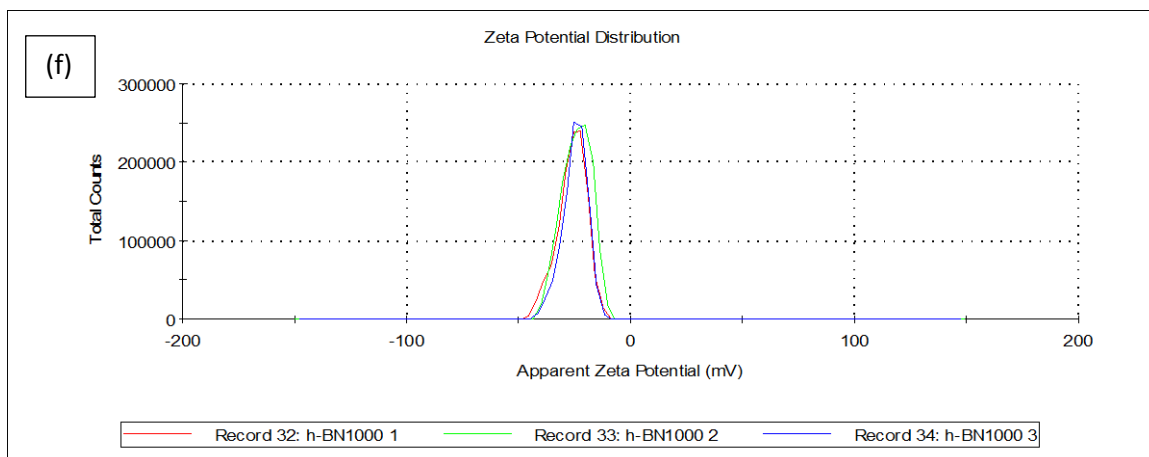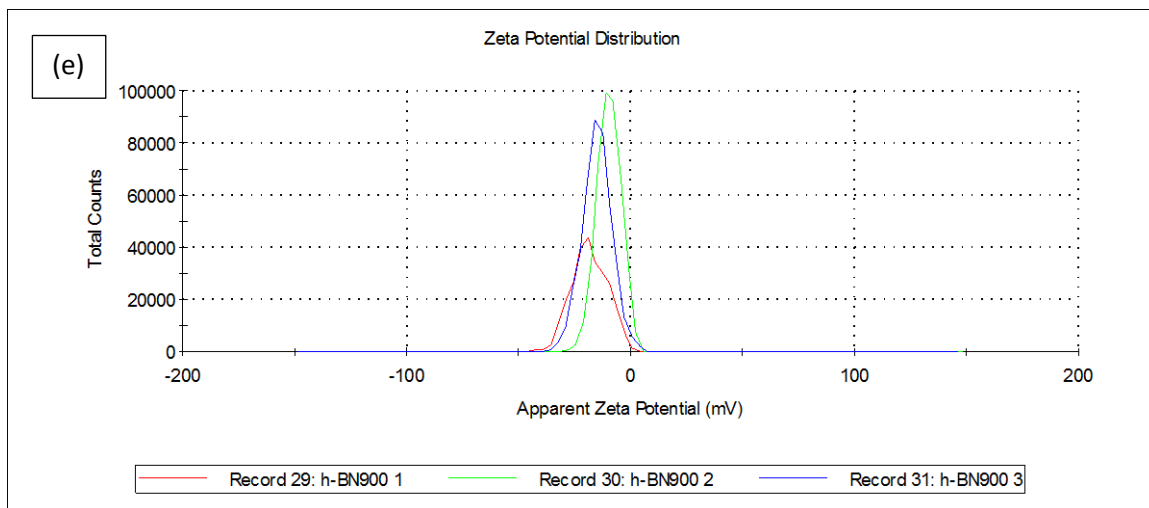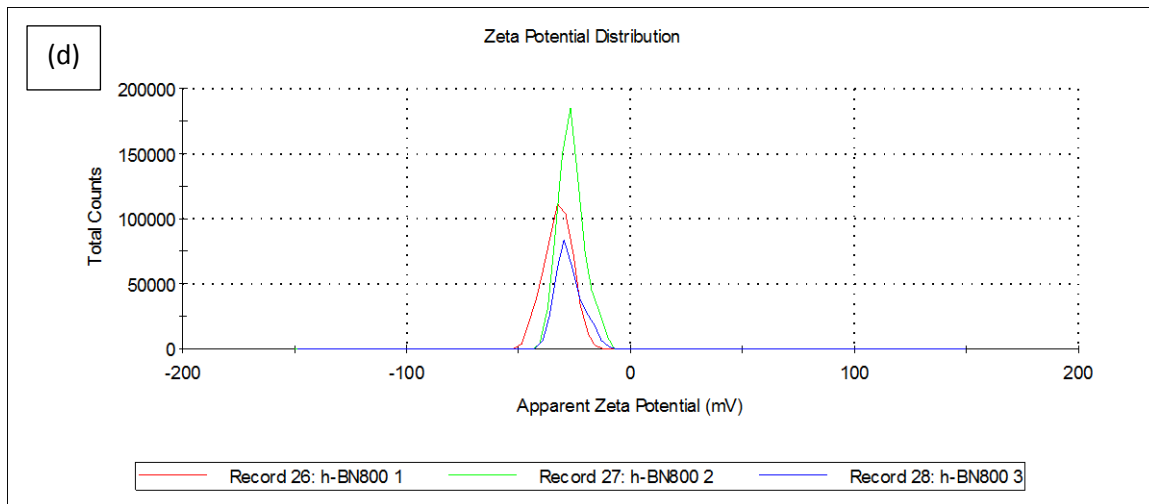
Figure 5. 4: The illustration of particle size distribution and electro-kinetic zeta potential for three different records of (a) and (d) 800 °C, (b) and (e) 900 °C and (c) and (f) 1000 °C respectively.

5.2.5 HR-TEM analysis

High-Resolution Transmission Electron Microscopy (HR-TEM) was utilised to study the crystal structures, specimen orientations and chemical compositions of phases of h-BNNSs samples fired at 800, 900 and 1000 °C under N_2 as shown in Figure 5.5, 5.6 and 5.7 respectively. The figures verify the nanoscale of the fabricated BN samples and the formation of the nanosheets with a stack of several layers indicated by the lattice fringes. It can be observed in Figure 5.5(a) that at 800 °C, the material is still covered with ash like amorphous phase of BN crystal as confirmed by the above instrumental analysis, which indicates the phase change process of the nanosheets. In Figure 5.5(b) and (c), the straight lines and circular shape like spheres at 100 and 50 nm magnification represent the existence of the lattice fringes, and by further increasing the magnification to 20 nm, the lattice fringes start to be fully visible. That is regarded as an indication of a stack of several layers estimated to range between 8 – 14 layers (see Figure 5.5(d)). In Figure 5.5(d), the lattice fringes are not fully visible at a lower magnification, because of the ash like amorphous phase of BN that is still covering the entire surface of the nanosheets. However, the existence of the layers through fringes allows their visualisation at high magnification of 20 nm. In Figure 5.6 and 5.7 (a and b images) the morphology depicts a stack of very fine nanocrystals, self-organised and agglomerated sheets forming a mini stack of several layers, which seem to be sitting well parallel to each other, however been wrinkled at the edges. The slight holes indicate the existence of the dislocations/defects of the bonds containing B and/or N atoms, which are in good agreement with other reported instrumental findings [320].
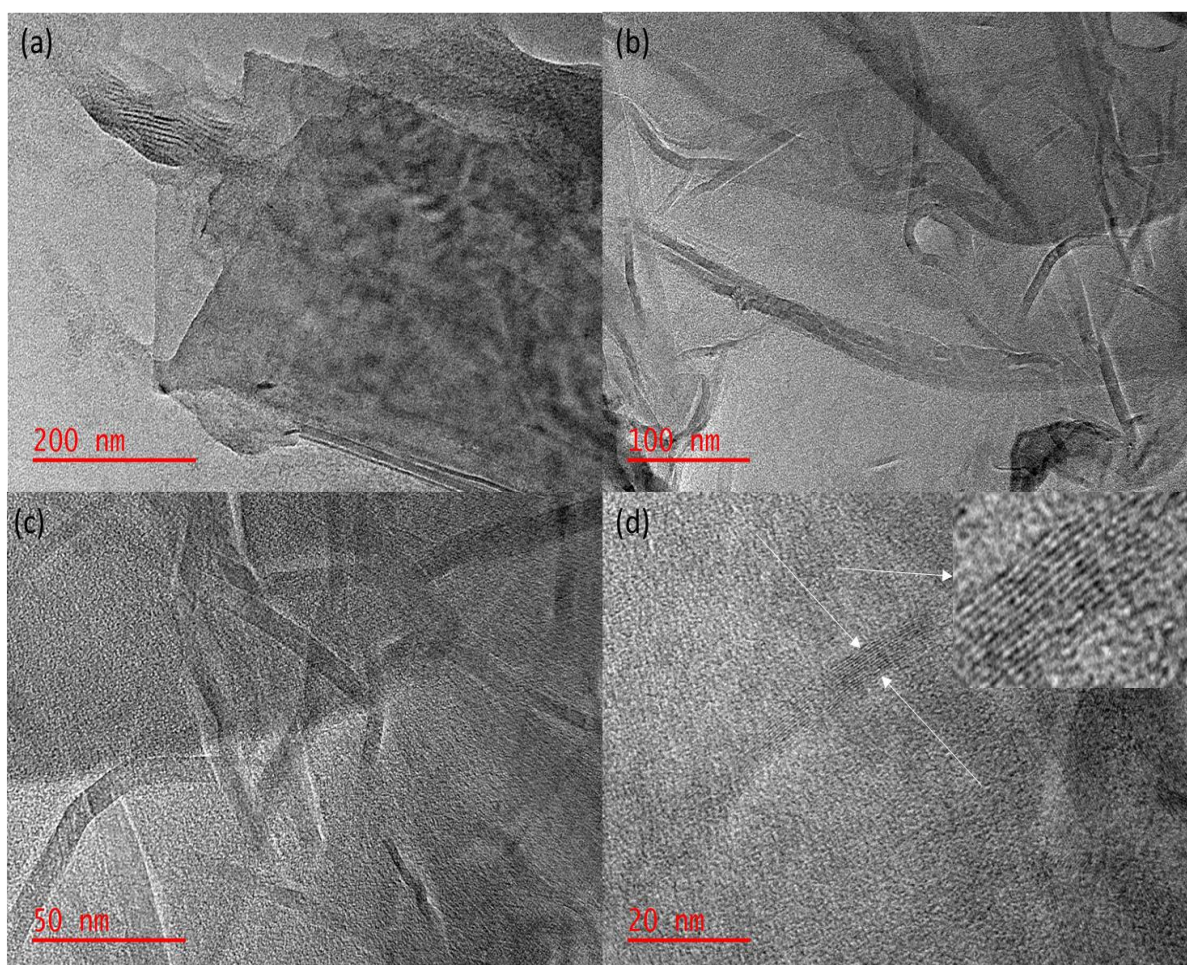
Figure 5. 5: TEM nano-graphs of h-BNNSs fabricated at 800 °C (a) 200 nm magnification of h-BNNSs, (b) 100 nm magnification of h-BNNSs and (c) and (d) 50 and 20 nm magnification for the visualisation of the lattice fringes of h-BNNSs respectively.

Additionally, there is a decline in the number of layers indicated by the decrease in the lattice fringes with an increase in temperature for the samples fabricated at 900 and 1000 °C. The number of layers are estimated to range between 3 and 5 layers (see Figure 5.6(d) and 5.7(d)). The decrease in number of lattice fringes play a very important role in increasing the surface area of the material, since the surface area of h-BN is known to increase with a decrease in the number of layers [320].
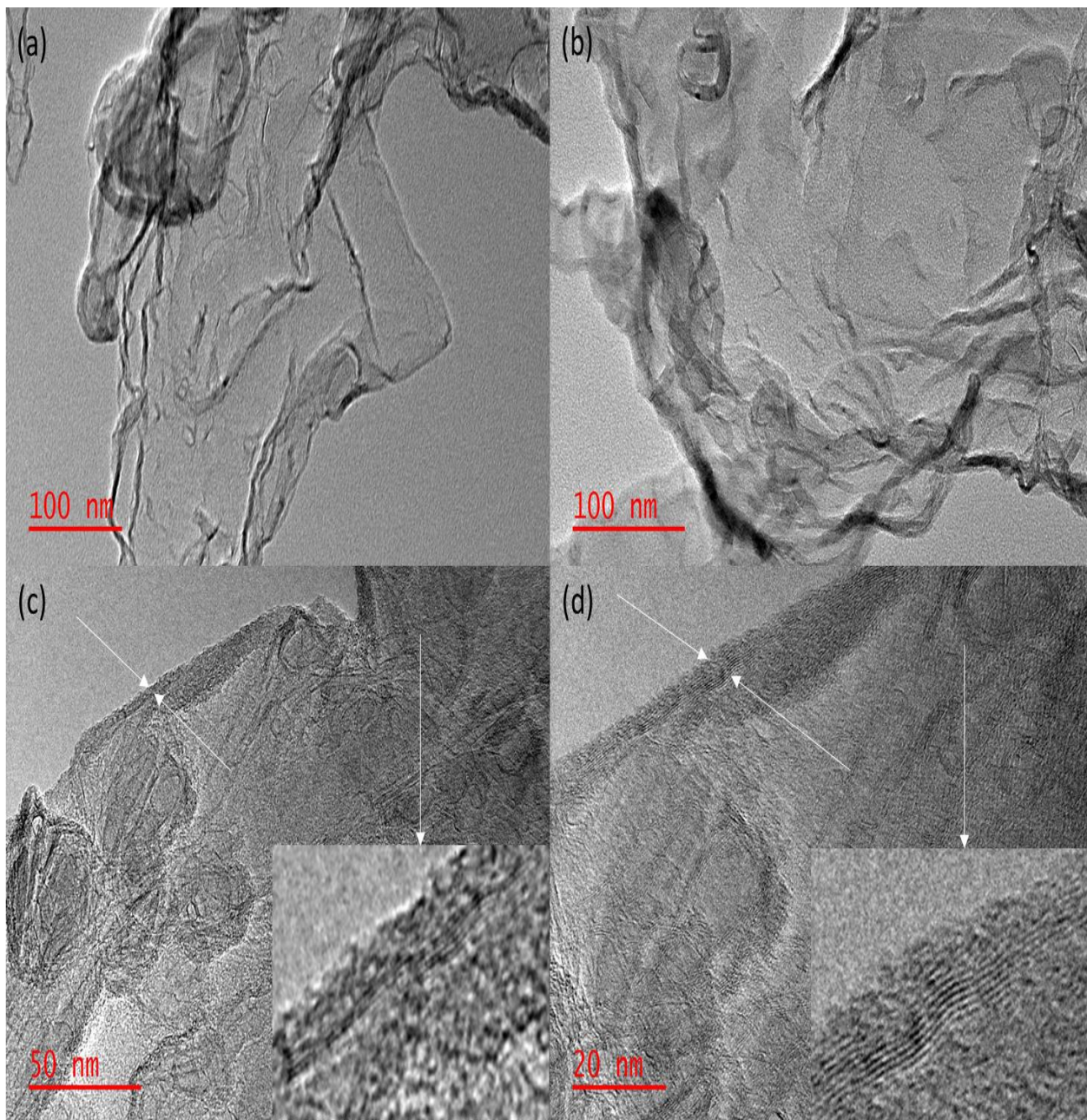
Figure 5. 6: TEM nano-graphs of h-BNNSs fabricated at 900 °C (a) 100 nm magnification of h-BNNSs, (b) 100 nm magnification of h-BNNSs at a different angle and (c) and (d) 50 and 20 nm magnification for the visualisation of the lattice fringes of h-BNNSs respectively.
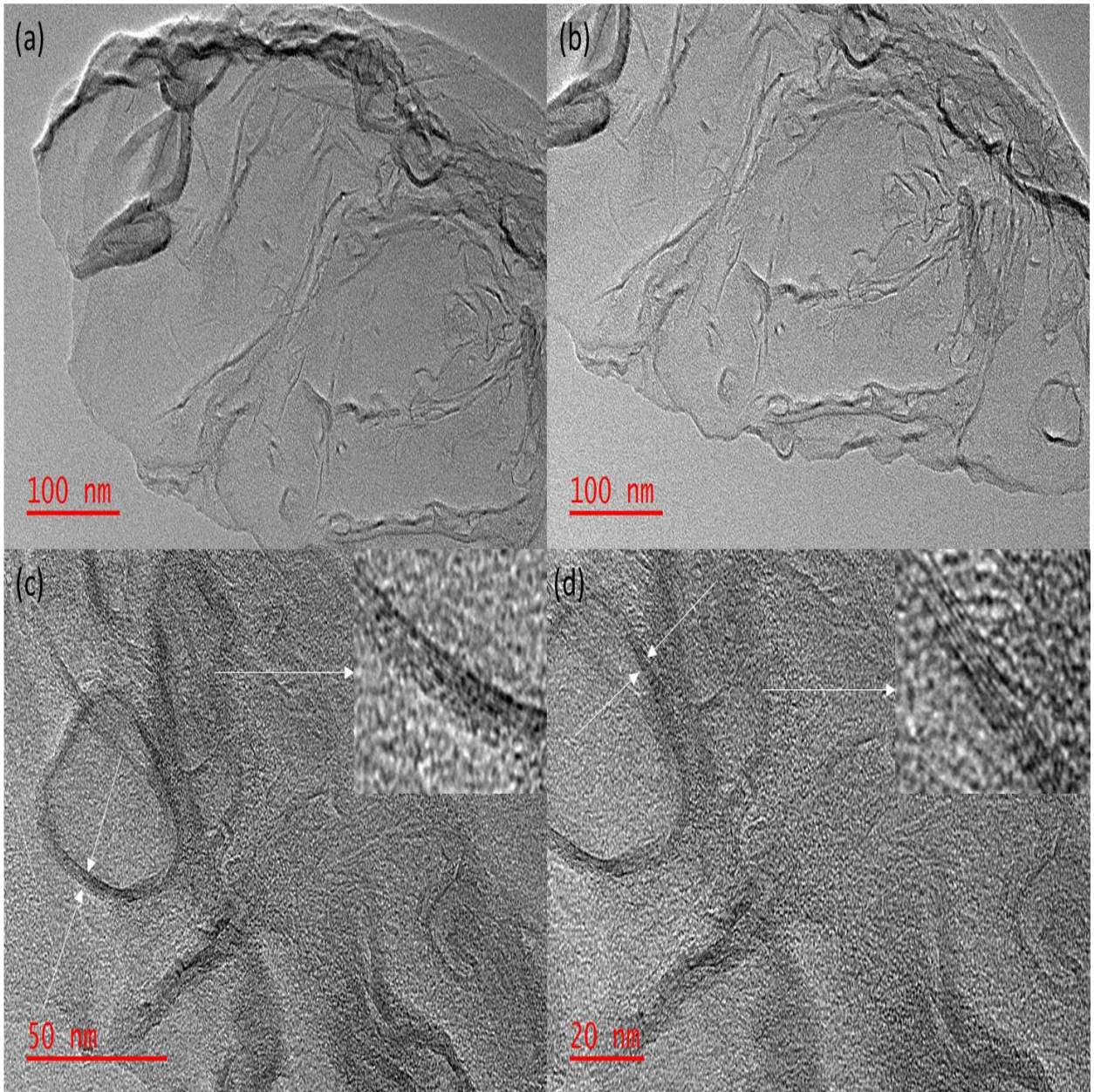
Figure 5. 7: TEM nano-graphs of h-BNNSs fabricated at 1000 °C (a) 100 nm magnification of h-BNNSs, (b) 100 nm magnification of h-BNNSs at a different angle and (c) and (d) 50 and 20 nm magnification for the visualisation of the lattice fringes of h-BNNSs respectively.

In Figures 5.6 and 5.7 the materials have completely transformed into the hexagonal phase of BN, confirmed by the full visibility of the lattice fringes at a lower

magnification of 50 nm for the samples fired at 900 and 1000 °C and well self-organised nanosheets. Furthermore, the high visibility and clear parallel lattice fringes at lower magnification observed through HR-TEM verifies the high crystalline nature of the samples [307]. Moreover, the spacing of the 2D lattice fringes was measured to be (0.38 nm) of the obtained nano-BN powders, which correspond to the (002) hexagonal phase of BN with a P63mc (180) space group. These results are totally in good agreement with the XRD patterns of the h-BNNSs for all the samples, together with the results reported in literature [307].

5.2.6 EDS analysis

Chemical analysis of the atoms present in the h-BNNSs was conducted through Energy Dispersion Spectroscopy (EDS) shown in Figure 5.8 and, three elements present in the material are depicted. The elements are boron (B), nitrogen (N) and oxygen (O) with an elemental composition of 42.0% of N, 41.3% of B, which forms the inner part of the material. The 16.7% of O, is mostly on the surface of the material.
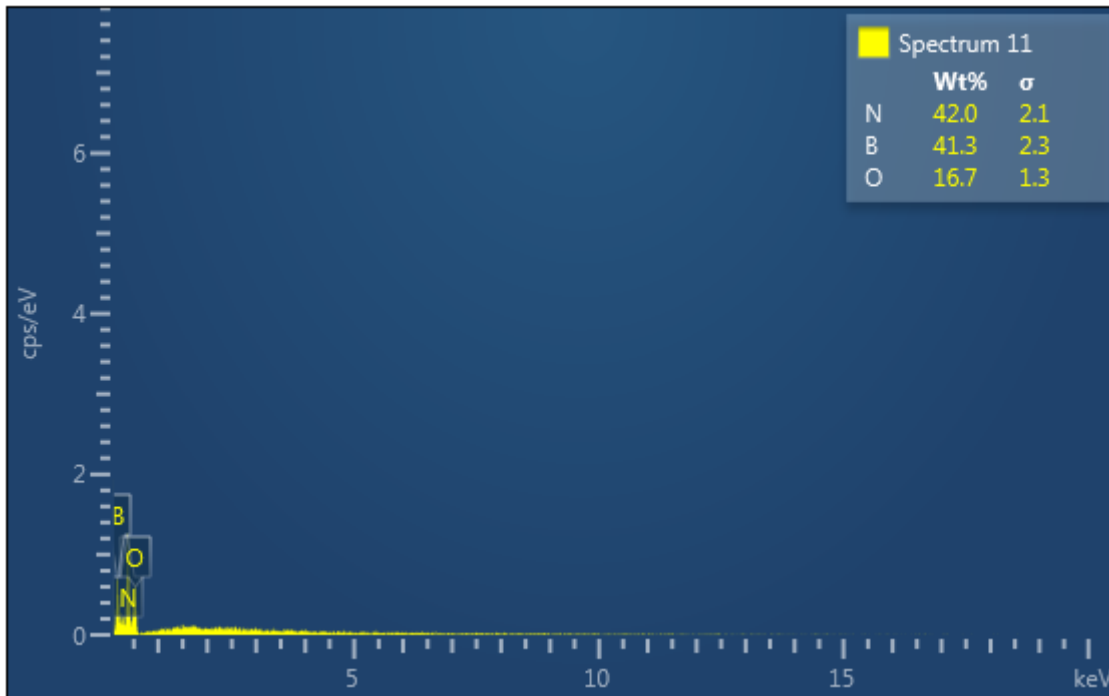
Figure 5. 8: EDS sketch for the elemental analysis of h-BNNSs for all the samples.

The elemental compositions of B and N atoms, which are almost the same, clearly shows that there is adequately equal stoichiometric ratio of the two atoms within the material. In addition, the peak that is associated with the O atom might be attributed to the substrates used or may be due to the samples not being fully dehydrated before the deposition can take place as stated in the methodology. Because we cannot expect O by cross contamination during the deposition process, as the synthesis was carried out under high vacuum. Moreover, BN compound deposition process is known to be very stable with respect to oxidation [272]. Therefore, it is clear that the existence of O on the surface of the material is from the surface of the quarts substrates or from the incomplete dehydration of the material. These finding were also verified to be in good agreement with the results reported by *Sajjad and Feng* [272].

5.2.7 RS analysis

The examination of the crystal quality of the h-BNNSs synthesised at three different temperatures of 800, 900 and 1000 °C were done through Raman Spectroscopy (RS). The Raman signal of h-BN is theoretically known to be extremely weak, and only the E_{2g} modes are Raman active which are comparable to the G-peak in graphene [321]. There are two detectable frequency vibrational peaks in proportion to the E_{2g} mode, the one with low frequency centred at 52.5 cm^{-1} and a high frequency peak centred at 1366 cm^{-1} [322] and, additionally the higher frequency mode of BN is also known to exhibits a vibrational mode in a range of 1364 – 1371 cm^{-1}, which its peak intensity is dependent on the number of layers [321, 323]. Theoretically it is known that the lower frequency mode peak is hardly detectible, which is associated with the interlayer vibrations, while the usually detectable high frequency mode is known to be associated to the in-plane vibrations where B and N atoms vibrate in opposite directions. The signal for the high frequency mode is roughly 50 times stronger than the lower frequency one [322, 324]. However, in this study, low and high frequency modes were detected with the help of Horiba Scientific Raman Spectroscopy (HSRS) using visible light operating with an excitation wavelength of 532 nm, where the lower frequency modes E_{1g} appeared to have red-shifted and centred at 144, 105 and 114 cm^{-1} for samples at h-BN800°C, h-BN900°C and h-BN1000°C which are associated with the interlayer vibrations as depicted in Figure 5.9. The E_{2g} higher frequency mode appears to have red-shifted as well and appears at 1375 cm^{-1}, slightly out of the theoretically specified range for h-BN800°C sample, which might be due to the specified phase change (see HR-TEM, XRD results). In the case of both h-BN900°C and h-BN1000°C samples the E_{2g} mode appeared at 1371 cm^{-1}, which fell within the range reported in literature [322, 324].

Furthermore, the peak intensity of the E_{2g} vibrational mode is known to increase with an increase in the number of layers and vice versa, which can in turn be used to estimate the number of layers. Therefore, as depicted in Figure 5.9, it is observed that the peak intensity of the E_{2g} mode decreases with an increase in temperature, which in turn suggests that the number of h-BN layers decreases with an increase in temperature, as also suggested by the examination of the specimen orientation through HR-TEM. The other detected frequency modes are, *D*-peak that appeared at 1556, 1553 and 1556 cm^{-1} symbolising the defects or disorder on the hexagonal sheet and *2D* mode that appeared at 2330, 2330 and 2328 cm^{-1} attributed to the stacking of the hexagonal sheets for samples h-BN800°C, h-BN900°C and h-BN1000°C. Furthermore, as the temperature was increased from 800 to 900 and 1000 °C, the E_{2g} mode blue-shifted 4 cm^{-1} from 1375 cm^{-1} to 1371 cm^{-1} suggesting the full transformation of amorphous to hexagonal phase of BN crystal.
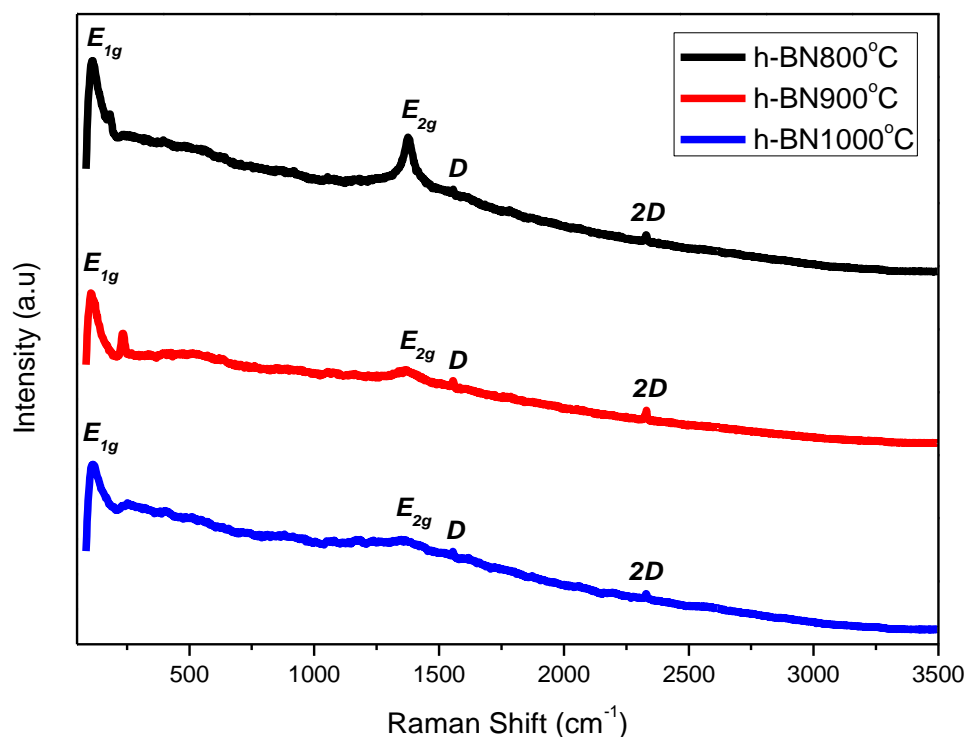
Figure 5. 9: Raman spectroscopy analysis for h-BNNSs at three different

In addition, the peak intensity of the *2D* for h-BNNSs was factually decreasing with an increase in temperature, where from 800 to 900 °C was relatively less, signifying the decrease in the dislocations or defects concentration. However, from 900 to 1000 °C the *2D* peak intensity relatively increased, which signifies an increase in the defects or dislocation concentration of the bonds containing B or N atoms, as suggested by the FTIR findings. Moreover, the intensity ratios of the I_{2D} and I_{E2g} (I_{2D}/I_{E2g}) for all the materials fabricated at 800, 900 and 1000 °C increased from 0.35 to 0.54 for h-BN800°C to h-BN900°C. This findings further confirms the decrease in number of layers of the h-BNNSs, where from 900 to 1000 °C the ratio slightly decreased from 0.54 to 0.49. This is an indication of a slight increase in the number of layers, which might be due to the influence of the defects bonds, recombining the sheets again as a result of the dislocations of the bonds containing B or N atoms.

Another point to note, on the materials fabricated at 900 and 1000 °C there are Raman detected peaks that are not usually observed as disclosed in literature, which appears as 236 and 1058 cm^{-1} for h-BN900°C material and 1166 and 1079 cm^{-1} for h-BN1000°C material, which might be attributed to the attachment of the (*-O-H*) and (*N-H*) on the surface of the materials after ultra-sonication process. Finally, the Raman findings suggest that h-BN800°C material has bulk sheets of h-BN with the layers ranging from 8 – 14, where for the materials h-BN900°C and h-BN1000°C, the sheets number ranges from 3 – 5 layers which are as well complemented by the HR-TEM results.

5.2.8 BET analysis

Brunauer-Emmett-Teller (BET) analysis is one of the most used tools for examining the surface properties of the material and was used in the study to examine the surface area of h-BNNSs. Figure 5.10 depicts the nitrogen adsorption-desorption isotherms of h-BN800°C, h-BN900°C and h-BN1000°C respectively. As shown in Figure 5.10, the adsorption-desorption isotherms of the aforementioned materials according to the International Union of Pure and Applied Chemistry (IUPAC) classification, the nanosheets belong to the type-IV isotherms, which guarantee their mesoporous structure [325], as portrayed by the hysteresis loop from 0.8 – 1.0 (P/P0). The surface area of the nanosheets were found to factually increase with temperature (see Table 5.2). However, in all the samples the surface area was observed to be very small in comparison to what has been disclosed by *Shahabuddin et al.* [326]. These might be due to the different methodological procedures adopted in our studies. h-BN800°C has higher surface area as compared to h-BN900°C and h-BN1000°C; the higher surface area might be due to the different

morphologies/phases present in the sample, which relatively increases the porosity of the material that led to the high surface area of the nanocomposites.
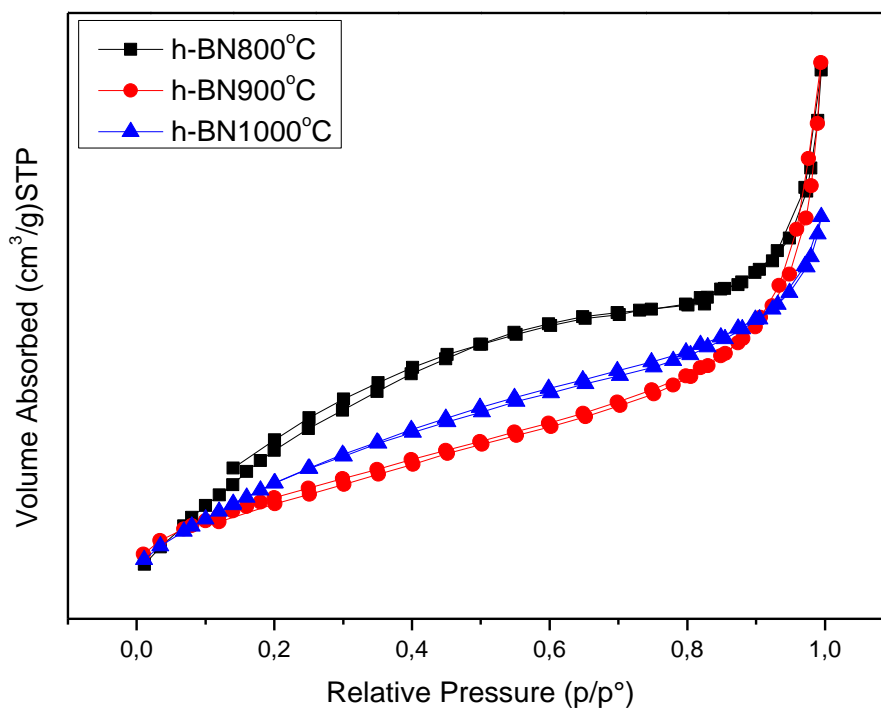
Figure 5. 10: Nitrogen adsorption-desorption isotherms (BET) of h-BN800°C, h-BN900°C and h-BN1000°C respectively.

Table 5. 3: BET specific surface area

Sample	BET surface area (m^2/g)
h-BN800°C	1.23
h-BN900°C	0.50
h-BN1000°C	1.14

The specific surface area of the h-BNNSs are presented in Table 5.2. As evident from the obtained BET results, the surface area of the nanocomposites were observed to decrease from 800 to 900 °C. The decrease in the surface area upon increasing the temperature might be due to the agglomeration and wrinkledness of the nanosheets at higher temperature. While the slight increase in the surface area from 900 to 1000 °C was also observed, which is as a result of the increase in the disordering of the bonds containing B and/or N atoms. Thus, the surface examination of the nanocomposites outlined the surface area of the nanosheets, which is an important aspect for every practical sensor.

5.3 Conclusion

The effects of temperature on the synthesis of the nanosheets was well studied by means of CVD technique. The results attests that the h-BNNSs were successfully synthesised at 800, 900 and 1000 °C. At 800 °C, the material was found to contain different phases. The RS and HR-TEM confirms the agglomeration of the nanosheets with the reduction of layer number with temperature elevation. Moreover, the nanosheets were found to consist of various defects, which were observed to elevate with synthetic temperature. The calculated direct energy band gap confirmed the remarkable semiconducting properties of the nanosheets. BET results confirmed h-BN800°C to have larger surface area in comparison to h-BN900°C and h-BN1000°C.

Chapter 6

Gas Sensing studies on h-BN nanosheets

6.1 Introduction

Ultra-thin 2D nanomaterials have attracted a huge scientific interest in the field of gas sensing due to their delightful properties such as better surface area, high electron mobility, stable atomic layer, low costs, easy to use and portability [58, 328, 329]. The successful implementation of ultra-thin nanomaterials such as graphene and molybdenum disulphide (MoS_2) have brought much interest to 2D h-BNNSs as a semiconductor-based gas sensor, due to its acceptable practical applications. 2D h-BNNSs is a wide band gap semiconducting based gas sensor, which is known to be physically and thermally stable in air up to 1500 °C and chemically inert [141, 327]. Therefore, due to its remarkable properties, it became one of the most appealing semiconductor materials within a variety of ultra-thin nanomaterials for producing gas sensors and shows ability for toxic gas detection [42]. Due to its remarkable ultra-thin properties, the nanosheets allows the total exposure of all its atoms to the adsorbing gas molecules, which increases the sensitivity of sensors. This allows the detection of gases at both low and high gas concentrations (ppm) at various operating temperatures. The nanosheets are ideal candidates for monitoring a fragment amount of toxic gases such as CO and H_2S for better human breathe, environmental monitoring in areas where toxic gases begin to threaten livelihood both indoors and outdoors. This chapter accounts on the gas sensing performance of the as-

synthesised 2D h-BNNSs (h-BN800, h-BN900 and h-BN1000) towards H_2S and CO gases at various gas concentrations (ppm) with temperature elevation.

6.2 Fabrication of sensors and sensing measurements

To prepare the sensor device, the alumina intergidited electrodes (2 mm x 2 mm) with one side having Pt-electrode and one side having micro-heater were used for gas sensing measurements. The h-BNNSs samples were dispersed in ethanol to form a paste and dropped uniformly onto the Pt-electrodes of alumina substrate. The impregnated substrate was then heated at 80 °C for 1 hour to remove the solvent and for adhesion of the paste. The gas sensing measurements were conducted using a gas sensing station KSGAS6S (KENOSISTEC, Italy). The measurements were tested at 50, 100, 150, 200 and 250 °C by the voltage change on the sensing carbon monoxide (CO) and hydrogen sulphide (H_2S) gases in the surroundings. Synthetic air with a constant flow rate of 0.5 l/min was used as carrier gas. The changes in electrical conductivity of nanomaterials subsequent to exposure to gas was used for determination of the gas response as:

$$Gas\ response = \frac{R_a - R_g}{R_a} \qquad\qquad 6.1$$

Where R_a and R_g characterise the conductance of nanomaterials in the air and upon exposure to gas. Response and recovery time were chosen as time required for reaching 90% of maximum response subsequent to exposure of nanomaterials to a gas, and time required for regaining 90% of the original conductance in the air respectively.

6.3 Evaluation of the gas sensing performance of h-BNNSs towards H₂S and CO gases

6.3.1 Response and recovery properties

The gas sensing performance of the nanosheets fabricated at 800, 900 and 1000 °C was examined for CO and H_2S at the operating temperatures ranging from 50, 100, 150, 200 and 250 °C as depicted in Figure 6.1. The sensing properties of pure h-BNNSs were tested on the concentrations of 5 to 100 ppm of CO and H_2S gas, and the temperature was varied in order to settle an optimum operating temperature with a maximum response. 2D h-BNNSs as a p-type semiconductor-based gas sensor shows remarkable gas sensing properties when exposed to H_2S as a reducing gas [330-332]. When the p-type semiconductor materials is exposed to a reducing gas the resistivity increases due to the electron transfer into the conduction band, while for an n-type the opposite takes place. As can be seen from Figure 6.1 (a-e), the h-BN800 sensor towards H_2S showed a maximum response in all the temperatures. The high H_2S response of h-BN800 sensor could be attributed to higher surface area, the small grain size, the presence of various phases in the sample, which facilitate porous structure and stabilise the sensor and high defect/disordering concentration, which increases the sensitivity of sensors. It has been reported that the surface area can positively influence the sensitivity of the sensor [21, 36, 37]. h-BN800 showed an optimum gas response of 1.56, 2.20, 2.40 and 3.20 for gas concentrations of 40, 60, 80 and 100 ppm respectively at an operating temperature of 250 °C. Overall, h-BN800 was found to exhibit great sensitivity and response to H_2S gas better than h-BN900 and h-BN1000. Most importantly, it can be seen that all

the fabricated sensors in this study respond very well at low gas concentrations of 5 ppm, this is a good attribute that is required for environmental sensor applications.
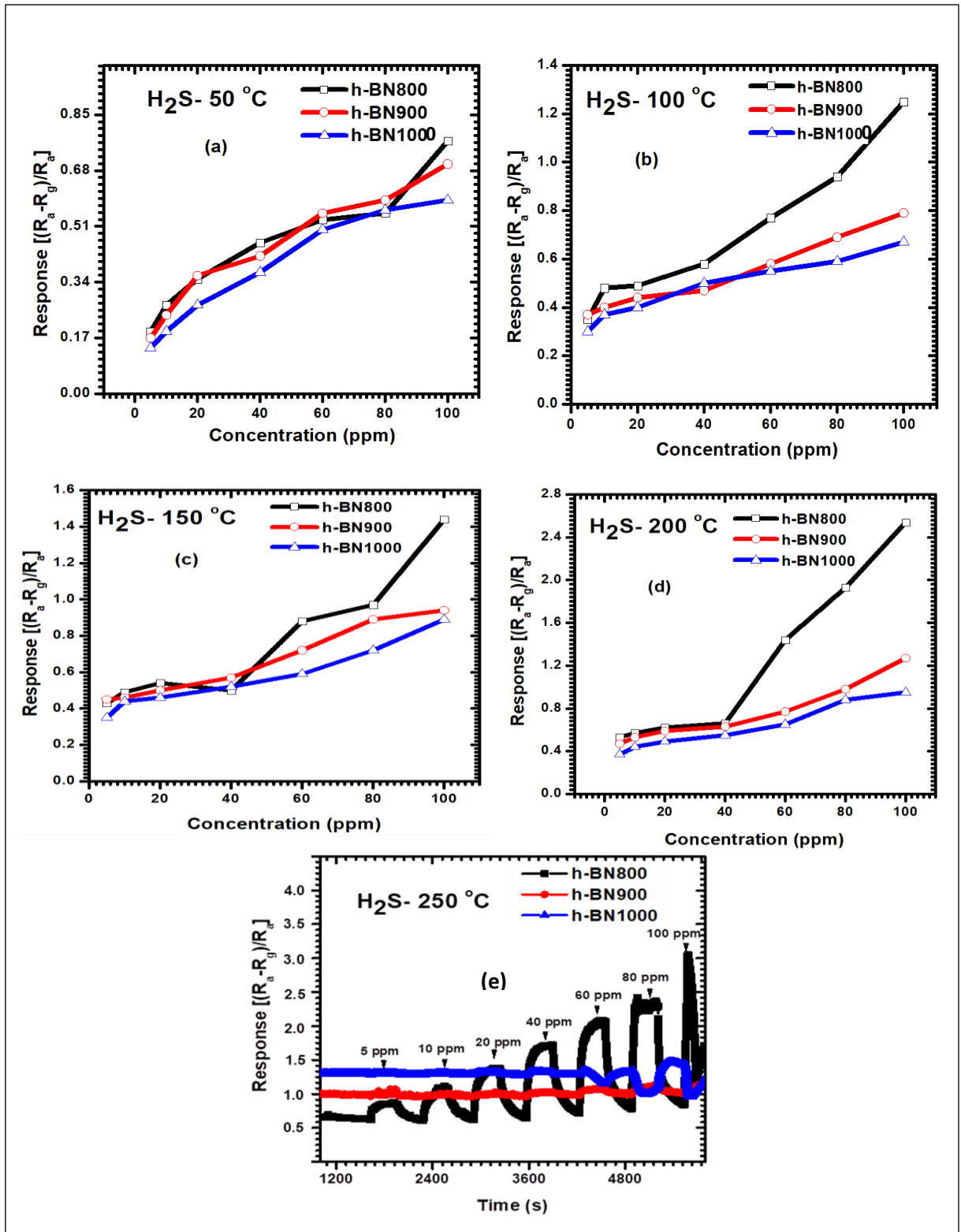
Figure 6. 1: The gas-sensing plots of: Dynamic response curves of h-BNNSs sensor against H_2S gas concentrations at (a) 50, (b) 100, (c) 150, and (d) 200 °C; Also, (e) is the response and recovery of the nanosheets over a broad spectrum of H_2S gas concentration at 250 °C.

Additionally, the maximum response was observed at 250 °C (see Figure 6.2) in all samples with the response values of 150, 100, 85, 67 and 64 for 50, 100, 150, 200 and 250 °C, respectively at 40 ppm H_2S concentration. This indicates an increase in sensor response with the increase in operating temperature. The increase in response with increase in operating temperature may be attributed to strong adsorption, high diffusion depth of the atoms at high temperatures and tuneable band gaps that enhances the electronic properties of the sensors. Furthermore, the sensitivity of the nanosheets were found to decrease with an increase in the synthetic temperature. This is due to the decrease in the surface area of the nanosheets with an increase in the synthetic temperature as expressed by the BET results. Hence, h-BN800 was able to exhibit better sensitivity and response towards H_2S as compared to h-BN900 and h-BN1000, simply because of higher surface area over the other two sensors. Moreover, the current findings attests that all the fabricated sensors in this work portrays an acceptable sensitivity and response at both low and high H_2S gas concentrations, which is a good attribution for practical sensors.
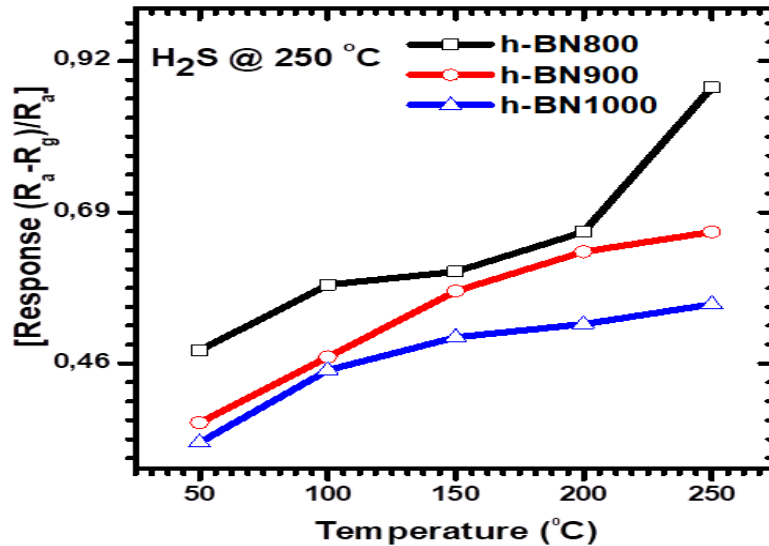
Figure 6. 2: Responses of nanosheets fabricated at 800, 900 and 1000 °C exposed to H_2S gas of 40 ppm concentration at different operating temperatures.

6.3.2 Sensitivity study on CO

The response behaviour of the h-BNNSs fabricated at 800, 900 and 1000 °C and later exposed on varying CO gas concentrations (in ppm) with increasing temperature are displayed in Figure 6.3. The results suggests that h-BN800, h-BN900 and h-BN1000 sheets behave absolutely alike when subjected to CO gas. However, the response time of the sensors was observed to increase even with a small amount of CO gas at elevated temperature, which is not convincing to resolve the h-BNNSs as good sensors towards CO gas. h-BNNSs were particularly found to be less sensitive towards CO within the specified temperature range of 50 – 250 °C, as compared to the H_2S gas. It can be agreed that the h-BNNSs sensors are good in the detection of H_2S gas.
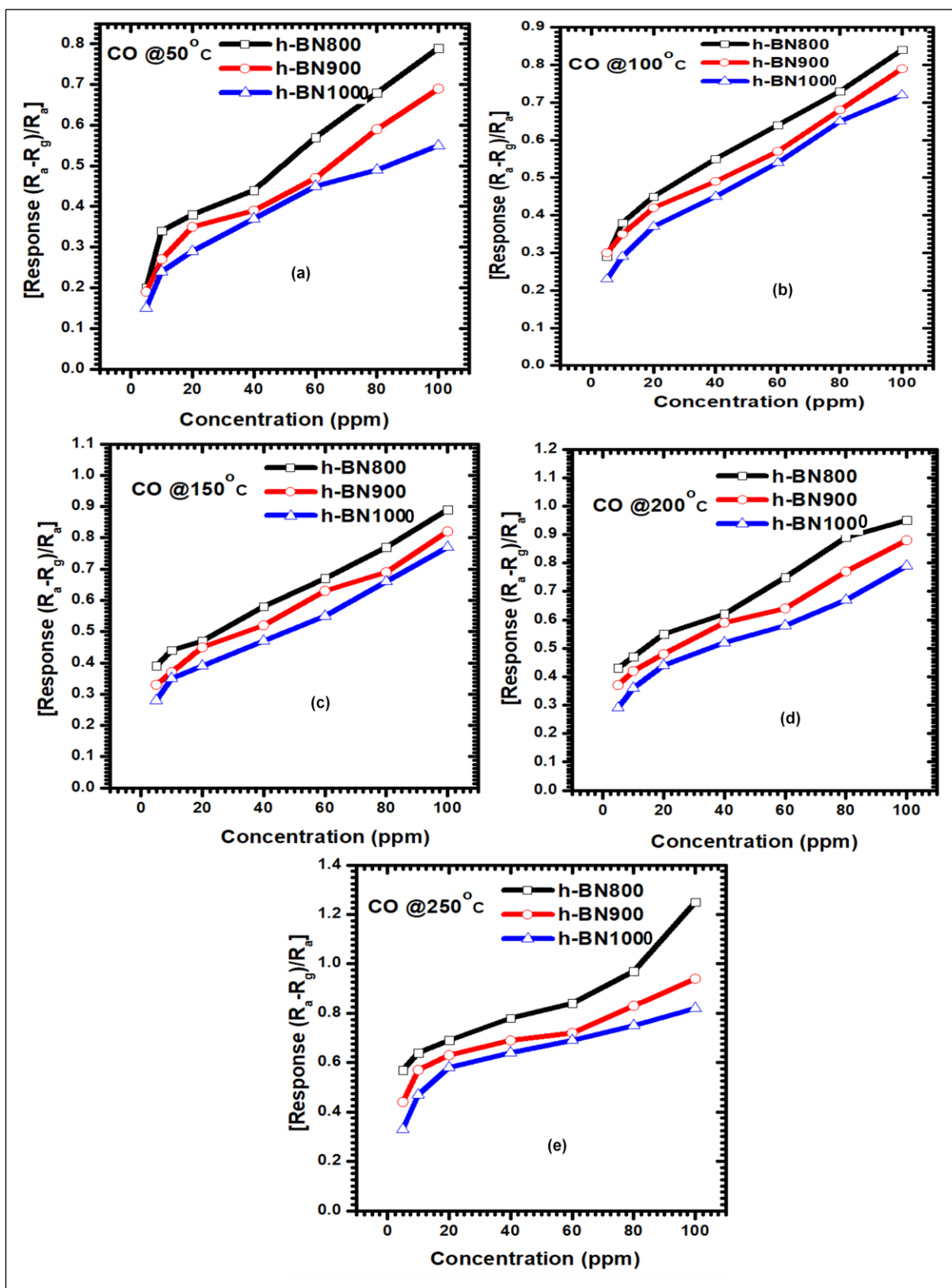
Figure 6. 3: Dynamic H_2S sensing response/recovery curves at various gas concentration for (a) 50 °C, (b) 100 °C, (c) 150 °C, (d) 200 °C, (e) 250 °C.

6.3.3 Response and recovery times

The response and recovery time of ultra-thin semiconductors-based gas sensor are another important factor in gas sensing analysis. Which is why the response and recovery times were investigated in this study as depicted in Figure 6.4. Table 6.1 also shows the response and recovery times of the fabricated sensors when exposed to H_2S gas of 40 ppm concentration at 250 °C temperature. The response time is normally described as the time taken by the sensor to reach 90% of equilibrium after the introduction of the gas of interest, while the recovery time is the time taken by the sensor to reach 90% of its original resistance in the absence of a gas. As displayed in Table 6.1, h-BN900 shows a fast response and short recovery time towards H_2S gas as compared to h-BN800 and h-BN1000. The response and recovery attributions of the as-synthesised h-BNNSs at various temperatures are depicted in Figure 6.4 at a gas concentration of 40 ppm and an operating temperature of 250 °C. The h-BNNSs as the semiconductor-based gas sensors showed a quick and acceptable response and recovery time towards H_2S gas. Thus, as per the results expressed in the Figure 6.4, all the nanocomposites were found to exhibits good response, recovery, and reproducibility characteristics towards 40 ppm H_2S gas at 250 °C temperature.

Table 6. 1: Response and recovery times of pure 2D h-BNNSs evaluated as 40 ppm H$_2$S gas concentration.

Samples	H$_2$S gas at 40ppm	
	Response time (s)	Recovery time (s)
h-BN800	97	100
h-BN900	67	75
h-BN1000	138	89
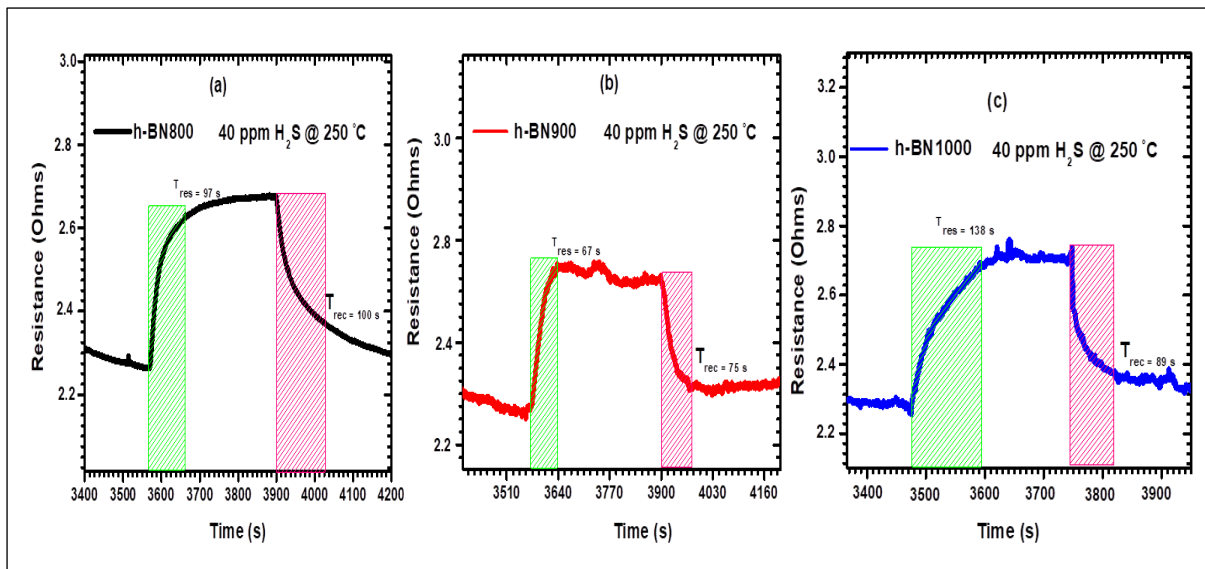
Figure 6. 4: Dynamic H$_2$S sensing resistance vs time curves at (a) h-BN800 towards 40ppm H$_2$S gas at 250°C, (b) h-BN900 towards 40ppm H$_2$S gas at 250°C, (c) h-BN1000 towards 40ppm H$_2$S gas at 250°C.

6.3.4 Gas sensing mechanism

2D h-BNNSs as a semiconductor-based gas sensor, is a p-type semiconductor due to its property as a hole carrier. H_2S is an electron donor gas, which is ionised when adsorbed on the surface of the nanosheets sensing thin films. Thus, bringing about a decrease in the concentration of the positive charge hole carriers on the surface of the nanosheets, which ultimately result in partial reduction in the devise conductance [333]. Therefore, the h-BN nanosheets were observed to change gradually from the conductive state to the insulating state, leading to an increase in resistance of the nanosheets. By setting, free the H_2S molecules and protons through passing on the clean air in the gas chamber, the resistance of the h-BN nanosheets based sensors ultimately recovered to its normal state [334].

6.4 Conclusion

The effects of temperature on the sensing ability of the nanosheets on different gas concentrations of H_2S and CO toxic gases was studied. The results attest that the nanosheets at 800 °C were found to fabricate with different BN crystal configurations, which might explain the enhanced sensing performance of the h-BN800 sheets. It was also observed that the h-BN1000 nanosheets with uniform crystallinity have compromised yet acceptable sensitivity towards H_2S compared to CO gas. To comprehend the findings, it was also observed that h-BN800 sheets demonstrated appreciable sensitivity and response towards 40 ppm of H_2S at 250 °C temperature. Most importantly, the fabricated sensors were all found to respond very well at low concentrations of 5 ppm. In addition, h-BN900 sheets showed both response and recovery time at 40 ppm of H_2S and 250 °C.

Chapter 7

Summary and Conclusion

The structural behaviour of 2D h-BNNSs/white graphene for 144, 324 and 576 atoms supercells together with their defected vacancy formation have been studied by means of classical molecular dynamics simulations. Throughout the calculations, the Tersoff potentials were utilised to explain the interactions between the B and N atoms. Calculated *g(r)* and *S(k)* outcomes demonstrated how the B-B, B-N and N-N first and second nearest neighbour distances are arranged in defect free, B and N vacancy h-BNNSs supercells. Structural properties predicted by the classical MD were confirmed by the XRD measurements. The diffusion coefficients with respect to both B and N atoms demonstrated the surface mobility of the atoms with an increase in the surface area. Furthermore, the calculated entropy changes of both defect free and defected supercells demonstrated the number of possible arrangements of the atoms within the surface of the materials, which was as well found to be increasing with an increase in the surface area. To add on that, structural 2D stability improved with enhanced surface area. The coefficients of linear thermal expansion demonstrate a complex scenario as the supercell surface area increases with temperature. At larger supercells multiple coefficients of expansion are noted, some of negative values. This observation is associated with the surface bending of nanosheets notable with the TEM measurements. These findings are further complemented by the visualisation of NVT and NPT ensembles at 1000 and 1200 K. Both the results of defect free and defected nanosheets, where all found to compare and agree well with each other. In the same routine, the 2D h-BNNSs were synthesised using the wet chemical reaction synthesis, thereafter different analytical

instruments were utilised to examine the effect of temperature on the nanosheets. The outcomes of all the analytical studies attests that the nanosheets were fully synthesised at a minimum temperature of 800 °C and a maximum temperature of 1000 °C. However, the nanosheets synthesised at 800 °C were found to be covered with ash-like amorphous phase of BN, which confirms that the material consists of different phases within the same material. The combination was further found to enhance the sensing performance of the nanosheets. As the temperature was further increased, the defects on the surface of the nanosheets were found to elevate with an increase in the synthetic temperature which in-turn enhanced the electronic properties of the materials. In addition, the stiffness of the nanosheets fabricated at 1000 °C was found to have reduced due to the absence of the layer-by-layer interaction however with a small percentage. The Raman E_{2g} frequency modes demonstrate the reduction in the number of layers with elevation of temperature, which was also complemented by the HR-TEM findings. The examination of the surface properties through BET, showed the nanosheets of h-BN800 portraying higher surface area over the h-BN900 and h-BN1000. Both the computational and experimental finding, were found to complement and concur well with each other, such a finding is observed through similarities in parameters calculated and other quantities. Additionally, the nanosheets were taken for gas sensing application in order to examine their performance towards H_2S and CO gases at different operating temperatures. The sensors showed great response towards H_2S as compared to CO. On the H_2S gas sensing, h-BN800 sample showed great response compared to the other two samples (h-BN900 and h-BN1000). This was attributed to high surface area, small crystallite size, the presence of different phases in the sample. All this facilitate porous nature with high defect/disordering concentration towards increased

sensitivity of sensors. Furthermore, the sample fabricated at 900 °C (h-BN900) showed great response and recovery time towards H_2S over the other two samples (h-BN800 and h-BN1000), which is due to the full crystallinity and high reduction of the band gap of the nanosheets. However, the response and recovery times of other two samples are of outmost practically acceptable for practical sustainable sensors. On comparison to other 2D planar sensors, h-BNNSs, a semiconductor-based gas sensor is convincing to demonstrate acceptable gas sensing performance, exhibiting cost effective standards and sustainable performance for global utility.

References

1. Lee, R., Keller, F. and Meyer, B., 2017. A concept to support the transformation from a linear to circular carbon economy: net zero emissions, resource efficiency and conservation through a coupling of the energy, chemical and waste management sectors. Clean Energy, 1(1), pp.102-113.

2. Bhattacharya, K., Kapoor, S. and Suri, N., 2017. An Optimised Platinum (Pt) Doped Tin-oxide (SnO2) Ink for Deposition of Gas Sensing Thick Film on LTCC Micro-hotplate. Material Science Research India, 14(2), pp.158-163.

3. Chen, T., Kuschner, W., Gokhale, J. and Shofer, S., 2007. Outdoor Air Pollution: Nitrogen Dioxide, Sulfur Dioxide, and Carbon Monoxide Health Effects. The American Journal of the Medical Sciences, 333(4), pp.249-256.

4. Raub, J., Mathieu-Nolf, M., Hampson, N. and Thom, S., 2000. Carbon monoxide poisoning — a public health perspective. Toxicology, 145(1), pp.1-14.

5. Allred, E., Bleecker, E., Chaitman, B., Dahms, T., Gottlieb, S., Hackney, J., Pagano, M., Selvester, R., Walden, S. and Warren, J., 1989. Short-Term Effects of Carbon Monoxide Exposure on the Exercise Performance of Subjects with Coronary Artery Disease. New England Journal of Medicine, 321(21), pp.1426-1432.

6. HU, C.Z., LI, F. and LIU, X.D. (2008). Theoretical study on gas sensing properties of boron nitride nanotubes. Acta Chimica Sinica, (66), pp.1641.

7. Rubio, A., Corkill, J. and Cohen, M. (1994). Theory of graphitic boron nitride nanotubes. Physical Review B, 49(7), pp.5081-5084.

8. Honeybourne, C., Ewen, R. and Hill, C., 1984. Use of thin films of conjugated organic macrocycles as the active elements in toxic-gas sensors operating at room temperature. Journal of the Chemical Society, Faraday Transactions 1: Physical Chemistry in Condensed Phases, 80(4), p.851.

9. Eranna, G., Joshi, B., Runthala, D. and Gupta, R., 2004. Oxide Materials for Development of Integrated Gas Sensors—A Comprehensive Review. Critical Reviews in Solid State and Materials Sciences, 29(3-4), pp.111-188.

10. Korolkoff, N.O., 1989. Survey of toxic gas sensors and monitoring systems, Solid State Technol, 32(12), pp.49–63.

11. Schedin, F., Geim, A., Morozov, S., Hill, E., Blake, P., Katsnelson, M. and Novoselov, K., 2007. Detection of individual gas molecules adsorbed on graphene. Nature Materials, 6(9), pp.652-655.

12. Rumyantsev, S., Liu, G., Shur, M., Potyrailo, R. and Balandin, A., 2012. Selective Gas Sensing with a Single Pristine Graphene Transistor. Nano Letters, 12(5), pp.2294-2298.

13. Perkins, F., Friedman, A., Cobas, E., Campbell, P., Jernigan, G. and Jonker, B., 2013. Chemical Vapor Sensing with Mono-layer MoS2. Nano Letters, 13(2), pp.668-673.

14. Rumyantsev, S., Liu, G., Potyrailo, R., Balandin, A. and Shur, M., 2013. Selective Sensing of Individual Gases Using Graphene Devices. IEEE Sensors Journal, 13(8), pp.2818-2822.

15. Samnakay, R., Jiang, C., Rumyantsev, S., Shur, M. and Balandin, A., 2015. Selective chemical vapor sensing with few-layer MoS2 thin-film transistors: Comparison with graphene devices. Applied Physics Letters, 106(2), p.023115.

16. Ganatra, R. and Zhang, Q., 2014. Few-Layer MoS_2: A Promising Layered Semiconductor. ACS Nano, 8(5), pp.4074-4099.

17. Mak, K., Lee, C., Hone, J., Shan, J. and Heinz, T., 2010. Atomically ThinMoS2: A New Direct-Gap Semiconductor. Physical Review Letters, 105(13).

18. Late, D., Huang, Y., Liu, B., Acharya, J., Shirodkar, S., Luo, J., Yan, A., Charles, D., Waghmare, U., Dravid, V. and Rao, C., 2013. Sensing Behavior of Atomically Thin-Layered MoS2 Transistors. ACS Nano, 7(6), pp.4879-4891.

19. Fandrich, M., Mehrtens, T., Aschenbrenner, T., Klein, T., Gebbe, M., Figge, S., Kruse, C., Rosenauer, A. and Hommel, D., 2013. Nitride based heterostructures with Ga- and N-polarity for sensing applications. Journal of Crystal Growth, 370, pp.68-73.

20. Yu, S., Wang, X., Pang, H., Zhang, R., Song, W., Fu, D., Hayat, T. and Wang, X., 2018. Boron nitride-based materials for the removal of pollutants from aqueous solutions: A review. Chemical Engineering Journal, 333, pp.343-360.

21. Lu, G., Ocola, L. and Chen, J., 2009. Reduced graphene oxide for room-temperature gas sensors. Nanotechnology, 20(44), p.445502.

22. Zhang, Y., Chen, Y., Zhou, K., Liu, C., Zeng, J., Zhang, H. and Peng, Y., 2009. Improving gas sensing properties of graphene by introducing dopants and defects: a first-principles study. Nanotechnology, 20(18), p.185504.

23. Son, Y., Cohen, M. and Louie, S., 2007. Erratum: Energy Gaps in Graphene Nanoribbons [Phys. Rev. Lett.97, 216803 (2006)]. Physical Review Letters, 98(8), p.216803.

24. Han, M., Özyilmaz, B., Zhang, Y. and Kim, P., 2007. Energy Band-Gap Engineering of Graphene Nanoribbons. Physical Review Letters, 98(20), p.206805.

25. Hoffman, D., Doll, G. and Eklund, P., 1984. Optical properties of pyrolytic boron nitride in the energy range 0.05—10 eV. Physical Review B, 30(10), pp.6051-6056.

26. Du, A., Smith, S. and Lu, G., 2007. First-principle studies of electronic structure and C-doping effect in boron nitride nanoribbon. Chemical Physics Letters, 447(4-6), pp.181-186.

27. Zhuang, H. and Hennig, R., 2012. Electronic structures of single-layer boron pnictides. Applied Physics Letters, 101(15), p.153109.

28. Wu, X., Wu, M. and Zeng, X., 2009. Chemically decorated boron-nitride nanoribbons. Frontiers of Physics in China, 4(3), pp.367-372.

29. Zheng, F., Zhang, J., Zhang, Y. and Ji, V., 2010. First-principles study of the perfect and vacancy defect AlN nanoribbon. Physica B: Condensed Matter, 405(17), pp.3775-3781.

30. Lipp, A., Schwetz, K. and Hunold, K., 1989. Hexagonal boron nitride: Fabrication, properties and applications. Journal of the European Ceramic Society, 5(1), pp.3-9.

31. Meric, I., Dean, C., Petrone, N., Wang, L., Hone, J., Kim, P. and Shepard, K., 2013. Graphene Field-Effect Transistors Based on Boron–Nitride Dielectrics. Proceedings of the IEEE, 101(7), pp.1609-1619.

32. Chen, Y., Zou, J., Campbell, S. and Le Caer, G., 2004. Boron nitride nanotubes: Pronounced resistance to oxidation. Applied Physics Letters, 84(13), pp.2430-2432.

33. Ma, R., Bando, Y., Sato, T. and Kurashima, K., 2001. Growth, Morphology, and Structure of Boron Nitride Nanotubes. Chemistry of Materials, 13(9), pp.2965-2971.

34. Wang, J., Xu, X., Mu, X., Ma, F. and Sun, M., 2017. Magnetics and spintronics on two-dimensional composite materials of graphene/hexagonal boron nitride. Materials Today Physics, 3, pp.93-117.

35. Ghassemi, H., Lee, C., Yap, Y. and Yassar, R., 2010. In situ TEM monitoring of thermal decomposition in individual boron nitride nanotubes. JOM, 62(4), pp.69-73.

36. Pacilé, D., Meyer, J., Girit, Ç. and Zettl, A., 2008. The two-dimensional phase of boron nitride: Few-atomic-layer sheets and suspended membranes. Applied Physics Letters, 92(13), p.133107.

37. Song, L., Ci, L., Lu, H., Sorokin, P., Jin, C., Ni, J., Kvashnin, A., Kvashnin, D., Lou, J., Yakobson, B. and Ajayan, P., 2010. Large Scale Growth and

Characterisation of Atomic Hexagonal Boron Nitride Layers. Nano Letters, 10(8), pp.3209-3215.

38. Yu, W., Lau, W., Chan, S., Liu, Z. and Zheng, Q., 2003. Ab initiostudy of phase transformations in boron nitride. Physical Review B, 67(1).

39. Xu, Y. and Ching, W., 1991. Calculation of ground-state and optical properties of boron nitrides in the hexagonal, cubic, and wurtzite structures. Physical Review B, 44(15), pp.7787-7798.

40. Mikołajczyk, J., Bielecki, Z., Stacewicz, T., Smulko, J., Wojtas, J., Szabra, D., Prokopiuk, A. and Magryta, P., 2016. Detection of gaseous compounds with different techniques. Metrology and Measurement Systems, 23(2), pp.205-224.

41. Nubi, O.O., 2016. Single and double doping of nanostructured titanium dioxide with silver and copper: structural, optical and gas-sensing properties (Doctoral dissertation).

42. Sajjad, M. and Feng, P., 2014. Study the gas sensing properties of boron nitride nanosheets. Materials Research Bulletin, 49, pp.35-38.

43. Weng, Q., Wang, X., Zhi, C., Bando, Y. and Golberg, D. (2013). Boron Nitride Porous Microbelts for Hydrogen Storage. ACS Nano, 7(2), pp.1558-1565.

44. Vallero, D. and Letcher, T. (2012). Engineering Risks and Failures: Lessons Learned from Environmental Disasters. Leadership and Management in Engineering, 12(4), pp.199-209.

45. Massera, E., La Ferrara, V., Miglietta, M., Polichetti, T., Nasti, I. and Di Francia, G., 2011. Gas sensors based on graphene. chimica oggi/Chemistry Today, 29(1).

46. Tricoli, A., Righettoni, M. and Teleki, A., 2010. Semiconductor gas sensors: dry synthesis and application. Angewandte Chemie International Edition, 49(42), pp.7632-7659.

47. Yamazoe, N., Sakai, G. and Shimanoe, K., Catal Surv Asia. 2003; 7: 63–75. doi: 10.1023. A: 1023436725457.[Cross Ref].

48. Cacciari, I. and Righini, G.C., 2009. Optical gas sensing. In Solid State Gas Sensing (pp. 1-28). Springer, Boston, MA.

49. Wetchakun, K., Samerjai, T., Tamaekong, N., Liewhiran, C., Siriwong, C., Kruefu, V., Wisitsoraat, A., Tuantranont, A. and Phanichphant, S., 2011. Semiconducting metal oxides as sensors for environmentally hazardous gases. Sensors and Actuators B: Chemical, 160(1), pp.580-591.

50. Nyembe, S.G., 2018. Group III-V nanostructures application in gas sensing (Doctoral dissertation).

51. Wang, L.C., Tang, K.T., Teng, I.J., Kuo, C.T., Ho, C.L., Kuo, H.W., Su, T.H., Yang, S.R., Shi, G.N. and Chang, C.P., 2011. A single-walled carbon nanotube network gas sensing device. Sensors, 11(8), pp.7763-7772.

52. Srivastava, A., Singh, V., Dhand, C., Kaur, M., Singh, T., Witte, K. and Scherer, U.W., 2006. Study of swift heavy ion modified conducting polymer composites for application as gas sensor. Sensors, 6(4), pp.262-269.

53. Liu, X., Cheng, S., Liu, H., Hu, S., Zhang, D. and Ning, H., 2012. A survey on gas sensing technology. Sensors, 12(7), pp.9635-9665.

54. Hwang, W.J., Shin, K.S., Roh, J.H., Lee, D.S. and Choa, S.H., 2011. Development of micro-heaters with optimised temperature compensation design for gas sensors. Sensors, 11(3), pp.2580-2591.

55. Jimenez, I., Vilà, A.M., Calveras, A.C. and Morante, J.R., 2005. Gas-sensing properties of catalytically modified WO/sub 3/with copper and vanadium for NH/sub 3/detection. IEEE Sensors Journal, 5(3), pp.385-391.

56. Refaat, T.F., Ismail, S., Koch, G.J., Rubio, M., Mack, T.L., Notari, A., Collins, J.E., Lewis, J., De Young, R., Choi, Y. and Abedin, M.N., 2010. Backscatter 2-$\mu\hbox {m} $ Lidar Validation for Atmospheric $\hbox {CO} _ {2} $ Differential Absorption Lidar Applications. IEEE transactions on geoscience and remote sensing, 49(1), pp.572-580.

57. Yu, B., Liu, D. and Zhang, T., 2011. Fault diagnosis for micro-gas turbine engine sensors via wavelet entropy. Sensors, 11(10), pp.9928-9941.

58. Varghese, S., Lonkar, S., Singh, K., Swaminathan, S. and Abdala, A., 2015. Recent advances in graphene based gas sensors. Sensors and Actuators B: Chemical, 218, pp.160-183.

59. Tan, C. and Zhang, H., 2015. Wet-chemical synthesis and applications of non-layer structured two-dimensional nanomaterials. *Nature Communications*, 6(1).

60. Zhao, Z., Yang, Z., Wen, Y. and Wang, Y., 2011. Facile Synthesis and Characterisation of Hexagonal Boron Nitride Nanoplates by Two-Step Route. *Journal of the American Ceramic Society*, 94(12), pp.4496-4501.

61. Alkoy, S., Toy, C., Gönül, T. and Tekin, A., 1997. Crystallization behavior and Characterisation of turbostratic boron nitride. *Journal of the European Ceramic Society*, 17(12), pp.1415-1422.

62. Golberg, D., Bando, Y., Huang, Y., Terao, T., Mitome, M., Tang, C. and Zhi, C., 2010. Boron Nitride Nanotubes and Nanosheets. *ACS Nano*, 4(6), pp.2979-2993

63. Lin, Y. and Connell, J., 2012. Advances in 2D boron nitride nanostructures: nanosheets, nanoribbons, nanomeshes, and hybrids with graphene. *Nanoscale*, 4(22), p.6908.

64. Novoselov, K., Jiang, D., Schedin, F., Booth, T., Khotkevich, V., Morozov, S. and Geim, A., 2005. Two-dimensional atomic crystals. *Proceedings of the National Academy of Sciences*, 102(30), pp.10451-10453.

65. Chopra, N., Luyken, R., Cherrey, K., Crespi, V., Cohen, M., Louie, S. and Zettl, A., 1995. Boron Nitride Nanotubes. *Science*, 269(5226), pp.966-967.

66. Golberg, D., Bando, Y., Stéphan, O. and Kurashima, K., 1998. Octahedral boron nitride fullerenes formed by electron beam irradiation. *Applied Physics Letters*, 73(17), pp.2441-2443.

67. Terrones, M., Charlier, J., Gloter, A., Cruz-Silva, E., Terrés, E., Li, Y., Vinu, A., Zanolli, Z., Dominguez, J., Terrones, H., Bando, Y. and Golberg, D., 2008. Experimental and Theoretical Studies Suggesting the Possibility of Metallic

Boron Nitride Edges in Porous Nanourchins. *Nano Letters*, 8(4), pp.1026-1032.

68. Chen, Z., Zou, J., Liu, G., Li, F., Wang, Y., Wang, L., Yuan, X., Sekiguchi, T., Cheng, H. and Lu, G., 2008. Novel Boron Nitride Hollow Nanoribbons. *ACS Nano*, 2(10), pp.2183-2191.

69. Zhao, Z., Yang, Z., Wen, Y. and Wang, Y., 2011. Facile Synthesis and Characterisation of Hexagonal Boron Nitride Nanoplates by Two-Step Route. *Journal of the American Ceramic Society*, 94(12), pp.4496-4501.

70. Ingo, G., Padeletti, G., de Caro, T., Riccucci, C., Faraldi, F., Curulli, A., Mezzi, A. and Piccinini, M., 2011. Novel route to high-yield synthesis of sp2-hybridized boron nitride nanoplates on stainless steel. *Journal of Materials Chemistry*, 21(28), p.10268.

71. Deepak, F., Vinod, C., Mukhopadhyay, K., Govindaraj, A. and Rao, C., 2002. Boron nitride nanotubes and nanowires. *Chemical Physics Letters*, 353(5-6), pp.345-352.

72. Qiu, Y., Yu, J., Yin, J., Tan, C., Zhou, X., Bai, X. and Wang, E., 2009. Synthesis of continuous boron nitride nanofibers by solution coating electrospun template fibers. *Nanotechnology*, 20(34), p.345603.

73. Zheng, M., Gu, Y., Xu, Z. and Liu, Y., 2007. Synthesis and Characterisation of boron nitride nanoropes. *Materials Letters*, 61(8-9), pp.1943-1945.

74. Yu, Y., Chen, H., Liu, Y., White, T. and Chen, Y., 2012. Preparation and potential application of boron nitride nanocups. *Materials Letters*, 80, pp.148-151.

75. Pakdel, A., Bando, Y. and Golberg, D., 2013. Morphology-Driven Nonwettability of Nanostructured BN Surfaces. *Langmuir*, 29(24), pp.7529-7533.

76. Yin, J., Li, X., Zhou, J. and Guo, W., 2013. Ultralight Three-Dimensional Boron Nitride Foam with Ultralow Permittivity and Superelasticity. *Nano Letters*, 13(7), pp.3232-3236.

77. Huang, B., Lee, H., Gu, B., Liu, F. and Duan, W., 2011. Edge stability of boron nitride nanoribbons and its application in designing hybrid BNC structures. *Nano Research*, 5(1), pp.62-72.

78. Mukherjee, R. and Bhowmick, S., 2011. Edge Stabilities of Hexagonal Boron Nitride Nanoribbons: A First-Principles Study. *Journal of Chemical Theory and Computation*, 7(3), pp.720-724.

79. Khan, M., Liu, H., Sun, X., Yamauchi, Y., Bando, Y., Golberg, D. and Huang, Z., 2017. Few-atomic-layered hexagonal boron nitride: CVD growth, Characterisation, and applications. *Materials Today*, 20(10), pp.611-628.

80. Ribeiro, R. and Peres, N., 2011. Stability of boron nitride bilayers: Ground-state energies, interlayer distances, and tight-binding description. *Physical Review B*, 83(23).

81. Constantinescu, G., Kuc, A. and Heine, T., 2013. Stacking in Bulk and Bilayer Hexagonal Boron Nitride. *Physical Review Letters*, 111(3).

82. Hod, O., Peralta, J. and Scuseria, G., 2007. Edge effects in finite elongated graphene nanoribbons. *Physical Review B*, 76(23).

83. Fernández-Rossier, J. and Palacios, J., 2007. Magnetism in Graphene Nanoislands. *Physical Review Letters*, 99(17).

84. Ezawa, M., 2007. Metallic graphene nanodisks: Electronic and magnetic properties. *Physical Review B*, 76(24).

85. Shemella, P., Zhang, Y., Mailman, M., Ajayan, P. and Nayak, S., 2007. Energy gaps in zero-dimensional graphene nanoribbons. *Applied Physics Letters*, 91(4), p.042101

86. Hariharan, P. and Pople, J., 1973. The influence of polarisation functions on molecular orbital hydrogenation energies. *Theoretica Chimica Acta*, 28(3), pp.213-222.

87. Boys, S. and Bernardi, F., 1970. The calculation of small molecular interactions by the differences of separate total energies. Some procedures with reduced errors. *Molecular Physics*, 19(4), pp.553-566.

88. Simon, S., Duran, M. and Dannenberg, J., 1996. How does basis set superposition error change the potential surfaces for hydrogen-bonded dimers?. *The Journal of Chemical Physics*, 105(24), pp.11024-11031.

89. Polo, V., Gräfenstein, J., Kraka, E. and Cremer, D., 2003. Long-range and short-range Coulomb correlation effects as simulated by Hartree-Fock, local density approximation, and generalized gradient approximation exchange functionals. *Theoretical Chemistry Accounts: Theory, Computation, and Modeling (Theoretica Chimica Acta)*, 109(1), pp.22-35.

90. Perdew, J., Burke, K. and Ernzerhof, M., 1996. Generalized Gradient Approximation Made Simple. *Physical Review Letters*, 77(18), pp.3865-3868.

91. Zhao, Y. and Truhlar, D., 2008. Density Functionals with Broad Applicability in Chemistry. *Accounts of Chemical Research*, 41(2), pp.157-167.

92. Zhao, Y. and Truhlar, D., 2007. The M06 suite of density functionals for main group thermochemistry, thermochemical kinetics, noncovalent interactions,

excited states, and transition elements: two new functionals and systematic testing of four M06-class functionals and 12 other functionals. *Theoretical Chemistry Accounts*, 120(1-3), pp.215-241.

93. Hirshfeld, F., 1977. Bonded-atom fragments for describing molecular charge densities. *Theoretica Chimica Acta*, 44(2), pp.129-138.

94. Lennard-Jones, J. and Dent, B., 1928. Cohesion at a crystal surface. *Transactions of the Faraday Society*, 24, p.92.

95. Tkatchenko, A. and Scheffler, M., 2009. Accurate Molecular Van Der Waals Interactions from Ground-State Electron Density and Free-Atom Reference Data. *Physical Review Letters*, 102(7).

96. Fumi, F. and Tosi, M., 1960. Extension of the Madelung Method for the Evaluation of Lattice Sums. *Physical Review*, 117(6), pp.1466-1468.

97. Li, Q., Zou, X., Liu, M., Sun, J., Gao, Y., Qi, Y., Zhou, X., Yakobson, B., Zhang, Y. and Liu, Z., 2015. Grain Boundary Structures and Electronic Properties of Hexagonal Boron Nitride on Cu(111). *Nano Letters*, 15(9), pp.5804-5810.

98. Stone, A. and Wales, D., 1986. Theoretical studies of icosahedral C60 and some related species. *Chemical Physics Letters*, 128(5-6), pp.501-503.

99. Ma, J., Alfè, D., Michaelides, A. and Wang, E., 2009. Stone-Wales defects in graphene and other planarsp2-bonded materials. *Physical Review B*, 80(3).

100. Meyer, J., Kisielowski, C., Erni, R., Rossell, M., Crommie, M. and Zettl, A., 2008. Direct Imaging of Lattice Atoms and Topological Defects in Graphene Membranes. *Nano Letters*, 8(11), pp.3582-3586.

101. Banhart, F., Kotakoski, J. and Krasheninnikov, A., 2010. Structural Defects in Graphene. *ACS Nano*, 5(1), pp.26-41.

102.   Kotakoski, J., Krasheninnikov, A., Kaiser, U. and Meyer, J., 2011. From Point Defects in Graphene to Two-Dimensional Amorphous Carbon. *Physical Review Letters*, 106(10).

103.   Nozaki, H. and Itoh, S., 1996. Structural stability of BC2N. *Journal of Physics and Chemistry of Solids*, 57(1), pp.41-49.

104.   Pokropivny, V., Skorokhod, V., Oleinik, G., Kurdyumov, A., Bartnitskaya, T., Pokropivny, A., Sisonyuk, A. and Sheichenko, D., 2000. Boron Nitride Analogs of Fullerenes (the Fulborenes), Nanotubes, and Fullerites (the Fulborenites). *Journal of Solid State Chemistry*, 154(1), pp.214-222.

105.   Liu, Y., Zou, X. and Yakobson, B., 2012. Dislocations and Grain Boundaries in Two-Dimensional Boron Nitride. *ACS Nano*, 6(8), pp.7053-7058.

106.   Gibb, A., Alem, N., Chen, J., Erickson, K., Ciston, J., Gautam, A., Linck, M. and Zettl, A., 2013. Atomic Resolution Imaging of Grain Boundary Defects in Mono-layer Chemical Vapor Deposition-Grown Hexagonal Boron Nitride. *Journal of the American Chemical Society*, 135(18), pp.6758-6761.

107.   Cretu, O., Lin, Y. and Suenaga, K., 2014. Evidence for Active Atomic Defects in Mono-layer Hexagonal Boron Nitride: A New Mechanism of Plasticity in Two-Dimensional Materials. *Nano Letters*, 14(2), pp.1064-1068.

108.   Yazyev, O. and Chen, Y., 2014. Polycrystalline graphene and other two-dimensional materials. *Nature Nanotechnology*, 9(10), pp.755-767.

109.   Zobelli, A., Ewels, C., Gloter, A. and Seifert, G., 2007. Vacancy migration in hexagonal boron nitride. *Physical Review B*, 75(9).

110. Jin, C., Lin, F., Suenaga, K. and Iijima, S., 2009. Fabrication of a Freestanding Boron Nitride Single Layer and Its Defect Assignments. *Physical Review Letters*, 102(19).

111. Han, T., Luo, Y. and Wang, C., 2013. Effects of temperature and strain rate on the mechanical properties of hexagonal boron nitride nanosheets. *Journal of Physics D: Applied Physics*, 47(2), p.025303.

112. Bosak, A., Serrano, J., Krisch, M., Watanabe, K., Taniguchi, T. and Kanda, H., 2006. Elasticity of hexagonal boron nitride: Inelastic x-ray scattering measurements. *Physical Review B*, 73(4).

113. Peng, Q., Ji, W. and De, S., 2012. Mechanical properties of the hexagonal boron nitride mono-layer: Ab initio study. *Computational Materials Science*, 56, pp.11-17.

114. Mirnezhad, M., Ansari, R. and Rouhi, H., 2013. Mechanical properties of multilayer boron nitride with different stacking orders. *Superlattices and Microstructures*, 53, pp.223-231.

115. Wu, J., Wang, B., Wei, Y., Yang, R. and Dresselhaus, M., 2013. Mechanics and Mechanically Tunable Band Gap in Single-Layer Hexagonal Boron-Nitride. *Materials Research Letters*, 1(4), pp.200-206.

116. Thomas, S., Ajith, K. and Valsakumar, M., 2016. Directional anisotropy, finite size effect and elastic properties of hexagonal boron nitride. *Journal of Physics: Condensed Matter*, 28(29), p.295302.

117. Mortazavi, B. and Rémond, Y., 2012. Investigation of tensile response and thermal conductivity of boron-nitride nanosheets using molecular dynamics simulations. *Physica E: Low-dimensional Systems and Nanostructures*, 44(9), pp.1846-1852.

118.   Zhao, S. and Xue, J., 2013. Mechanical properties of hybrid graphene and hexagonal boron nitride sheets as revealed by molecular dynamic simulations. *Journal of Physics D: Applied Physics*, 46(13), p.135303.

119.   Kudin, K., Scuseria, G. and Yakobson, B., 2001. C2F,BN, and C nanoshell elasticity fromab initiocomputations. *Physical Review B*, 64(23).

120.   Ding, N., Wu, C. and Li, H., 2014. The effect of grain boundaries on the mechanical properties and failure behavior of hexagonal boron nitride sheets. *Phys. Chem. Chem. Phys.*, 16(43), pp.23716-23722.

121.   Mortazavi, B. and Cuniberti, G., 2014. Mechanical properties of polycrystalline boron-nitride nanosheets. *RSC Adv.*, 4(37), pp.19137-19143.

122.   Kim, S., Hsu, A., Park, M., Chae, S., Yun, S., Lee, J., Cho, D., Fang, W., Lee, C., Palacios, T., Dresselhaus, M., Kim, K., Lee, Y. and Kong, J., 2015. Synthesis of large-area multilayer hexagonal boron nitride for high material performance. *Nature Communications*, 6(1).

123.   Li, C., Bando, Y., Zhi, C., Huang, Y. and Golberg, D., 2009. Thickness-dependent bending modulus of hexagonal boron nitride nanosheets. *Nanotechnology*, 20(38), p.385707.

124.   Marom, N., Bernstein, J., Garel, J., Tkatchenko, A., Joselevich, E., Kronik, L. and Hod, O., 2010. Stacking and Registry Effects in Layered Materials: The Case of Hexagonal Boron Nitride. *Physical Review Letters*, 105(4).

125.   Gao, W. and Tkatchenko, A., 2015. Sliding Mechanisms in Multilayered Hexagonal Boron Nitride and Graphene: The Effects of Directionality, Thickness, and Sliding Constraints. *Physical Review Letters*, 114(9).

126.   Mostaani, E., Drummond, N. and Fal'ko, V., 2015. Quantum Monte Carlo Calculation of the Binding Energy of Bilayer Graphene. *Physical Review Letters*, 115(11).

127.   Falin, A., Cai, Q., Santos, E., Scullion, D., Qian, D., Zhang, R., Yang, Z., Huang, S., Watanabe, K., Taniguchi, T., Barnett, M., Chen, Y., Ruoff, R. and Li, L., 2017. Mechanical properties of atomically thin boron nitride and the role of interlayer interactions. *Nature Communications*, 8(1).

128.   Zhi, C., Bando, Y., Tang, C., Kuwahara, H. and Golberg, D., 2009. Large-Scale Fabrication of Boron Nitride Nanosheets and Their Utilization in Polymeric Composites with Improved Thermal and Mechanical Properties. *Advanced Materials*, 21(28), pp.2889-2893.

129.   Zhou, H., Zhu, J., Liu, Z., Yan, Z., Fan, X., Lin, J., Wang, G., Yan, Q., Yu, T., Ajayan, P. and Tour, J., 2014. High thermal conductivity of suspended few-layer hexagonal boron nitride sheets. *Nano Research*, 7(8), pp.1232-1240.

130.   Jo, I., Pettes, M., Kim, J., Watanabe, K., Taniguchi, T., Yao, Z. and Shi, L., 2013. Thermal Conductivity and Phonon Transport in Suspended Few-Layer Hexagonal Boron Nitride. *Nano Letters*, 13(2), pp.550-554.

131.   Chen, C., Li, Z., Shi, L. and Cronin, S., 2014. Thermoelectric transport across graphene/hexagonal boron nitride/graphene heterostructures. *Nano Research*, 8(2), pp.666-672.

132.   Zhou, W., Qi, S., An, Q., Zhao, H. and Liu, N., 2007. Thermal conductivity of boron nitride reinforced polyethylene composites. *Materials Research Bulletin*, 42(10), pp.1863-1873.

133.   Jo, I., Pettes, M., Kim, J., Watanabe, K., Taniguchi, T., Yao, Z. and Shi, L., 2013. Thermal Conductivity and Phonon Transport in Suspended Few-Layer Hexagonal Boron Nitride. *Nano Letters*, 13(2), pp.550-554.

134.   Zhi, C., Xu, Y., Bando, Y. and Golberg, D., 2011. Highly Thermo-conductive Fluid with Boron Nitride Nanofillers. *ACS Nano*, 5(8), pp.6571-6577.

135.   Taha-Tijerina, J., Narayanan, T., Gao, G., Rohde, M., Tsentalovich, D., Pasquali, M. and Ajayan, P., 2012. Electrically Insulating Thermal Nano-Oils Using 2D Fillers. *ACS Nano*, 6(2), pp.1214-1220.

136.   Wang, J., Ma, F. and Sun, M., 2017. Graphene, hexagonal boron nitride, and their heterostructures: properties and applications. *RSC Advances*, 7(27), pp.16801-16822.

137.   Watanabe, K., Taniguchi, T. and Kanda, H., 2004. Direct-bandgap properties and evidence for ultraviolet lasing of hexagonal boron nitride single crystal. *Nature Materials*, 3(6), pp.404-409.

138.   Gao, R., Yin, L., Wang, C., Qi, Y., Lun, N., Zhang, L., Liu, Y., Kang, L. and Wang, X., 2009. High-Yield Synthesis of Boron Nitride Nanosheets with Strong Ultraviolet Cathodoluminescence Emission. *The Journal of Physical Chemistry C*, 113(34), pp.15160-15165.

139.   Wheelock, P., Cook, B., Harringa, J. and Russell, A., 2004. Phase changes induced in hexagonal boron nitride by high energy mechanical milling. *Journal of Materials Science*, 39(1), pp.343-347.

140.   Barone, V. and Peralta, J., 2008. Magnetic Boron Nitride Nanoribbons with Tunable Electronic Properties. *Nano Letters*, 8(8), pp.2210-2214.

141. Liao, L., Lin, Y., Bao, M., Cheng, R., Bai, J., Liu, Y., Qu, Y., Wang, K., Huang, Y. and Duan, X., 2010. High-speed graphene transistors with a self-aligned nanowire gate. *Nature*, 467(7313), pp.305-308.

142. Liu, Z., Gong, Y., Zhou, W., Ma, L., Yu, J., Idrobo, J., Jung, J., MacDonald, A., Vajtai, R., Lou, J. and Ajayan, P., 2013. Ultrathin high-temperature oxidation-resistant coatings of hexagonal boron nitride. *Nature Communications*, 4(1).

143. Lyalin, A., Nakayama, A., Uosaki, K. and Taketsugu, T., 2013. Theoretical predictions for hexagonal BN based nanomaterials as electrocatalysts for the oxygen reduction reaction. *Physical Chemistry Chemical Physics*, 15(8), p.2809.

144. Rand, M. and Roberts, J., 1968. Preparation and Properties of Thin Film Boron Nitride. *Journal of The Electrochemical Society*, 115(4), p.423.

145. Nigam, S. and Majumder, C., 2008. CO Oxidation by BN−Fullerene Cage: Effect of Impurity on the Chemical Reactivity. *ACS Nano*, 2(7), pp.1422-1428.

146. Huda, M. and Kleinman, L., 2006. Hydrogen adsorption and dissociation on small platinum clusters: An electronic structure density functional study. *Physical Review B*, 74(19).

147. Wasey, A., Chakrabarty, S., Das, G. and Majumder, C., 2013. h-BN Mono-layer on the Ni(111) Surface: A Potential Catalyst for Oxidation. *ACS Applied Materials & Interfaces*, 5(21), pp.10404-10408.

148. Gamo, Y., Nagashima, A., Wakabayashi, M., Terai, M. and Oshima, C., 1997. Atomic structure of mono-layer graphite formed on Ni(111). *Surface Science*, 374(1-3), pp.61-64.

149. Laskowski, R. and Blaha, P., 2010. Ab initiostudy ofh−BNnanomeshes on Ru(001), Rh(111), and Pt(111). *Physical Review B*, 81(7).

150. Gamo, Y., Nagashima, A., Wakabayashi, M., Terai, M. and Oshima, C., 1997. Atomic structure of mono-layer graphite formed on Ni(111). *Surface Science*, 374(1-3), pp.61-64.

151. Nagashima, A., Tejima, N., Gamou, Y., Kawai, T. and Oshima, C., 1995. Electronic Structure of Mono-layer Hexagonal Boron Nitride Physisorbed on Metal Surfaces. *Physical Review Letters*, 75(21), pp.3918-3921.

152. Rokuta, E., Hasegawa, Y., Suzuki, K., Gamou, Y., Oshima, C. and Nagashima, A., 1997. Phonon Dispersion of an Epitaxial Mono-layer Film of Hexagonal Boron Nitride on Ni(111). *Physical Review Letters*, 79(23), pp.4609-4612.

153. Laskowski, R. and Blaha, P., 2010. Ab initiostudy ofh−BNnanomeshes on Ru(001), Rh(111), and Pt(111). *Physical Review B*, 81(7).

154. Bosak, A., Serrano, J., Krisch, M., Watanabe, K., Taniguchi, T. and Kanda, H., 2006. Elasticity of hexagonal boron nitride: Inelastic x-ray scattering measurements. *Physical Review B*, 73(4).

155. Green, J., Bolland, T. and Bolland, J., 1976. Theoretical elastic behavior for hexagonal boron nitride. *The Journal of Chemical Physics*, 64(2), pp.656-662.

156. Hamdi, I. and Meskini, N., 2010. Ab initio study of the structural, elastic, vibrational and thermodynamic properties of the hexagonal boron nitride: Performance of LDA and GGA. *Physica B: Condensed Matter*, 405(13), pp.2785-2794.

157.   Lebedev, A., Lebedeva, I., Knizhnik, A. and Popov, A., 2016. Interlayer interaction and related properties of bilayer hexagonal boron nitride: ab initio study. *RSC Advances*, 6(8), pp.6423-6435.

158.   Weitz, R. and Yacoby, A., 2010. Graphene rests easy. *Nature Nanotechnology*, 5(10), pp.699-700.

159.   Lei, W., Portehault, D., Liu, D., Qin, S. and Chen, Y., 2013. Porous boron nitride nanosheets for effective water cleaning. *Nature Communications*, 4(1).

160.   Balmain, W., 1842. Bemerkungen über die Bildung von Verbindungen des Bors und Siliciums mit Stickstoff und gewissen Metallen. *Journal für Praktische Chemie*, 27(1), pp.422-430.

161.   Iwamoto, T., Kabuto, C. and Kira, M., 2000. The First Stable Cyclotrisilene [J. Am. Chem. Soc.1999,121, 886−887]. *Journal of the American Chemical Society*, 122(50), pp.12614-12614.

162.   Lipp, A., Schwetz, K. and Hunold, K., 1989. Hexagonal boron nitride: Fabrication, properties and applications. *Journal of the European Ceramic Society*, 5(1), pp.3-9.

163.   Novoselov, K., Jiang, D., Schedin, F., Booth, T., Khotkevich, V., Morozov, S. and Geim, A., 2005. Two-dimensional atomic crystals. *Proceedings of the National Academy of Sciences*, 102(30), pp.10451-10453.

164.   Dean, C., Young, A., Meric, I., Lee, C., Wang, L., Sorgenfrei, S., Watanabe, K., Taniguchi, T., Kim, P., Shepard, K. and Hone, J., 2010. Boron nitride substrates for high-quality graphene electronics. *Nature Nanotechnology*, 5(10), pp.722-726.

165.   Wang, L., Meric, I., Huang, P., Gao, Q., Gao, Y., Tran, H., Taniguchi, T., Watanabe, K., Campos, L., Muller, D., Guo, J., Kim, P., Hone, J., Shepard, K. and Dean, C., 2013. One-Dimensional Electrical Contact to a Two-Dimensional Material. *Science*, 342(6158), pp.614-617.

166.   Petrone, N., Chari, T., Meric, I., Wang, L., Shepard, K. and Hone, J., 2015. Flexible Graphene Field-Effect Transistors Encapsulated in Hexagonal Boron Nitride. *ACS Nano*, 9(9), pp.8953-8959.

167.   Xue, J., Sanchez-Yamagishi, J., Bulmash, D., Jacquod, P., Deshpande, A., Watanabe, K., Taniguchi, T., Jarillo-Herrero, P. and LeRoy, B., 2011. Scanning tunnelling microscopy and spectroscopy of ultra-flat graphene on hexagonal boron nitride. *Nature Materials*, 10(4), pp.282-285.

168.   Yao, Y., Lin, Z., Li, Z., Song, X., Moon, K. and Wong, C., 2012. Large-scale production of two-dimensional nanosheets. *Journal of Materials Chemistry*, 22(27), p.13494.

169.   Li, L., Chen, Y., Behan, G., Zhang, H., Petravic, M. and Glushenkov, A., 2011. Large-scale mechanical peeling of boron nitride nanosheets by low-energy ball milling. *Journal of Materials Chemistry*, 21(32), p.11862.

170.   Lin, Y., Williams, T., Cao, W., Elsayed-Ali, H. and Connell, J., 2010. Defect Functionalisation of Hexagonal Boron Nitride Nanosheets. *The Journal of Physical Chemistry C*, 114(41), pp.17434-17439.

171.   Huang, J., Yasuda, H. and Mori, H., 2004. HR-TEM and EELS Studies on the Amorphization of Hexagonal Boron Nitride Induced by Ball Milling. *Journal of the American Ceramic Society*, 83(2), pp.403-409.

172.   Streletskii, A., Permenov, D., Bokhonov, B., Kolbanev, I., Leonov, A., Berestetskaya, I. and Streletzky, K., 2009. Destruction, amorphization and

reactivity of nano-BN under ball milling. *Journal of Alloys and Compounds*, 483(1-2), pp.313-316.

173.   Coleman, J. and et al., e., 2011. ChemInform Abstract: Two-Dimensional Nanosheets Produced by Liquid Exfoliation of Layered Materials. *ChemInform*, 42(18), p.no-no.

174.   Zhao, G., Zhang, F., Wu, Y., Hao, X., Wang, Z. and Xu, X., 2015. One-Step Exfoliation and Hydroxylation of Boron Nitride Nanosheets with Enhanced Optical Limiting Performance. *Advanced Optical Materials*, 4(1), pp.141-146.

175.   Zeng, Z., Sun, T., Zhu, J., Huang, X., Yin, Z., Lu, G., Fan, Z., Yan, Q., Hng, H. and Zhang, H., 2012. An Effective Method for the Fabrication of Few-Layer-Thick Inorganic Nanosheets. *Angewandte Chemie International Edition*, 51(36), pp.9052-9056.

176.   Kovtyukhova, N., Wang, Y., Lv, R., Terrones, M., Crespi, V. and Mallouk, T., 2013. Reversible Intercalation of Hexagonal Boron Nitride with Brønsted Acids. *Journal of the American Chemical Society*, 135(22), pp.8372-8381.

177.   Du, M., Wu, Y. and Hao, X., 2013. A facile chemical exfoliation method to obtain large size boron nitride nanosheets. *CrystEngComm*, 15(9), p.1782.

178.   Li, X., Hao, X., Zhao, M., Wu, Y., Yang, J., Tian, Y. and Qian, G., 2013. Exfoliation of Hexagonal Boron Nitride by Molten Hydroxides. *Advanced Materials*, 25(15), pp.2200-2204.

179.   Lin, Y., Williams, T., Xu, T., Cao, W., Elsayed-Ali, H. and Connell, J., 2011. Aqueous Dispersions of Few-Layered and Mono-layered Hexagonal

Boron Nitride Nanosheets from Sonication-Assisted Hydrolysis: Critical Role of Water. *The Journal of Physical Chemistry C*, 115(6), pp.2679-2685.

180.   Han, W., Wu, L., Zhu, Y., Watanabe, K. and Taniguchi, T., 2008. Structure of chemically derived mono- and few-atomic-layer boron nitride sheets. *Applied Physics Letters*, 93(22), p.223103.

181.   Liu, Y., Xie, X. and Ye, X., 2013. Tuning the solubility of boron nitridenanosheets in organic solvents by using block copolymer as a "Janus" modifier. *Chem. Commun.*, 49(4), pp.388-390.

182.   Singhal, S., Kumar, V., Stalin, K., Choudhary, A., Teotia, S., Reddy, G., Mathur, R., Singh, S. and Pasricha, R., 2013. Gold-Nanoparticle-Decorated Boron Nitride Nanosheets: Structure and Optical Properties. *Particle & Particle Systems Characterisation*, 30(5), pp.445-452.

183.   Lin, Y., Williams, T. and Connell, J., 2009. Soluble, Exfoliated Hexagonal Boron Nitride Nanosheets. *The Journal of Physical Chemistry Letters*, 1(1), pp.277-283.

184.   Sainsbury, T., Satti, A., May, P., Wang, Z., McGovern, I., Gun'ko, Y. and Coleman, J., 2012. Oxygen Radical Functionalisation of Boron Nitride Nanosheets. *Journal of the American Chemical Society*, 134(45), pp.18758-18771.

185.   Jin, C., Lin, F., Suenaga, K. and Iijima, S., 2009. Fabrication of a Freestanding Boron Nitride Single Layer and Its Defect Assignments. *Physical Review Letters*, 102(19).

186.   Medical Physics, 2000. Multimedia in Online Journals via EPAPS. 27(1), pp.270-270.

187.   Paffett, M., Simonson, R., Papin, P. and Paine, R., 1990. Borazine adsorption and decomposition at Pt(111) and Ru(001) surfaces. *Surface Science*, 232(3), pp.286-296.

188.   Pierson, H., 1975. Boron Nitride Composites By Chemical Vapor Deposition. *Journal of Composite Materials*, 9(3), pp.228-240.

189.   Rozenberg, A., Sinenko, Y. and Chukanov, N., 1993. Regularities of pyrolytic boron nitride coating formation on a graphite matrix. *Journal of Materials Science*, 28(20), pp.5528-5533.

190.   Middleman, S., 1993. The role of gas-phase reactions in boron nitride growth by chemical vapor deposition. *Materials Science and Engineering: A*, 163(1), pp.135-140.

191.   Adams, A., 1981. Characterisation of Films Formed by Pyrolysis of Borazine. *Journal of The Electrochemical Society*, 128(6), p.1378.

192.   Auwärter, W., Suter, H., Sachdev, H. and Greber, T., 2004. Synthesis of One Mono-layer of Hexagonal Boron Nitride on Ni(111) from B-Trichloroborazine (ClBNH)3. *Chemistry of Materials*, 16(2), pp.343-345.

193.   Müller, F., Stöwe, K. and Sachdev, H., 2005. Symmetry versus Commensurability: Epitaxial Growth of Hexagonal Boron Nitride on Pt(111) From B-Trichloroborazine (ClBNH)3. *Chemistry of Materials*, 17(13), pp.3464-3467.

194.   Constant, G. and Feurer, R., 1981. Preparation and Characterisation of thin protective films in silica tubes by thermal decomposition of hexachloroborazine. *Journal of the Less Common Metals*, 82, pp.113-118.

195.	Paffett, M., Simonson, R., Papin, P. and Paine, R., 1990. Borazine adsorption and decomposition at Pt(111) and Ru(001) surfaces. *Surface Science*, 232(3), pp.286-296.

196.	Archer, N., 1979. Chemical vapour deposition. *Physics in Technology*, 10(4), pp.152-161.

197.	Corso, M., Auwaerter, W., Muntwiler, M., Tamai, A., Greber, T. and Osterwalder, J., 2004. Boron Nitride Nanomesh. *ChemInform*, 35(14).

198.	Auwärter, W., Kreutz, T., Greber, T. and Osterwalder, J., 1999. XPD and STM investigation of hexagonal boron nitride on Ni(111). *Surface Science*, 429(1-3), pp.229-236.

199.	Huda, M. and Kleinman, L., 2006. h-BNmono-layer adsorption on theNi(111)surface: A density functional study. *Physical Review B*, 74(7).

200.	Ćavar, E., Westerström, R., Mikkelsen, A., Lundgren, E., Vinogradov, A., Ng, M., Preobrajenski, A., Zakharov, A. and Mårtensson, N., 2008. A single h-BN layer on Pt(111). *Surface Science*, 602(9), pp.1722-1726.

201.	Goriachko, A., He, Knapp, M., Over, H., Corso, M., Brugger, T., Berner, S., Osterwalder, J. and Greber, T., 2007. Self-Assembly of a Hexagonal Boron Nitride Nanomesh on Ru(0001). *Langmuir*, 23(6), pp.2928-2931.

202.	Preobrajenski, A., Vinogradov, A. and Mårtensson, N., 2005. Mono-layer of h-BN chemisorbed on Cu(111) and Ni(111): The role of the transition metal 3d states. *Surface Science*, 582(1-3), pp.21-30.

203.	Preobrajenski, A., Vinogradov, A., Ng, M., Ćavar, E., Westerström, R., Mikkelsen, A., Lundgren, E. and Mårtensson, N., 2007. Influence of chemical interaction at the lattice-mismatchedh−BN∕Rh(111)andh−BN∕Pt(111)interfaces on the overlayer morphology. *Physical Review B*, 75(24).

204.   Morscher, M., Corso, M., Greber, T. and Osterwalder, J., 2006. Formation of single layer h-BN on Pd(111). *Surface Science*, 600(16), pp.3280-3284.

205.   Corso, M., Greber, T. and Osterwalder, J., 2005. h-BN on Pd(110): a tunable system for self-assembled nanostructures?. *Surface Science*, 577(2-3), pp.L78-L84.

206.   Vinogradov, N., Zakharov, A., Ng, M., Mikkelsen, A., Lundgren, E., Mårtensson, N. and Preobrajenski, A., 2012. One-Dimensional Corrugation of the h-BN Mono-layer on Fe(110). *Langmuir*, 28(3), pp.1775-1781.

207.   Allan, M., Berner, S., Corso, M., Greber, T. and Osterwalder, J., 2007. Tunable self-assembly of one-dimensional nanostructures with orthogonal directions. *Nanoscale Research Letters*, 2(2), pp.94-99.

208.   Müller, F., Hüfner, S. and Sachdev, H., 2008. One-dimensional structure of boron nitride on chromium (110) – a study of the growth of boron nitride by chemical vapour deposition of borazine. *Surface Science*, 602(22), pp.3467-3476.

209.   Sutter, P., Lahiri, J., Albrecht, P. and Sutter, E., 2011. Chemical Vapor Deposition and Etching of High-Quality Mono-layer Hexagonal Boron Nitride Films. *ACS Nano*, 5(9), pp.7303-7309.

210.   Guerra, V., Wan, C. and McNally, T., 2019. Thermal conductivity of 2D nano-structured boron nitride (BN) and its composites with polymers. *Progress in Materials Science*, 100, pp.170-186.

211.   Shi, Y., Hamsen, C., Jia, X., Kim, K., Reina, A., Hofmann, M., Hsu, A., Zhang, K., Li, H., Juang, Z., Dresselhaus, M., Li, L. and Kong, J., 2010.

Synthesis of Few-Layer Hexagonal Boron Nitride Thin Film by Chemical Vapor Deposition. *Nano Letters*, 10(10), pp.4134-4139.

212.   Kim, K., Hsu, A., Jia, X., Kim, S., Shi, Y., Hofmann, M., Nezich, D., Rodriguez-Nieva, J., Dresselhaus, M., Palacios, T. and Kong, J., 2011. Synthesis of Mono-layer Hexagonal Boron Nitride on Cu Foil Using Chemical Vapor Deposition. *Nano Letters*, 12(1), pp.161-166.

213.   Kim, G., Jang, A., Jeong, H., Lee, Z., Kang, D. and Shin, H., 2013. Growth of High-Crystalline, Single-Layer Hexagonal Boron Nitride on Recyclable Platinum Foil. *Nano Letters*, 13(4), pp.1834-1839.

214.   Zhang, Z., Liu, Y., Yang, Y. and Yakobson, B., 2016. Growth Mechanism and Morphology of Hexagonal Boron Nitride. *Nano Letters*, 16(2), pp.1398-1403.

215.   Bae, S., Kim, H., Lee, Y., Xu, X., Park, J.S., Zheng, Y., Balakrishnan, J., Lei, T., Kim, H.R., Song, Y.I. and Kim, Y.J., 2010. Roll-to-roll production of 30-inch graphene films for transparent electrodes. *Nature nanotechnology*, *5*(8), pp.574-578.

216.   Jin, C., Lin, F., Suenaga, K. and Iijima, S., 2009. Fabrication of a Freestanding Boron Nitride Single Layer and Its Defect Assignments. *Physical Review Letters*, 102(19).195505.

217.   Wang, H., Zhang, X., Liu, H., Yin, Z., Meng, J., Xia, J., Meng, X., Wu, J. and You, J., 2015. Synthesis of Large-Sized Single-Crystal Hexagonal Boron Nitride Domains on Nickel Foils by Ion Beam Sputtering Deposition. *Advanced Materials*, 27(48), pp.8109-8115.

218. Han, W., Yu, H. and Liu, Z., 2011. Convert graphene sheets to boron nitride and boron nitride–carbon sheets via a carbon-substitution reaction. *Applied Physics Letters*, 98(20), p.203112.

219. Lin, T., Su, C., Zhang, X., Zhang, W., Lee, Y., Chu, C., Lin, H., Chang, M., Chen, F. and Li, L., 2012. Converting Graphene Oxide Mono-layers into Boron Carbonitride Nanosheets by Substitutional Doping. *Small*, 8(9), pp.1384-1391.

220. Gong, Y., Shi, G., Zhang, Z., Zhou, W., Jung, J., Gao, W., Ma, L., Yang, Y., Yang, S., You, G., Vajtai, R., Xu, Q., MacDonald, A., Yakobson, B., Lou, J., Liu, Z. and Ajayan, P., 2014. Direct chemical conversion of graphene to boron- and nitrogen- and carbon-containing atomic layers. *Nature Communications*, 5(1).

221. Han, W., Bando, Y., Kurashima, K. and Sato, T., 1998. Synthesis of boron nitride nanotubes from carbon nanotubes by a substitution reaction. *Applied Physics Letters*, 73(21), pp.3085-3087.

222. Wang, X., Weng, Q., Wang, X., Li, X., Zhang, J., Liu, F., Jiang, X., Guo, H., Xu, N., Golberg, D. and Bando, Y., 2014. Biomass-Directed Synthesis of 20 g High-Quality Boron Nitride Nanosheets for Thermoconductive Polymeric Composites. *ACS Nano*, 8(9), pp.9081-9088.

223. Kim, G., Lim, H., Ma, K., Jang, A., Ryu, G., Jung, M., Shin, H., Lee, Z. and Shin, H., 2015. Catalytic Conversion of Hexagonal Boron Nitride to Graphene for In-Plane Heterostructures. *Nano Letters*, 15(7), pp.4769-4775.

224. Nag, A., Raidongia, K., Hembram, K., Datta, R., Waghmare, U. and Rao, C., 2010. Graphene Analogues of BN: Novel Synthesis and Properties. *ACS Nano*, 4(3), pp.1539-1544.

225.   Wang, L., Sun, C., Xu, L. and Qian, Y., 2011. Convenient synthesis and applications of gram scale boron nitride nanosheets. *Catalysis Science & Technology*, 1(7), p.1119.

226.   Lin, T., Su, C., Zhang, X., Zhang, W., Lee, Y., Chu, C., Lin, H., Chang, M., Chen, F. and Li, L., 2012. Converting Graphene Oxide Mono-layers into Boron Carbonitride Nanosheets by Substitutional Doping. *Small*, 8(9), pp.1384-1391.

227.   Hallett, J. (2002). Climate change 2001: The scientific basis. Edited by J. T. Houghton, Y. Ding, D. J. Griggs, N. Noguer, P. J. van der Linden, D. Xiaosu, K. Maskell and C. A. Johnson. Contribution of Working Group I to the Third Assessment Report of the Intergovernmental Panel on Climate Change, Cambridge University Press, Cambridge. 2001. 881 pp. ISBN 0521 01495 6. Quarterly Journal of the Royal Meteorological Society, 128(581), pp.1038-1039.

228.   Cobb, N. and Etzel, R.A., 1991. Unintentional carbon monoxide— Related deaths in the United States, 1979 through 1988. Jama, 266(5), pp.659-663.

229.   Meredith, C.T., 1988. Correction: Comroe and Dripps revisited. Brit. Med. J, 296, p.110.

230.   Runyan, C.W., Johnson, R.M., Yang, J., Waller, A.E., Perkis, D., Marshall, S.W., Coyne-Beasley, T. and McGee, K.S., 2005. Risk and protective factors for fires, burns, and carbon monoxide poisoning in US households. American journal of preventive medicine, 28(1), pp.102-108.

231.   Varon, J., Marik, P.E., Fromm Jr, R.E. and Gueler, A., 1999. Carbon monoxide poisoning: a review for clinicians. The Journal of emergency medicine, 17(1), pp.87-93.

232.   de Wet, S.D. and du Toit, A., 2000. The challenge of implementing a records management system at the National Electricity Regulator in South Africa. *Records management journal*.

233.   Yoshida, T. and Shevkoplyas, S.S., 2010. Anaerobic storage of red blood cells. Blood Transfusion, 8(4), p.220.

234.   Penney, D.G., 2000. 18 Chronic Carbon Monoxide Poisoning. Carbon monoxide toxicity, p.393.

235.   Fine, G.F., Cavanagh, L.M., Afonja, A. and Binions, R., 2010. Metal oxide semi-conductor gas sensors in environmental monitoring. sensors, 10(6), pp.5469-5502.

236.   Denman, K.L., Brasseur, G., Chidthaisong, A., Ciais, P., Cox, P.M., Dickinson, R.E. and Hauglustaine, D., 2007. C. 20 Heinze, E. Holland, D. Jacob, U. Lohmann, S Ramachandran, PL da Silva Dias, SC Wofsy, and X. Zhang,: Couplings Between Changes in the Climate System and Biogeochemistry. In: Climate Change.

237.   Lemery, J. and Auerbach, P., 2017. Enviromedics: the impact of climate change on human health. Rowman & Littlefield.

238.   Hunter, C. and Crecelius, H., 1938. Hydrogen Sulphide Studies. Journal of Bacteriology, 35(2), pp.185-196.

239.   Orofeo, C., Suzuki, S., Kageshima, H. and Hibino, H., 2013. Growth and low-energy electron microscopy Characterisation of mono-layer hexagonal boron nitride on epitaxial cobalt. *Nano Research*, 6(5), pp.335-347.

240.   Wu, Q., Park, J., Park, S., Jung, S., Suh, H., Park, N., Wongwiriyapan, W., Lee, S., Lee, Y. and Song, Y., 2015. Single Crystalline Film of Hexagonal Boron Nitride Atomic Mono-layer by Controlling Nucleation Seeds and Domains. *Scientific Reports*, 5(1).

241.   Gilbert, B., Zhang, H., Huang, F., Banfield, J., Ren, Y., Haskel, D., Lang, J., Srajer, G., Jürgensen, A. and Waychunas, G. 2004. Analysis and simulation of the structure of nanoparticles that undergo a surface-driven structural transformation. *The Journal of Chemical Physics*, 120(24), pp.11785-11795.

242.   Smith, W., Forester, T., Todorov, I. & Leslie, M. 2009. The DL poly 2 user manual, CCLRC, Daresbury Laboratory, Daresbury, Warrington WA4 4AD, England, 2.

243.   Verlet, L. 1968. Computer "Experiments" on Classical Fluids. II. Equilibrium Correlation Functions. *Physical Review*, 165(1), pp.201-214.

244.   Moon, W.H. and Hwang, H.J., 2003. Structural and thermodynamic properties of GaN: a molecular dynamics simulation. Physics Letters A, 315(3-4). pp.319-324.

245.   Goumri-Said, S., Kanoun, M.B., Merad, A.E., Merad, G. and Aourag, H., 2004. Prediction of structural and thermodynamic properties of zinc-blende AlN: molecular dynamics simulation. Chemical Physics, 302(1-3). pp.135-141.

246.   Verlet, L. 1968. Computer "Experiments" on Classical Fluids. II. Equilibrium Correlation Functions. *Physical Review*, 165(1), pp.201-214.

247.   Allinger, N., 1977. Conformational analysis. 130. MM2. A hydrocarbon force field utilizing V1 and V2 torsional terms. Journal of the American Chemical Society, 99(25), pp.8127-8134.

248.   Allinger, N., Yuh, Y. and Lii, J., 1989. Molecular mechanics. The MM3 force field for hydrocarbons. 1. Journal of the American Chemical Society, 111(23), pp.8551-8566.

249.   Lii, J. and Allinger, N., 1989. Molecular mechanics. The MM3 force field for hydrocarbons. 2. Vibrational frequencies and thermodynamics. Journal of the American Chemical Society, 111(23), pp.8566-8575.

250.   Lii, J. and Allinger, N., 1989. Molecular mechanics. The MM3 force field for hydrocarbons. 3. The van der Waals' potentials and crystal data for aliphatic and aromatic hydrocarbons. Journal of the American Chemical Society, 111(23), pp.8576-8582.

251.   Abell, G., 1985. Empirical chemical pseudopotential theory of molecular and metallic bonding. Physical Review B, 31(10), pp.6184-6196.

252.   Tersoff, J., 1988. New empirical approach for the structure and energy of covalent systems. Physical Review B, 37(12), pp.6991-7000.

253.   Tersoff, J., 1988. Empirical Interatomic Potential for Carbon, with Applications to Amorphous Carbon. Physical Review Letters, 61(25), pp.2879-2882.

254. Nordlund, K., Keinonen, J. and Mattila, T., 1996. Formation of Ion Irradiation Induced Small-Scale Defects on Graphite Surfaces. Physical Review Letters, 77(4), pp.699-702.

255. Erhart, P. and Albe, K., 2005. Analytical potential for atomistic simulations of silicon, carbon, and silicon carbide. Physical Review B, 71(3). p.035211.

256. Lindsay, L. and Broido, D.A., 2010. Optimised Tersoff and Brenner empirical potential parameters for lattice dynamics and phonon thermal transport in carbon nanotubes and graphene. Physical Review B, 81(20). p.205441.

257. Agrawal, P.M., Raff, L.M. and Komanduri, R., 2005. Monte Carlo simulations of void-nucleated melting of silicon via modification in the Tersoff potential parameters. Physical Review B, 72(12). p.125206.

258. Smith, R., 1992. A semi-empirical many-body interatomic potential for modelling dynamical processes in gallium arsenide. Nuclear Instruments and Methods in Physics Research Section B: Beam Interactions with Materials and Atoms, 67(1-4). pp.335-339.

259. Sayed, M., Jefferson, J.H., Walker, A.B. and Cullis, A.G., 1995. Molecular dynamics simulations of implantation damage and recovery in semiconductors. Nuclear Instruments and Methods in Physics Research Section B: Beam Interactions with Materials and Atoms, 102(1-4). pp.218-222.

260.   Nordlund, K., Nord, J., Frantz, J. and Keinonen, J., 2000. Strain-induced Kirkendall mixing at semiconductor interfaces. Computational materials science, 18(3-4). pp.283-294.

261.   Powell, D., Migliorato, M.A. and Cullis, A.G., 2007. Optimised Tersoff potential parameters for tetrahedrally bonded III-V semiconductors. Physical Review B, 75(11). p.115202.

262.   Sevik, C., Kinaci, A., Haskins, J.B. and Çağın, T., 2011. Characterisation of thermal transport in low-dimensional boron nitride nanostructures. Physical Review B, 84(8). p.085409.

263.   Mortazavi, B., Cuniberti, G. and Rabczuk, T., 2015. Mechanical properties and thermal conductivity of graphitic carbon nitride: A molecular dynamics study. Computational Materials Science, 99. pp.285-289.

264.   Srivastava, P. and Sen, P., 2012. Density functional study of structural defects in h-BNC2 sheets. *Journal of Physics: Condensed Matter*, *25*(2), p.025304.

265.   Slotman, G.J. and Fasolino, A., 2012. Structure, stability and defects of single layer hexagonal BN in comparison to graphene. Journal of Physics: Condensed Matter, 25(4), p.045009.

266.   Shi, Y., Hamsen, C., Jia, X., Kim, K., Reina, A., Hofmann, M., Hsu, A., Zhang, K., Li, H., Juang, Z., Dresselhaus, M., Li, L. and Kong, J., 2010. Synthesis of Few-Layer Hexagonal Boron Nitride Thin Film by Chemical Vapor Deposition. Nano Letters, 10(10), pp.4134-4139.

267.   Nag, A., Raidongia, K., Hembram, K.P., Datta, R., Waghmare, U.V. and Rao, C.N.R., 2010. Graphene analogues of BN: novel synthesis and properties. ACS nano, 4(3), pp.1539-1544.

268.   Lee, J.U., Kim, M. and Cheong, H., 2015. Raman spectroscopic studies on two-dimensional materials. Applied Microscopy, 45(3), pp.126-130.

269.   Kiran, M.S.R.N., Raidongia, K., Ramamurty, U. and Rao, C.N.R., 2011. Improved mechanical properties of polymer nanocomposites incorporating graphene-like BN: Dependence on the number of BN layers. Scripta Materialia, 64(6), pp.592-595.

270.   Besisa, D.H., Hagras, M.A., Ewais, E.M., Ahmed, Y.M., Zaki, Z.I. and Ahmed, A., 2016. Low temperature synthesis of nano-crystalline h-boron nitride from boric acid/urea precursors. J. Ceram. Process. Res., 17(12), pp.1219-1225.

271.   Zhang, Y., Choi, J.R. and Park, S.J., 2017. Thermal conductivity and thermo-physical properties of nanodiamond-attached exfoliated hexagonal boron nitride/epoxy nanocomposites for microelectronics. *Composites Part A: Applied Science and Manufacturing*, *101*, pp.227-236.

272.   Sajjad, M. and Feng, P., 2014. Study the gas sensing properties of boron nitride nanosheets. *Materials Research Bulletin*, *49*, pp.35-38.

273.   Sharma, R., Bisen, D.P., Shukla, U. and Sharma, B.G., 2012. X-ray diffraction: a powerful method of characterizing nanomaterials. Recent research in science and technology, 4(8).

274.   Devi, B.R., Raveendran, R. and Vaidyan, A.V., 2007. Synthesis and Characterisation of Mn 2+-doped ZnS nanoparticles. Pramana, 68(4), pp.679-687.

275.   Pankove, J.I., 1971. Optical processes in semiconductors Prentice-Hall. New Jersey, 92.

276.   McComiskey, K.P., 2019. The Production, Characterisation, Stabilization and Isolation of Azole Anti-Fungal Nanoparticles (Doctoral dissertation, University of Dublin, Ireland

277.   Harding, S., 1999. Protein Hydrodynamics. Protein: a comprehensive treatise. Greenwich, CT: JAI Press, (2), pp. 271–305.

278.   Stetefeld, J., McKenna, S.A. and Patel, T.R., 2016. Dynamic light scattering: a practical guide and applications in biomedical sciences. Biophysical reviews, 8(4), pp.409-427.

279.   Egerton, R.F., 2005. Physical principles of electron microscopy (Vol. 56). New York: Springer.

280.   Lee, J.U., Kim, M. and Cheong, H., 2015. Raman spectroscopic studies on two-dimensional materials. Applied Microscopy, 45(3), pp.126-130.

281.   Hwang, N. and Barron, A.R., 2011. BET surface area analysis of nanoparticles. The Connexions project, pp.1-11.

282.   Thomas, S., Ajith, K.M. and Valsakumar, M.C., 2017. Empirical potential influence and effect of temperature on the mechanical properties of pristine and defective hexagonal boron nitride. *Materials Research Express*, *4*(6), p.065005.

283.   Verma, V., Jindal, V.K. and Dharamvir, K., 2007. Elastic moduli of a boron nitride nanotube. *Nanotechnology*, *18*(43), p.435711.

284. Srivastava, P. and Sen, P., 2012. Density functional study of structural defects in h-BNC2 sheets. *Journal of Physics: Condensed Matter*, *25*(2), p.025304.

285. Fasolino, A., Los, J.H. and Katsnelson, M.I., 2007. Intrinsic ripples in graphene. *Nature materials*, *6*(11), pp.858-861.

286. Thomas, S., Ajith, K., Chandra, S. and Valsakumar, M., 2015. Temperature dependent structural properties and bending rigidity of pristine and defective hexagonal boron nitride. *Journal of Physics: Condensed Matter*, 27(31), p.315302.

287. Yuan, J. and Liew, K.M., 2014. Structure stability and high-temperature distortion resistance of trilayer complexes formed from graphenes and boron nitride nanosheets. *Physical Chemistry Chemical Physics*, *16*(1), pp.88-94.

288. Barnard, A.S., Snook, I.K. and Russo, S.P., 2007. Bonding and structure in B x N y nanotubes (x, y= 1, 2). *Journal of Materials Chemistry*, *17*(28), pp.2892-2898.

289. Liu, Y., Bhowmick, S. and Yakobson, B.I., 2011. BN white graphene with "colorful" edges: The energies and morphology. *Nano letters*, *11*(8), pp.3113-3116.

290. Liu, Z.Q., Dong, J. and Ding, F., 2019. The geometry of hexagonal boron nitride clusters in the initial stages of chemical vapor deposition growth on a Cu (111) surface. *Nanoscale*, *11*(28), pp.13366-13376.

291.   Liu, Z.Q., Dong, J. and Ding, F., 2019. The geometry of hexagonal boron nitride clusters in the initial stages of chemical vapor deposition growth on a Cu (111) surface. *Nanoscale*, *11*(28), pp.13366-13376.

292.   Huang, B., Lee, H., Gu, B.L., Liu, F. and Duan, W., 2012. Edge stability of boron nitride nanoribbons and its application in designing hybrid BNC structures. *Nano Research*, *5*(1), pp.62-72.

293.   Zhang, Z., Liu, Y., Yang, Y. and Yakobson, B.I., 2016. Growth mechanism and morphology of hexagonal boron nitride. *Nano letters*, *16*(2), pp.1398-1403.

294.   Tay, R.Y., Griep, M.H., Mallick, G., Tsang, S.H., Singh, R.S., Tumlin, T., Teo, E.H.T. and Karna, S.P., 2014. Growth of large single-crystalline two-dimensional boron nitride hexagons on electropolished copper. *Nano letters*, *14*(2), pp.839-846.

295.   Paszkowicz, W., Pelka, J.B., Knapp, M., Szyszko, T. and Podsiadlo, S.J.A.P.A., 2002. Lattice parameters and anisotropic thermal expansion of hexagonal boron nitride in the 10–297.5 K temperature range. *Applied Physics A*, *75*(3), pp.431-435.

296.   Albe, K., Möller, W. and Heinig, K.H., 1997. Computer simulation and boron nitride. *Radiation Effects and Defects in Solids*, *141*(1-4), pp.85-97.

297.   Alem, N., Erni, R., Kisielowski, C., Rossell, M.D., Gannett, W. and Zettl, A.J.P.R.B., 2009. Atomically thin hexagonal boron nitride probed by ultrahigh-resolution transmission electron microscopy. Physical review B, 80(15), p.155425.

298. Huang, J.Y., Chen, S., Wang, Z.Q., Kempa, K., Wang, Y.M., Jo, S.H., Chen, G., Dresselhaus, M.S. and Ren, Z.F., 2006. Superplastic carbon nanotubes. *Nature*, *439*(7074), pp.281-281.

299. Tang, C., Guo, W. and Chen, C., 2009. Molecular dynamics simulation of tensile elongation of carbon nanotubes: temperature and size effects. *Physical Review B*, *79*(15), p.155436.

300. Zhang, Y.Y. and Gu, Y., 2013. Mechanical properties of graphene: Effects of layer number, temperature and isotope. *Computational Materials Science*, *71*, pp.197-200.

301. Hopfield, J.J. and Herz, A.V., 1995. Rapid local synchronization of action potentials: Toward computation with coupled integrate-and-fire neurons. *Proceedings of the National Academy of Sciences*, *92*(15), pp.6655-6662.

302. Khordad, R. and Sedehi, H.R., 2017. Application of different entropies to study of bound magnetopolaron in an asymmetric quantum dot. *Indian Journal of Physics*, *91*(7), pp.825-831.

303. Thomas, S., Ajith, K., Chandra, S. and Valsakumar, M., 2015. Temperature dependent structural properties and bending rigidity of pristine and defective hexagonal boron nitride. *Journal of Physics: Condensed Matter*, 27(31), p.315302.

304. Sevik, C., 2014. Assessment on lattice thermal properties of two-dimensional honeycomb structures: Graphene, h-BN, h-MoS 2, and h-MoSe 2. *Physical Review B*, *89*(3), p.035422.

305.   Qian, G.X., Martin, R.M. and Chadi, D.J., 1988. First-principles study of the atomic reconstructions and energies of Ga-and As-stabilised GaAs (100) surfaces. *Physical Review B*, *38*(11), p.7649.

306.   Okada, S., 2009. Atomic configurations and energetics of vacancies in hexagonal boron nitride: First-principles total-energy calculations. *Physical Review B, 80*(16), p.161404.

307.   Besisa, D.H., Hagras, M.A., Ewais, E.M., Ahmed, Y.M., Zaki, Z.I. and Ahmed, A., 2016. Low temperature synthesis of nano-crystalline h-boron nitride from boric acid/urea precursors. *J. Ceram. Process. Res.*, *17*(12), pp.1219-1225.

308.   Gorbachev, R.V., Riaz, I., Nair, R.R., Jalil, R., Britnell, L., Belle, B.D., Hill, E.W., Novoselov, K.S., Watanabe, K., Taniguchi, T. and Geim, A.K., 2011. Hunting for mono-layer boron nitride: optical and Raman signatures. *Small*, *7*(4), pp.465-468.

309.   Cao, L., Emami, S. and Lafdi, K., 2014. Large-scale exfoliation of hexagonal boron nitride nanosheets in liquid phase. *Materials Express*, *4*(2), pp.165-171.

310.   Vilcarromero, J., Carreño, M.N.P. and Pereyra, I., 2000. Mechanical properties of boron nitride thin films obtained by RF-PECVD at low temperatures. *Thin Solid Films*, *373*(1-2), pp.273-276.

311.   Watanabe, K., Taniguchi, T. and Kanda, H., 2004. Direct-bandgap properties and evidence for ultraviolet lasing of hexagonal boron nitride single crystal. *Nature Materials*, 3(6), pp.404-409.

312.   Blase, X., Rubio, A., Louie, S.G. and Cohen, M.L., 1994. Stability and band gap constancy of boron nitride nanotubes. EPL (Europhysics Letters), 28(5), p.335.

313.   Liu, X., Ma, T., Pinna, N. and Zhang, J., 2017. Two-Dimensional Nanostructured Materials for Gas Sensing. *Advanced Functional Materials*, 27(37), p.1702168.

314.   Zhang, K., Feng, Y., Wang, F., Yang, Z. and Wang, J., 2017. Two dimensional hexagonal boron nitride (2D-hBN): synthesis, properties and applications. *Journal of Materials Chemistry C*, 5(46), pp.11992-12022.

315.   Li, X., Shan, J., Zhang, W., Su, S., Yuwen, L. and Wang, L., 2016. Recent Advances in Synthesis and Biomedical Applications of Two-Dimensional Transition Metal Dichalcogenide Nanosheets. *Small*, 13(5), p.1602660.

316.   Yin, J., Li, J., Hang, Y., Yu, J., Tai, G., Li, X., Zhang, Z. and Guo, W., 2016. Boron Nitride Nanostructures: Fabrication, Functionalisation and Applications. *Small*, 12(22), pp.2942-2968.

317.   Azevedo, S., Kaschny, J., de Castilho, C. and de Brito Mota, F., 2009. Electronic structure of defects in a boron nitride mono-layer. *The European Physical Journal B*, 67(4), pp.507-512.

318.   Shahabuddin, S., Shah, S.N.A., Sabri, M.F.M. and Pandey, A.K., 2021, March. Influence of SDBS Surfactant on Stability, Thermal Conductivity and Viscosity of h-BN/EG Based Nanofluids. In *IOP Conference Series: Materials Science and Engineering* (Vol. 1127, No. 1, p. 012014). IOP Publishing.

319.   Korada, V.S. and Hamid, N.H.B., 2017. Engineering Applications of Nanotechnology.

320.   Peigney, A., Laurent, C., Flahaut, E., Bacsa, R. and Rousset, A., 2001. Specific surface area of carbon nanotubes and bundles of carbon nanotubes. *Carbon*, 39(4), pp.507-514.

321.   Gorbachev, R.V., Riaz, I., Nair, R.R., Jalil, R., Britnell, L., Belle, B.D., Hill, E.W., Novoselov, K.S., Watanabe, K., Taniguchi, T. and Geim, A.K., 2011. Hunting for mono-layer boron nitride: optical and Raman signatures. *Small*, *7*(4), pp.465-468.

322.   Stenger, I., Schué, L., Boukhicha, M., Berini, B., Plaçais, B., Loiseau, A. and Barjon, J., 2017. Low frequency Raman spectroscopy of few-atomic-layer thick hBN crystals. *2D Materials*, *4*(3), p.031003.

323.   Zhou, H., Zhu, J., Liu, Z., Yan, Z., Fan, X., Lin, J., Wang, G., Yan, Q., Yu, T., Ajayan, P. and Tour, J., 2014. High thermal conductivity of suspended few-layer hexagonal boron nitride sheets. *Nano Research*, 7(8), pp.1232-1240.

324.   Reich, S., Ferrari, A., Arenal, R., Loiseau, A., Bello, I. and Robertson, J., 2005. Resonant Raman scattering in cubic and hexagonal boron nitride. *Physical Review B*, 71(20).

325.   Kibasomba, P.M., Dhlamini, S., Maaza, M., Liu, C.P., Rashad, M.M., Rayan, D.A. and Mwakikunga, B.W., 2018. Strain and grain size of TiO2 nanoparticles from TEM, Raman spectroscopy and XRD: The revisiting of the Williamson-Hall plot method. Results in Physics, 9, pp.628-635.

326.   Shahabuddin, S., Khanam, R., Khalid, M., Sarih, N.M., Ching, J.J., Mohamad, S. and Saidur, R., 2018. Synthesis of 2D boron nitride doped polyaniline hybrid nanocomposites for photocatalytic degradation of

carcinogenic dyes from aqueous solution. Arabian journal of chemistry, 11(6), pp.1000-1016.

327.   Kınacı, A., Haskins, J.B., Sevik, C. and Çağın, T., 2012. Thermal conductivity of BN-C nanostructures. Physical Review B, 86(11), p.115410.

328.   Saasa, V., Malwela, T., Beukes, M., Mokgotho, M., Liu, C.P. and Mwakikunga, B., 2018. Sensing technologies for detection of acetone in human breath for diabetes diagnosis and monitoring. *Diagnostics*, *8*(1), p.12.

329.   Cao, S. and Chen, H., 2017. Nanorods assembled hierarchical urchin-like WO3 nanostructures: Hydrothermal synthesis, Characterisation, and their gas sensing properties. *Journal of Alloys and Compounds*, *702*, pp.644-648.

330.   Morrison, S.R., 1981. Semiconductor gas sensors. Sensors and Actuators, 2, pp.329-341.

331.   Maekawa, T., Tamaki, J., Miura, N. and Yamazoe, N., 1991. Sensing behavior of CuO-loaded SnO2 element for H2S detection. chemistry Letters, 20(4), pp.575-578.

332.   Hao, Q., Li, L., Yin, X., Liu, S., Li, Q. and Wang, T., 2011. Anomalous conductivity-type transition sensing behaviors of n-type porous α-Fe2O3 nanostructures toward H2S. Materials Science and Engineering: B, 176(7), pp.600-605.

333.   Ansari, M.O., Khan, M.M., Ansari, S.A., Amal, I., Lee, J. and Cho, M.H., 2014. Enhanced thermoelectric performance and ammonia sensing properties of sulfonated polyaniline/graphene thin films. *Materials Letters*, *114*, pp.159-162.

334.   Gaikwad, G., Patil, P., Patil, D. and Naik, J., 2017. Synthesis and evaluation of gas sensing properties of PANI based graphene oxide nanocomposites. Materials Science and Engineering: B, 218, pp.14-22.

335.   Pankove, J.I., 1975. Optical processes in semiconductors. Courier Corporation.

336.   Makuła, P., Pacia, M. and Macyk, W., 2018. How to correctly determine the band gap energy of modified semiconductor photocatalysts based on UV–Vis spectra. The journal of physical chemistry letters, 9(23), pp.6814-6817.

337.   Levitsky, I.A., 2015. Porous silicon structures as optical gas sensors. Sensors, 15(8), pp.19968-19991.

338.   Kaur, Kalwinder. 2019. Electrochemical gas sensors. AZosensors, viewed 13 September 2022, https://www.azosensors.com/article.aspx?articleID=235

339.   Dutta, A., 2017. Fourier transform infrared spectroscopy. Spectroscopic methods for nanomaterials characterization, pp.73-93.

340.   Yang, B., Guo, W., Liang, W., Zhou, Y. and Zhu, X., 2022. Design and evaluation of a miniature milk quality detection system based on UV/Vis spectroscopy. Journal of Food Composition and Analysis, 106, p.104341.

341.   Long, D.A. and Long, D.A., 2002. The Raman effect: a unified treatment of the theory of Raman scattering by molecules (Vol. 8, pp. 31-48). Chichester: Wiley.

342.   Singh, R. and Riess, F., 1998. Sir CV Raman and the story of the Nobel Prize. Current Science, 75(9), pp.965-971.
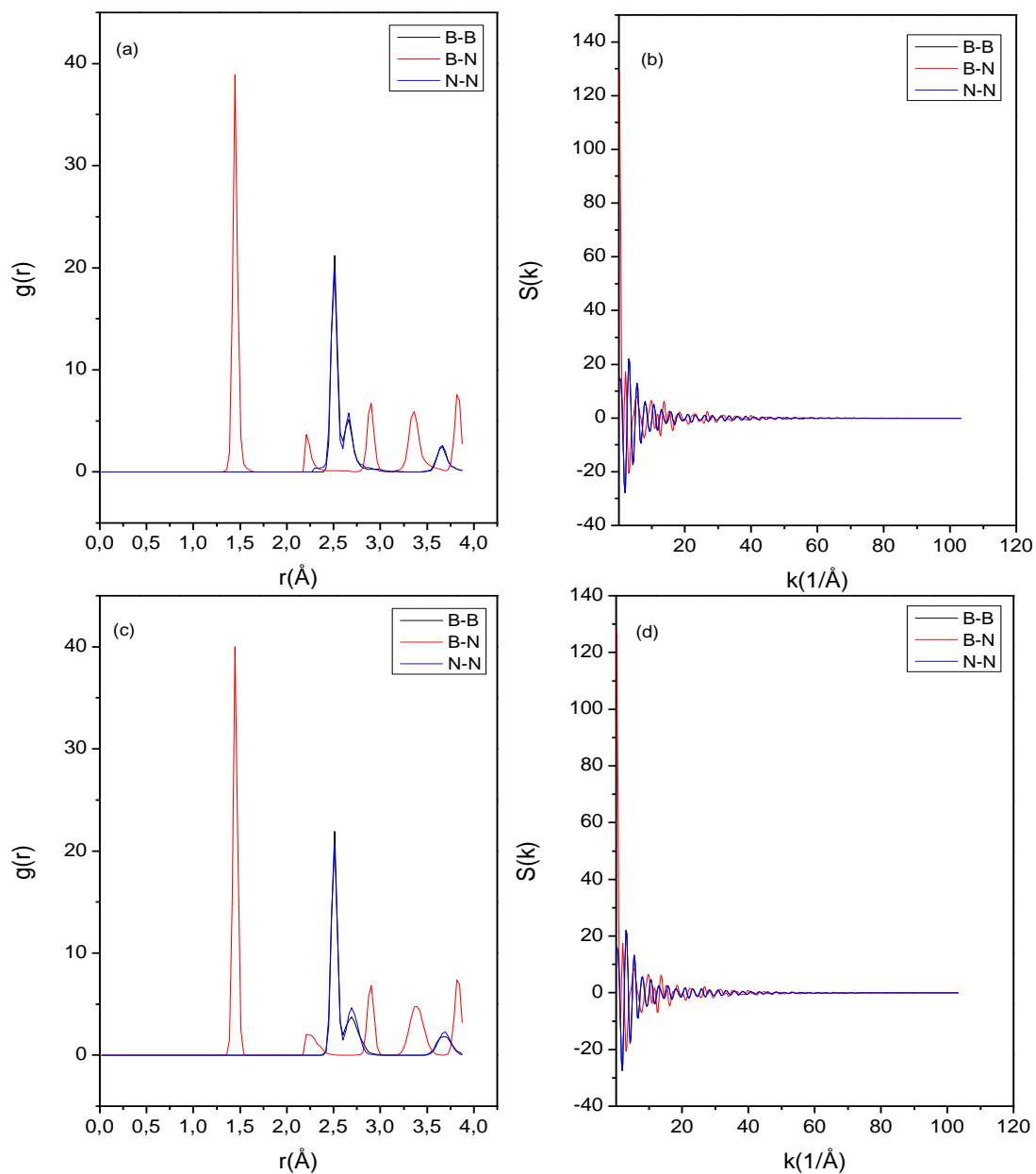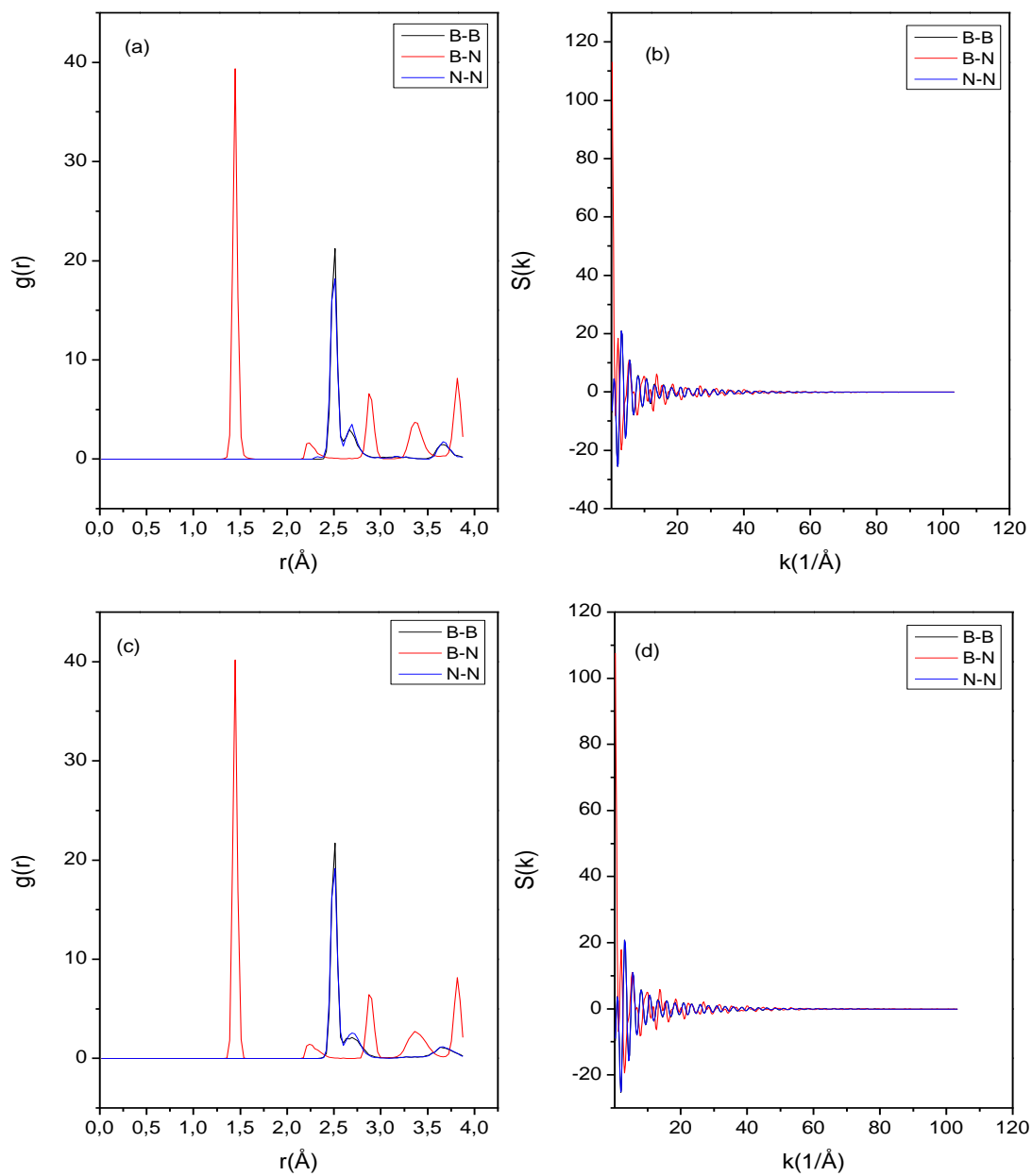
Appendix 1: Graphs
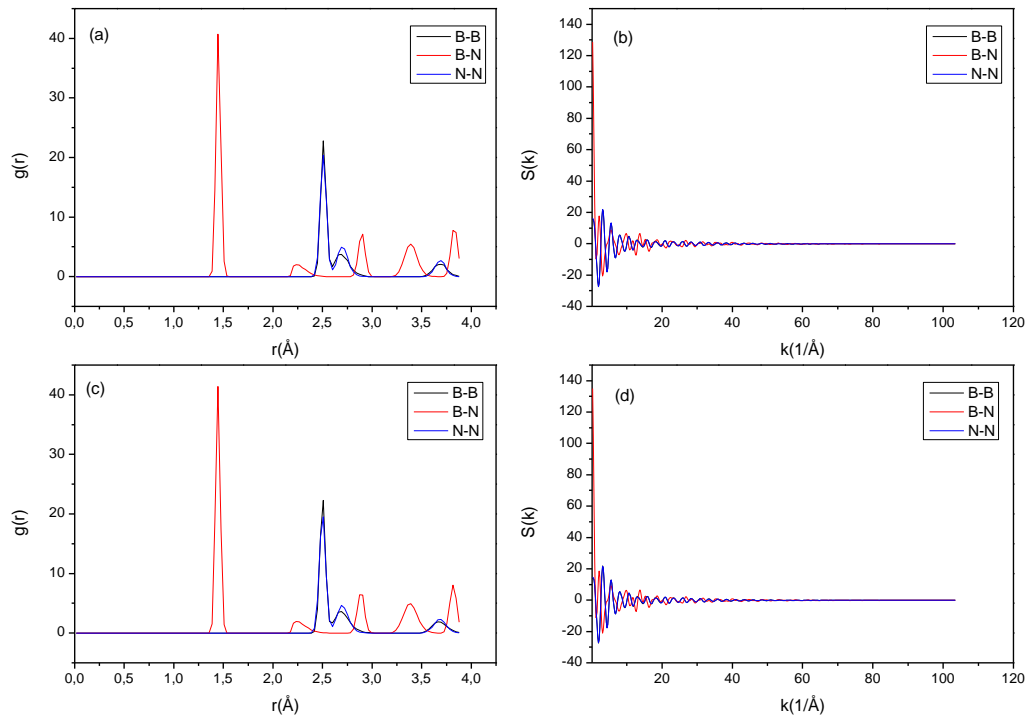
Figure 1- 1: Radial Distribution Functions together with their corresponding structure factors for (a) and (b) h-BNNSs324 supercell and (c) and (d) h-BNNSs576 supercells.
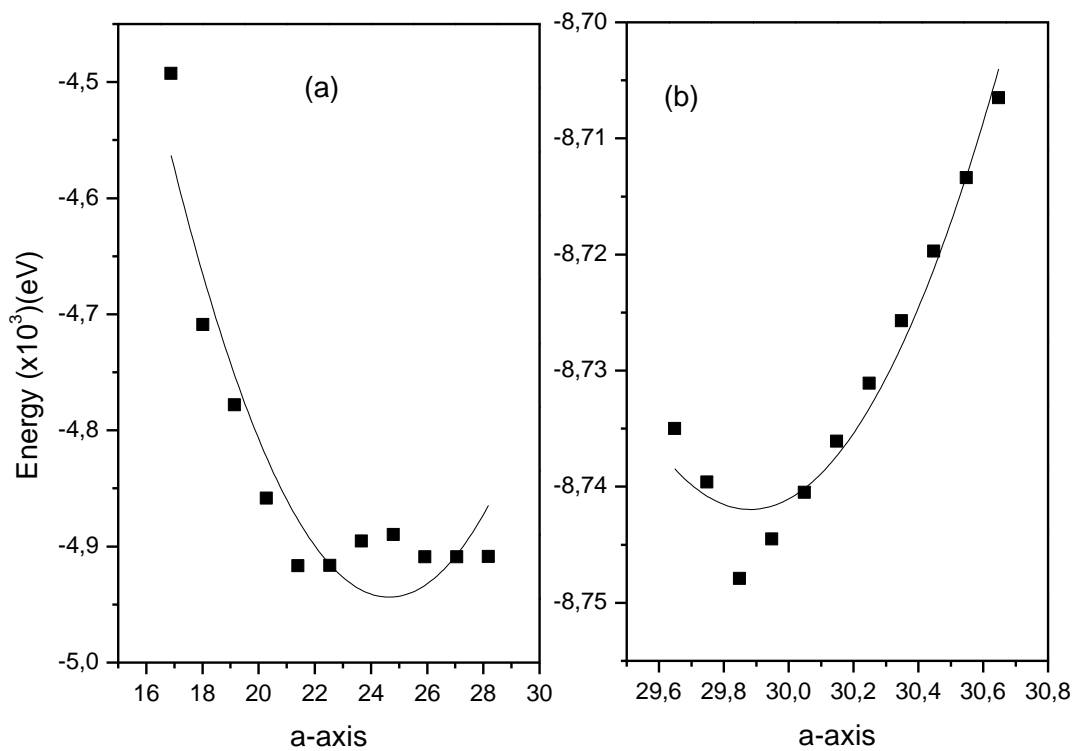
Figure 1- 2: Graphs of Energy vs a-axis of (a) h-BNNSs324 and (b) h-BNNSs576 supercells.
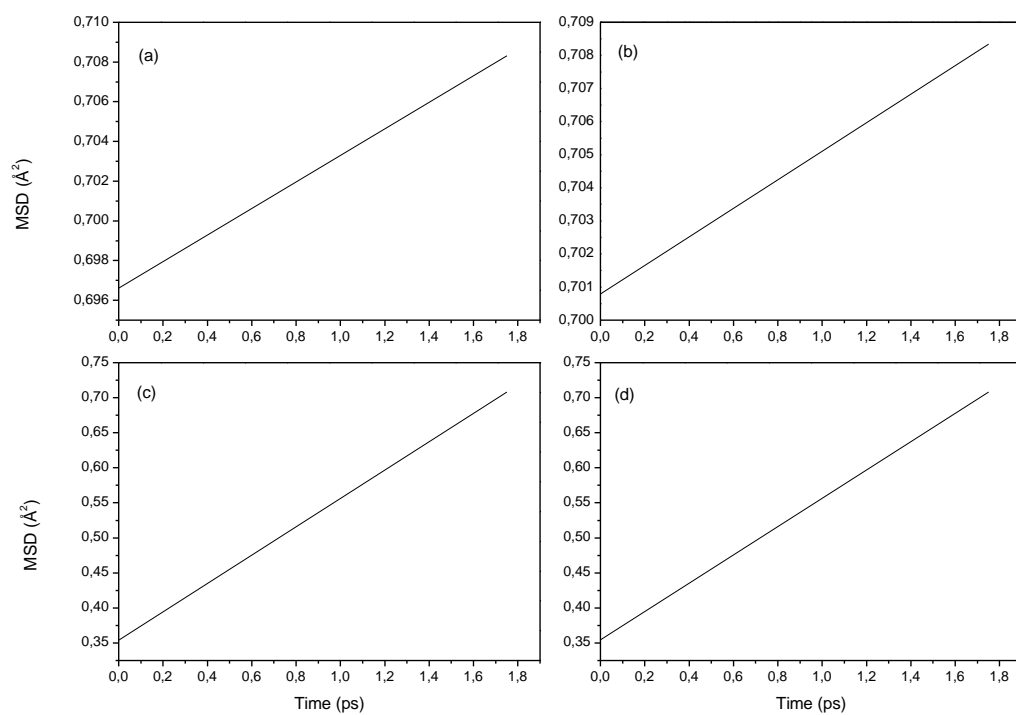
Figure 1- 3: Mean Square Displacement graphs of (a) B for h-BNNSs324, (b) N for h-BNNSs324, (c) B for h-BNNSs576 and (d) N for h-BNNSs576 supercells.
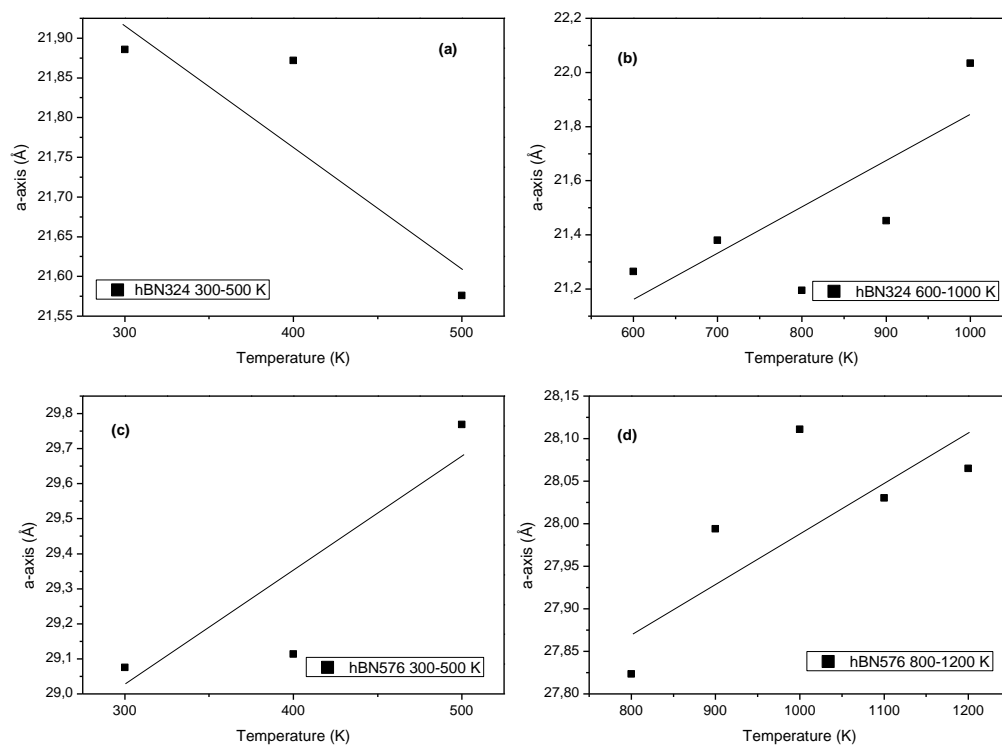
Figure 1- 4: Graphs of a-axis vs temperature for hBN324 (a) 300 –500 K, (b) 600 –
1000 K and hBN576 (c) 300 – 500 K, (d) 800 – 1200 K for determining the coefficient
of thermal expansion under NPT hoover ensemble.

Figure 1- 5: Radial Distribution Functions together with their corresponding structure factors of (a) and (b) V_B for h-BNNSs323 supercell and (c) and (d) V_N for h-BNNSs323 supercell.

Figure 1- 6: Radial Distribution Functions together with their corresponding structure factors of (a) and (b) V_B or h-BNNSs575 supercell and (c) and (d) V_N for h-BNNSs575 supercell.

Appendix 2: Tables

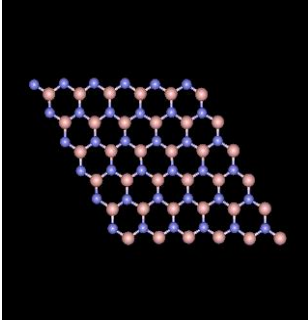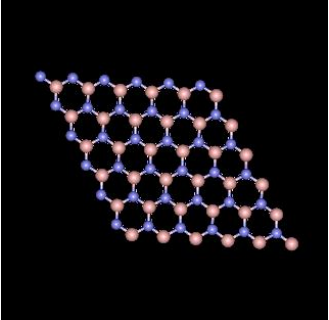Table 2- 1: First and second nearest neighbouring distances (r_1 and r_2) and number of atoms (n_1 and n_2) for h-BNNSs324 and h-BNNSs576 supercells at 300 K.

Supercells	Atomic bonds	r_1(Å)	n_1	r_2(Å)	n_2
h-BNNSs324	B-B	2.51	1.73	2.69	0.34
	B-N	1.44	1.86	2.90	0.43
	N-N	2.51	1.55	2.69	0.45
h-BNNSs576	B-B	2.51	2.45	2.66	0.64
	B-N	1.44	1.86	2.90	0.76
	N-N	2.51	2.15	2.72	0.50

Table 2- 2: Shows the total energy of a defected BN system, vacancy energy for the formation of a vacancy, volume and entropy of a system of V_B and V_N for h-BNNSs323 and h-BNNSs575 supercells.

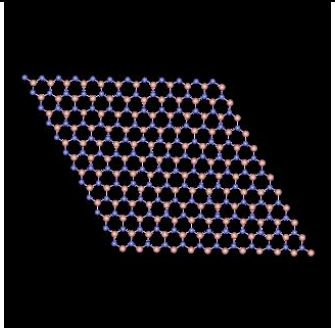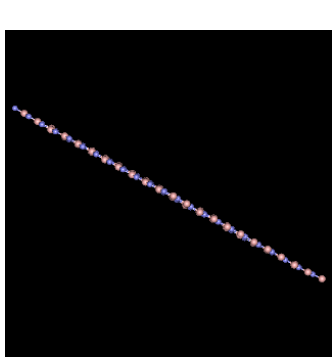| Supercells		B-vacancy	N-vacancy	Defect free
h-BNNSs323	Total energy (eV)	-4.9013×10^3	-4.8875×10^3	-4.9155×10^3
	Vacancy energy (eV)	-14.2	-28	$-$
	Volume (Å^3)	3.4796×10^3	3.4796×10^3	3.4796×10^3
	Entropy (eV. K^{-1})	1.43×10^{-2}	1.43×10^{-2}	8.6×10^{-2}
h-BNNSs575	Total energy (eV)	-8.7249×10^3	-8.7124×10^3	-8.7414×10^3
	Vacancy energy (eV)	-16.5	-29.0	$-$
	Volume (Å^3)	6.1461×10^3	6.1461×10^3	6.1461×10^3
	Entropy (eV. K^{-1})	1.55×10^{-1}	1.53×10^{-1}	1.56×10^{-1}

Table 2- 3: First and second nearest neighbouring distances (r_1 and r_2) and number of atoms (n_1 and n_2) of V_B and V_N in h-BNNSs323 supercell.
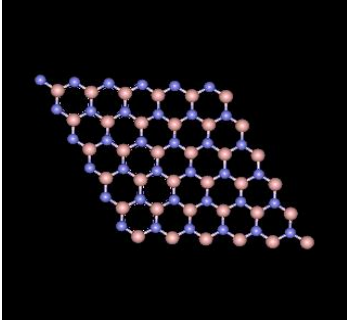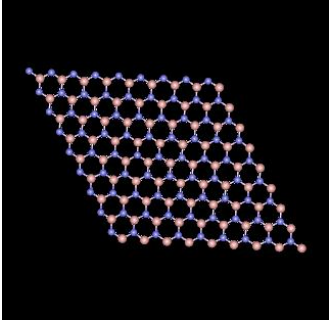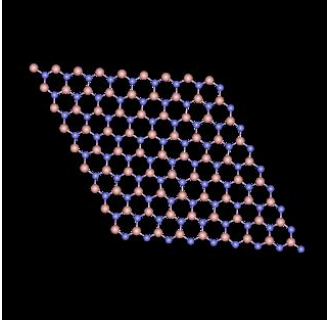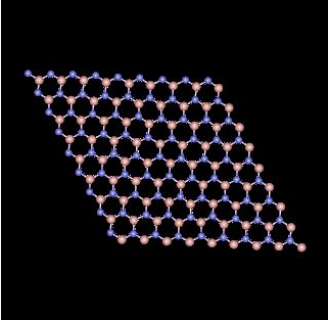
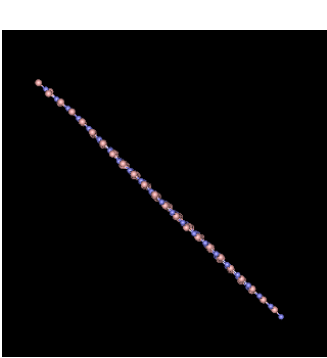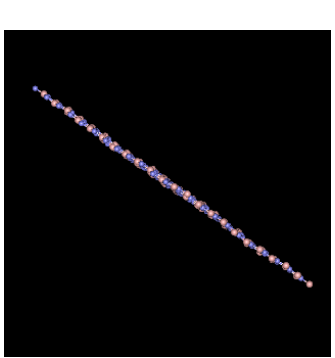| Defect description	Atomic bonds	$r_1(\text{Å})$	n_1	$r_2(\text{Å})$	n_2
V_B	B-B	2.52	1.59	2.3	0.28
	B-N	1.44	2.33	2.90	0.51
	N-N	2.51	1.48	2.66	0.35
V_N	B-B	2.51	1.64	2.66	0.36
	B-N	1.44	2.40	2.90	0.51
	N-N	2.51	1.55	2.69	0.42
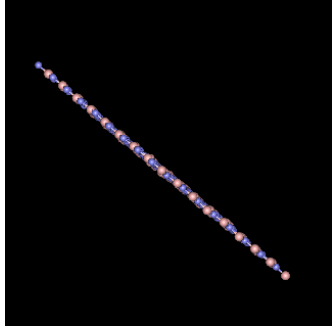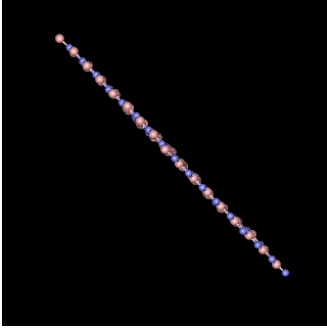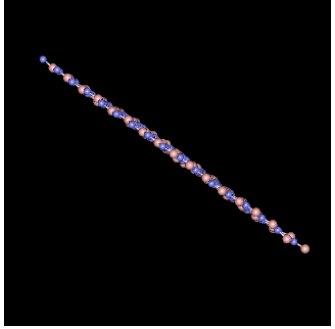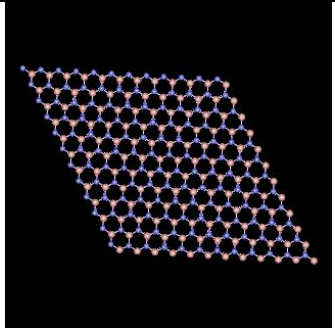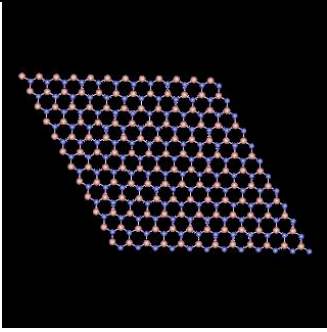
Table 2- 4: First and second nearest neighbouring distances (r_1 and r_2) and number of atoms (n_1 and n_2) of V_B and V_N in h-BNNSs575 supercell.

Defect description	Atomic bonds	r_1(Å)	n_1	r_2(Å)	n_2
V_B	B-B	2.51	2.24	2.66	0.32
	B-N	1.44	2.96	2.90	0.54
	N-N	2.51	1.92	2.69	0.37
V_N	B-B	2.51	1.95	2.75	0.28
	B-N	1.44	3.02	2.90	0.55
	N-N	2.51	1.75	2.75	0.34

Appendix 3: Visualisations

Table 3- 1: The visualisation of the structural alignments represented by alternating B (brown balls) and N (blue balls) atoms for defect free nanosheets for all the supercells at three different temperatures of 300, 500 and 1000 K.

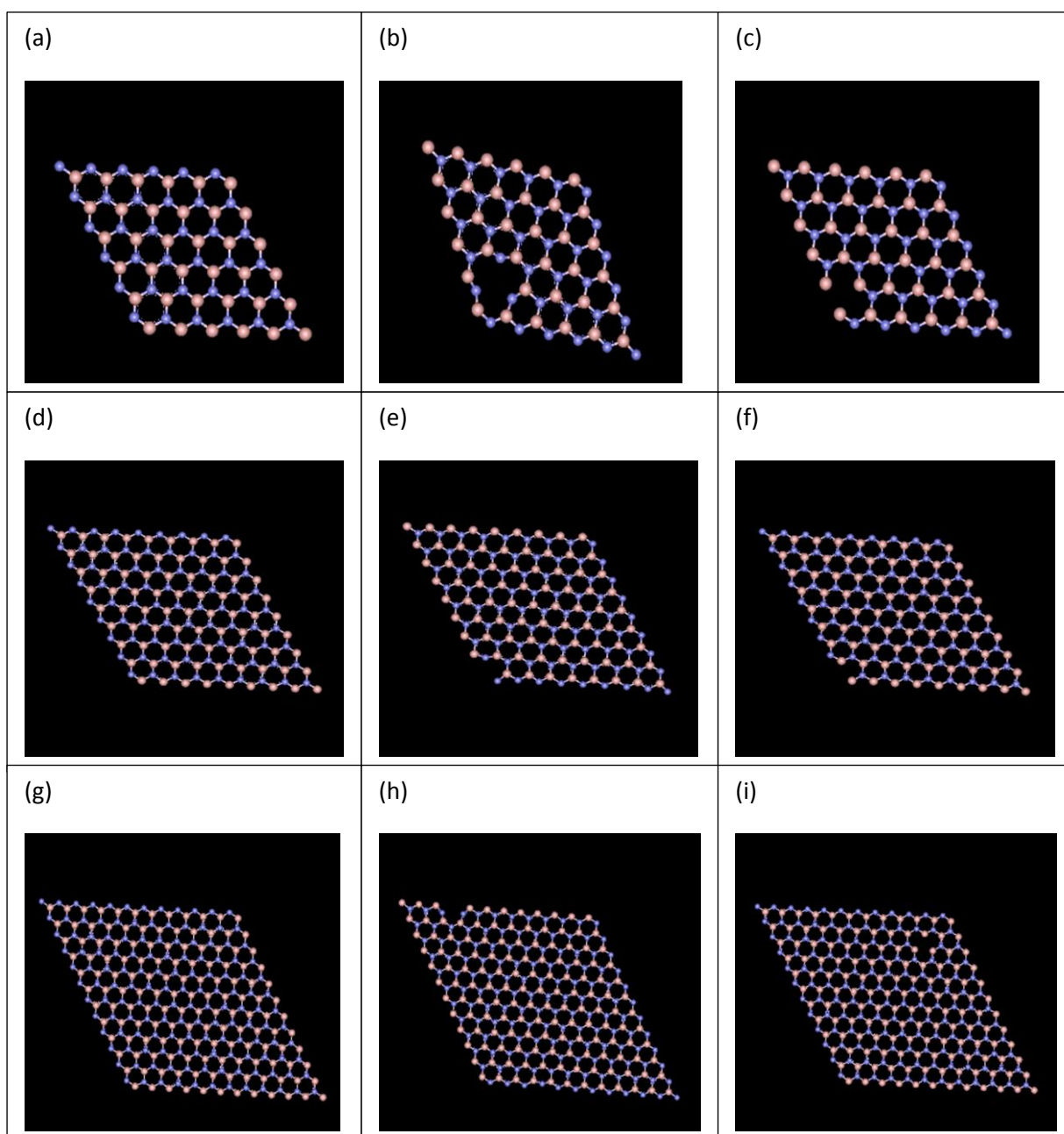| • B • N	300 K	500 K	1000 K
h-BNNSs144			
h-BNNSs324			

h-BNNSs576			

173

Figure 3- 1: The visualisation of V_B and V_N where brown and blue balls represent B and N atoms respectively. (a) defect free for 144 atoms, (b) V_B for 143 atoms, (c) V_N for 143 atoms, (d) defect free for 324 atoms, (e) V_B for 323 atoms, (f) V_N for 323 atoms, (g) defect free for 576 atoms, (h) V_B for 575 atoms and (i) V_N for 575 atoms supercells.